

**Calibration of the Polarization of a
Frozen Spin Type Polarized Proton Target**

by

Konstantinos Chantziantoniou

A thesis
submitted to the Faculty of Graduate
Studies in partial fulfillment of the
requirements for the degree
of
Master of Science

Department of Physics

Winnipeg, Manitoba

©K. Chantziantoniou, 1989



National Library
of Canada

Bibliothèque nationale
du Canada

Canadian Theses Service Service des thèses canadiennes

Ottawa, Canada
K1A 0N4

The author has granted an irrevocable non-exclusive licence allowing the National Library of Canada to reproduce, loan, distribute or sell copies of his/her thesis by any means and in any form or format, making this thesis available to interested persons.

The author retains ownership of the copyright in his/her thesis. Neither the thesis nor substantial extracts from it may be printed or otherwise reproduced without his/her permission.

L'auteur a accordé une licence irrévocable et non exclusive permettant à la Bibliothèque nationale du Canada de reproduire, prêter, distribuer ou vendre des copies de sa thèse de quelque manière et sous quelque forme que ce soit pour mettre des exemplaires de cette thèse à la disposition des personnes intéressées.

L'auteur conserve la propriété du droit d'auteur qui protège sa thèse. Ni la thèse ni des extraits substantiels de celle-ci ne doivent être imprimés ou autrement reproduits sans son autorisation.

ISBN 0-315-63313-1

Canada

CALIBRATION OF THE POLARIZATION OF A
FROZEN SPIN TYPE POLARIZED PROTON TARGET

BY

KONSTANTINOS CHANTZIANTONIOU

A thesis submitted to the Faculty of Graduate Studies of
the University of Manitoba in partial fulfillment of the requirements
of the degree of

MASTER OF SCIENCE

© 1989

Permission has been granted to the LIBRARY OF THE UNIVER-
SITY OF MANITOBA to lend or sell copies of this thesis. to
the NATIONAL LIBRARY OF CANADA to microfilm this
thesis and to lend or sell copies of the film, and UNIVERSITY
MICROFILMS to publish an abstract of this thesis.

The author reserves other publication rights, and neither the
thesis nor extensive extracts from it may be printed or other-
wise reproduced without the author's written permission.

DEDICATION

I dedicate this work to my parents for the sacrifices they have made to give their beloved children a better life and education.

ABSTRACT

Polarized proton targets of the frozen spin type (FST) rely on nuclear magnetic resonance (NMR) systems to measure the proton polarization. Difficulties arise when the polarization must be known to an absolute accuracy that is greater than that achievable by the currently used NMR systems, which are typically in the order of $\pm 4\%$. An independent absolute measurement of the FST proton polarization was achieved at TRIUMF by performing a p-p elastic scattering experiment at an energy and angle where the p-p analyzing power is accurately known. A beam of unpolarized protons was scattered from the FST, and the scattered and recoil protons were detected in two symmetrically placed detector systems. The measurement of the FST proton polarization distribution allowed the calibration of the NMR system to be made to an absolute accuracy of $\pm 2.6\%$. The average NMR calibration constant, deduced from its distribution over three equally segmented horizontal bins (top, middle and bottom), was 0.953 ± 0.025 (absolute).

ACKNOWLEDGEMENTS

I would like to thank Professor W.T.H. van Oers for his guidance, support and patience which not only stimulated my interest in this work but also gave me the opportunity to be involved in an experiment performed at the TRIUMF cyclotron laboratory.

I would also like to express my deepest gratitude to Dr. S.A. Page for her undivided attention and patience in those long and frequent discussions concerning the experimental techniques and data analysis. I am indebted to her for the knowledge and experience that I have gained. I wish to express thanks to Dr. J. Birchall for his guidance and valuable suggestions relating to the data analysis. Particular thanks are due to Dr. D.C. Healey and Dr. P.P.J. Delheij for their discussions concerning the theory and experimental operation of the polarized proton target. It is great pleasure to thank Dr. D. Bandyopadhyay for his data analysis assistance and for making my stays at TRIUMF most pleasurable.

Special thanks are reserved for my wife, Connie Rose, who has given me continuing encouragement, understanding and for enduring so patiently the division of my attention during the preparation of this work, and without whom it would not have been completed. I also would like to thank my son, Dimitrios John, for taking my mind away from the field of physics during periods where mental rest was most appropriate. Last but not least, thanks go to my brother, Nick, for helping me architect and draw the various figures in this work.

TABLE OF CONTENTS

	Page
Title page	i
Thesis examination committee approval	ii
Dedication	iii
Abstract	iv
Acknowledgements	v
List of Figures	x
List of Tables	xiii
List of Constants	xv
I. Introduction	1
II. The Frozen Spin Target	4
II.1 Introduction	4
II.2 The Dynamic Nuclear Polarization Method	5
II.3 The He-3/He-4 Dilution Refrigerator	12
II.3.a Liquid mixture of He-3 and He-4	12
II.3.b The Principle of Dilution	14
II.3.c Theory of Operation of a Dilution Refrigerator	14
II.3.d Dilution Refrigerator External Heat Load Limitation	21
II.4 The Frozen Spin Target Apparatus	23
II.4.a Procedure Used to Cool the Frozen Spin Target Sample	24
II.4.b Procedure Used to Attain and Maintain the Frozen Spin Target Sample Polarization	28
II.5 Nuclear Magnetic Resonance	32
II.5.a Theoretical Consideration of the NMR Polarization Measurement	35
II.5.b Difficulties in Using the NMR System to Determine the FST Polarization	37

IV.2.b Scattered and Recoil Proton Analysis	121
IV.2.b.1 Track Reconstruction	121
IV.2.b.2 Time of Flight	125
IV.2.b.3 Proton Energies and Momenta	132
IV.2.b.4 Scattered and Azimuthal Angles	135
IV.2.b.5 FST Image Reconstruction	140
IV.3 Data Rejection	140
IV.4 Constraints used to Identify Elastic Scattering Events	142
IV.4.a Energy Sum	145
IV.4.b Opening Angle	145
IV.4.c Coplanarity Angle	148
IV.4.d Transverse Momentum Sum	148
IV.5 Data Representation	150
IV.5.a Detector Counts	151
IV.5.a.1 Background Corrections	154
IV.5.a.2 Total Detector Efficiency Corrections	155
IV.5.b Effective Runs	155
IV.6 FST Polarization Measurement	155
IV.6.a Using p-p Elastic Scattering Experiment	155
IV.6.a.1 Scattering Asymmetry	155
IV.6.a.2 p-p Analyzing Power	159
IV.6.a.3 FST Polarization	162
IV.6.b Using the NMR System	163
IV.7 FST Polarization Distribution	164
IV.8 Average FST Polarization	168
IV.9 NMR Polarization Calibration	168
V. Results and Discussion	170
V.1 Conclusion	184
References	185
Appendix A	
Frozen Spin Target Polarization Uncertainty Requirement	187
Appendix B	
Proton Ensemble Polarization at Thermal Equilibrium	189

Appendix C

Systematic Error Calculations	192
C.1 Incident Proton Beam Energy	193
C.2 Scattered Proton Detector Positioning	194
C.3 Holding Field Deflection Angles	194
C.4 p-p Analyzing Power	196
C.5 Different FST Polarization	197
C.6 Background Fraction Estimation	198
C.7 Superconducting Solenoid Spin Precession	199
C.7.a Incorrect Solenoid Current Setting	200
C.7.b Solenoid Misalignment	201
C.8 Extraneous Beam and FST Polarization Components	202

Appendix D

Experimental Data	204
-------------------	-----

LIST OF FIGURES

Figure	Description	Page
1	Proton Polarization at Thermal Equilibrium	6
2	Energy Level Diagram of Electron-Proton System in an External Magnetic Field	9
3	Phase Separation Curve for a Liquid He-3/He-4 Mixture Below 1.5 K	13
4	Schematic of the Dilution Process	15
5	Schematic of Dilution Refrigerator Used in p-p Elastic Scattering Experiment	18
6	Mixing Chamber Power Test	22
7	Schematic of Target Chamber	25
8	Cool Down Curve of Mixing Chamber	29
9	Magnet Arrangement Used in Experiment	30
10	Typical Polarization Curve Obtained by the FST Using the Dynamic Nuclear Polarization Method	31
11	Energy Level Diagram of Polarized Proton States in Static External Magnetic Field	34
12	Experimental Layout Used in the p-p Elastic Scattering Experiment	41
13	Proton Beam Transport System	44
14	Schematic of the BEM-Polarimeter Apparatus	47
15	Electronics Diagram for BEM-Polarimeter System	48
16	Axial Magnetic Field of Superconducting Solenoid	55
17	Schematic Diagram of Electronics for Either Start or Stop Scintillator Signals	62
18	Types of Pulse Discrimination	63

19	The Effect of Input Signals of Differing Amplitudes on the Timing of the Output Pulse From an Integral Discriminator	64
20	CFD Principle of Operation	65
21	The Horizontal Drift Chamber	67
22	Holding Field as a Function of Radial Distance from the FST in the Horizontal Beam Plane	73
23	Experimental Coordinate System Definitions	77
24	Scattered Proton Detector Electronics	82
25	The Delay Line Chamber	84
26	Delay line Chamber Electronics	85
27	Recoil Proton Detector Electronics	93
28	Schematic of p-p Elastic Scattering Experiment's Trigger Logic	96
29	Incident Beam TOF Spectrum	106
30	Primary Proton Beam Energy Deviation as Measured by the BEM System	110
31	Magnetic Field Deflection Angle Geometry for the Incident Beam Protons	115
32	Incident Proton Beam Magnetic Field Deflection Angle Sign Convention	116
33	FST Images Obtained from the Nearest Horizontal Drift Chamber Coordinate Distributions	120
34	Coordinate Resolution Spectra for Left Event DLC 3	123
35	Scattered Proton TOF Stop Scintillator Region Segmentation	127
36	Total Detector Efficiency Variation with Run Number	130
37	Scattered and Recoil Proton TOF Spectra	131

38	Scattered and Recoil Proton Energy Error Spectra	134
39	Scattering and Azimuthal Angle Coordinate Definitions	137
40	FST Holding Field Deflection Angle Illustration	139
41	FST Image Reconstruction Using the Scattered Proton Track Projections	141
42	Energy Sum and Opening Angle Error Plots Used to Identify Elastic Scattering	146
43	Non-coplanarity and Transverse Momentum Sum Plots Used to Identify Elastic Scattering Events	149
44	Opening Angle χ_i^2 Distribution Centroids as a Function of Proton Scattering Angle	152
45	Proton Scattering Angle Distribution Binned to Aid in $\bar{A}_y(\theta)$ Calculation	161
46	FST Sample Segmentation	165
47	Average NMR Calibration Constant Results Using Various Scattering Asymmetry Methods	177
48	Average NMR Calibration Constant Results When Using Various Count Rate Corrections	178

LIST OF TABLES

Table	Description	Page
1	Operating Parameters of Frozen Spin Target	39
2	Operating Parameters of Polarimeter-Beam Energy Monitor Assembly	50
3	Superconducting Solenoid Specification	54
4	DAC Settings of "Clyde" and Corresponding Total Deflection Angles	59
5	DAC Settings of "Bonnie" and Corresponding Total Deflection Angles	59
6	Secondary Proton Beam TOF System Specification	60
7	Horizontal Drift Chamber Material in the Secondary Proton Beam Path	70
8	Frozen Spin Target Holding Field Deflection Angles	72
9	Frozen Spin Target Material in the Secondary Proton Beam Path	74
10	X-ray Radiograph Results of Frozen Spin Target	75
11	Positions of Scattered Proton Detection Apparatus Along Beam	79
12	Scattered Proton Detection System TOF Start Scintillator Dimensions	80
13	DLC Cathode Strip Geometry With Respect to Anode Wire Direction	88
14	Delay Line Chamber Material in the Scattered Proton Path	90
15	Positions of Recoil Proton Detection Apparatus	92
16	Recoil Proton Veto Scintillator Dimensions	95
17	Event Type Summary	98
18	DCR Bit Map Summary	99

19	Tape Summary of LH2 p-p Elastic Scattering Experiment	101
20	Tape Summary of C p-p Elastic Scattering Experiment	102
21	Primary Proton Beam Energy Breakdown	108
22	FST Holding Field Deflection Coefficient	113
23	FST y-coordinate Image Centroid	118
24	Average DLC Coordinate Efficiencies	124
25	Software Cut Rejection of Data	143
26	Badword Bit Map Summary	144
27	Effective Runs Used in LH2 Calibration Experiment	156
28	Effective Runs Used in C Calibration Experiment	156
29	FST Polarization Distribution Using Three and Six Bin Arrangements	167
30	FST Polarization Distribution	171
31	NMR Polarization Distribution	172
32	FST Experimental Parameters	174
33	Systematic Error Considerations	180
34	Average NMR Calibration Constant Results	181
35	LH2 Run Primary Proton Beam Energy Losses	182

LIST OF CONSTANTS

Constant	Symbol	Value
Proton Gyromagnetic Ratio	γ_p	$2.67519 \times 10^8 \text{ rad} \cdot \text{m}^2 \cdot \text{s}^{-1} \cdot \text{Wb}^{-1}$
Planck Constant Divided by 2π	\hbar	$1.05450 \times 10^{-34} \text{ J} \cdot \text{s}$
Boltzmann Constant	k	$1.3806 \times 10^{-23} \text{ J} \cdot \text{K}^{-1}$
Gas Constant	R	$8.3143 \times 10^3 \text{ J} \cdot \text{mol}^{-1} \cdot \text{K}^{-1}$
Velocity of Light	c	$2.9979 \times 10^8 \text{ m} \cdot \text{s}^{-1}$
	$\hbar c$	$1.9733 \times 10^{-13} \text{ MeV} \cdot \text{m}$
Proton Rest Mass	$m_p c^2$	938.28 MeV
Proton Magnetic Moment	μ_p	$8.8 \times 10^{-14} \text{ MeV} \cdot \text{T}^{-1}$
Proton Resonance Frequency	ν_p	$42.5759 \text{ MHz} \cdot \text{T}^{-1}$

CHAPTER I

INTRODUCTION

Polarized proton targets of the frozen spin type, otherwise known as frozen spin targets (FST), have been used in nuclear and high energy physics experiments for over two decades. Great emphasis has been placed on their development, largely because of their ability to achieve and maintain high proton polarizations as is required for the measurements of many spin-dependent observables.

Frozen spin targets currently in use utilize "dynamic" methods, that is microwave "pumping", to achieve polarization. Nuclear magnetic resonance (NMR) methods are then used to ascertain the degree of proton polarization in the target. For the FST developed at the TRIUMF cyclotron facility, the absolute accuracy in the NMR polarization measurements was typically about $\pm 4\%$ [Ref. 1].

Using NMR techniques to measure the FST polarizations have a two fold disadvantage:

- (a) achieving an absolute accuracy of $\pm 4\%$ may be sufficient for most nuclear scattering experiments, but for cases in which the target polarization must be known to higher accuracy, the current NMR techniques are clearly inadequate; and
- (b) because of the NMR coil physical geometry within the target sample, the NMR system samples different parts of the target volume with unequal weight, indicating a target polarization that may be different from what is seen by the beam in the actual experiment.

Therefore, what is needed is an independent absolute measurement of the FST polarization, which can be achieved by a proton-proton (p-p) elastic

scattering experiment. The accuracy in the FST polarization measurements in such experiments is then limited by the known accuracy of the p-p analyzing powers, which act as systematic errors (scale factors). A second advantage in using p-p scattering events originating throughout the entire target volume to measure the target polarization is that not only does it give a good representation of the true average polarization, but it also provides the means to determine the target polarization distribution, thus enabling finite target size effects to be accounted for.

An experiment was performed at the TRIUMF cyclotron laboratory to measure the neutron-proton (n-p) spin correlation parameter $A_{yy}(\theta)$ and analyzing power $A_y(\theta)$ to an absolute accuracy of ± 0.03 , for the angular range of 40° to 150° (center of mass) at incident neutron energies of 220, 325 and 425 MeV [Ref. 2]. Attainment of the ± 0.03 absolute accuracy depended on the criterion that the FST proton polarization be known to an absolute accuracy of $\pm 2\%$ [see Appendix A].

The objective of this work is to determine the average NMR calibration constant from the FST proton polarization distribution to an absolute accuracy of $\pm 2\%$ by performing a p-p elastic scattering experiment at an energy and angle where the p-p analyzing power is known to $\pm 1.5\%$ [Ref. 3]. The proton polarization was determined from a measurement of the left-right scattering asymmetry.

The main concern of this thesis is the direct measurement of the target polarization distribution (and hence the NMR calibration constant distribution) using p-p elastic scattering. Chapter II will describe the FST polarizing mechanism, how the polarization was maintained, how

the NMR system measured the target polarization, and the difficulty that arose when using the NMR system. Chapter III is concerned with the experimental apparatus for the p-p elastic scattering experiment, and Chapter IV presents the analysis involved in the determination of the average NMR calibration constant from the FST polarization distribution. Finally, Chapter V summarizes the results, and draws conclusions about the target polarization and NMR calibration constant distributions.

CHAPTER II

THE FROZEN SPIN TARGET

II.1 Introduction

The traditional polarized targets used in particle scattering experiments were mainly of the continuously polarizing type, in which irradiation of the target nuclei with microwaves was required to obtain and maintain the target polarization. This required that the target be held continuously in a strong magnetic field which was uniform over the target volume.

In 1965, Schmutge and Jeffries [Ref. 4] suggested that target polarizations could be maintained without an external microwave source in a less homogeneous and perhaps less strong field. Their prediction was based upon the observation that the nuclear spin-lattice relaxation time of the protons in Lanthanum Magnesium Nitrate [$\text{La}_2\text{Mg}_3(\text{NO}_2)_{12} \cdot 24\text{H}_2\text{O}$] extrapolated to very large values at temperatures below 1 K. Using this material would free the experiment from the constraint of having the target in a region of high uniform magnetic field, allowing a large solid angle of access for observing the scattered particles and minimal perturbation of the particle trajectories. The advent of highly polarizable organic materials [Ref. 5, 6] having long relaxation times at low temperatures, and the incorporation of the dilution refrigerator in the polarized proton target, as suggested by London, Clarke and Mendoza [Ref. 7] led to the development of the FST. The large angle of acceptance around the FST, the orientability of the target polarization, and the use of a low holding field have made the use of the FST in present day nuclear scattering or reaction experiments most desirable.

II.2 The Dynamic Nuclear Polarization Method

Consider an ensemble of protons in a static external magnetic field, \vec{B} . The proton polarization at thermal equilibrium (TE) can be shown [see Appendix B] to be of the form:

$$P_{TE} = \tanh\left(\frac{\gamma B \hbar}{2kT}\right) \quad (1a)$$

$$= \frac{n(m = 1/2) - n(m = -1/2)}{n(m = 1/2) + n(m = -1/2)} \quad (1b)$$

with

$$n(m) = e^{-\frac{m\gamma B \hbar}{kT}} \quad (1c)$$

where γ is the gyromagnetic ratio of the proton (in $\text{rad}\cdot\text{m}^2\cdot\text{s}^{-1}\cdot\text{Wb}^{-1}$), B is the magnitude of the magnetic field (in T), \hbar is Planck's constant divided by 2π (in J·s), k is the Boltzmann constant (in $\text{J}\cdot\text{K}^{-1}$) and T is the absolute temperature (in K). The occupation number $n(m)$ of the magnetic substate, m , after the Zeeman splitting of the proton energy levels is given by the Boltzmann distribution [Eq. 1c].

It is seen from [Eq. 1a] that significant proton polarizations can in principle be achieved by reducing the temperature and/or increasing the magnetic field so that the thermal energy kT becomes much smaller than the magnetic energy $\frac{\gamma B \hbar}{2}$. This is illustrated in [Fig. 1].

However, the construction difficulties in refrigerators operating at very low temperatures (< 10 mK) and the requirement in nuclear scattering or reaction experiments to have the least possible interference by target, cryostat and magnet with the incoming and/or scattered charged particles, has made this "brute force" method of polarizing protons inadequate. The requirement for a strong magnetic

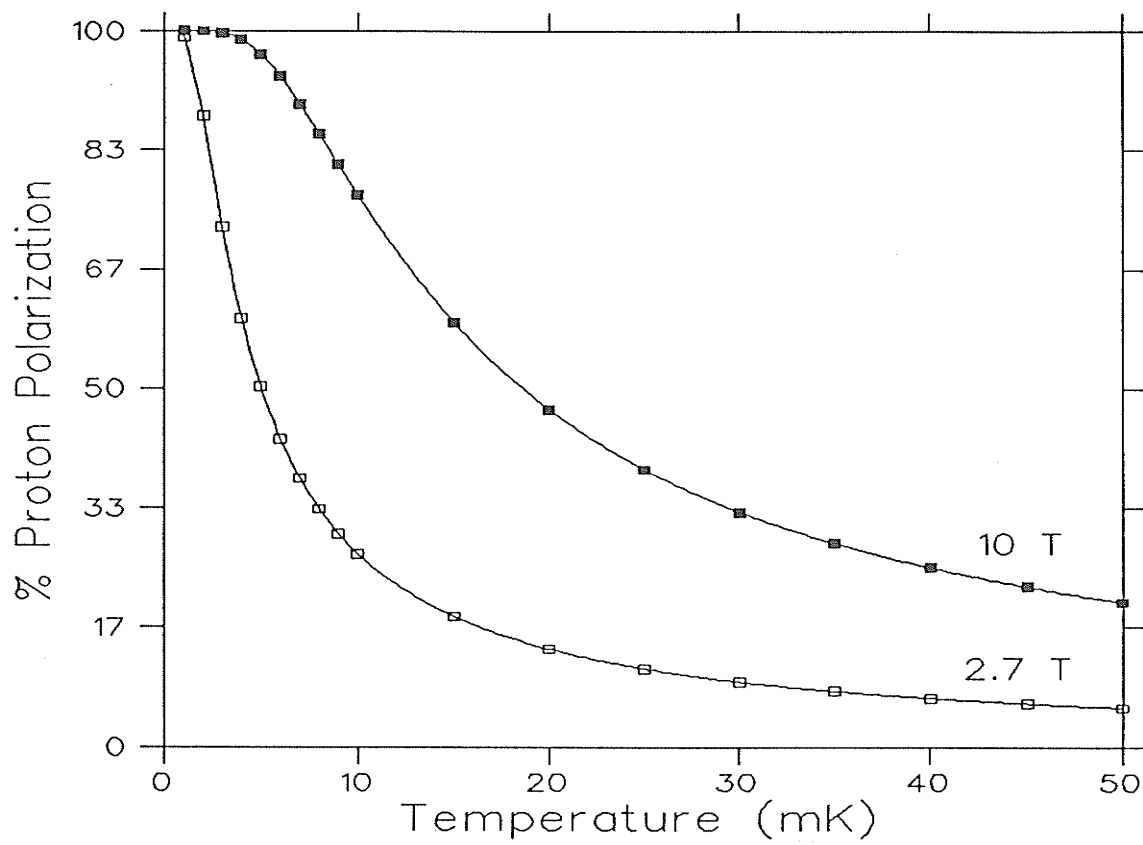


[Fig. 1]

Proton polarization at thermal equilibrium calculated for magnetic fields of 2.7 and 10 T, using [Eq. 1a].

field is particularly restrictive for lower energy (less than 100 MeV) charged particles.

An alternate scheme was then developed which allowed achievement of proton polarizations as high as 0.97 [Ref. 8], using magnetic fields of 2.5 T and operating temperatures of ~ 0.5 K. Under these conditions the brute force method would have obtained a proton polarization of only 0.005. The new method has come to be known as the dynamic nuclear polarization method or the "solid effect".

The samples that are commonly used as target material for the dynamic method of proton polarization are organic substances [Ref. 5, 6] that have been doped with an electron donor material, usually a complex molecule containing the chromium atom. This is done because the efficiency of the polarization process depends on the density of free electrons in the target sample, as will be explained below. In this method the electrons in question are the unpaired electrons of the chromium atoms, whereas the protons to be polarized are the nuclei of hydrogen atoms in the organic substance.

The mechanism of target (proton) polarization is indirect: first the spins of the electrons are polarized, and then the polarization is transferred to the protons. This is made possible by the fact that the electron has a magnetic moment some 660 times larger than that of the proton and so under conditions of 2.5 T and 0.5 K has a polarization in excess of 0.99.

In the presence of an external magnetic field that permeates the target sample, the electrons and protons form temporary pairs, whose energy levels undergo Zeeman splitting into four distinct magnetic

substates $|m_e m_p\rangle$ depending on the electron (m_e) and proton (m_p) spin orientation [Fig. 2]. In this discussion a spin up (down) orientation with respect to the external magnetic field \vec{B} , is denoted as '+' (-). The occupation numbers of the magnetic substates at thermal equilibrium are given by the Boltzmann factor. Under conditions of 2.5 T and 0.5 K, the states $|+-\rangle$ and $|++\rangle$ are almost unpopulated and the states $|--\rangle$ and $| -+\rangle$ are approximately equally populated.

By irradiating the target sample with microwave photons of energy $h(\nu_e + \nu_p)$ the transition N becomes saturated, equalizing the populations of the states $|--\rangle$ and $|+-\rangle$. The electrons are strongly coupled to the lattice and so the state $|+-\rangle$ quickly relaxes (relaxation time ~ 1 ms [Ref. 9]) to the state $|--\rangle$ by electron spin flip. After a certain time the state $|--\rangle$ breaks up into an electron and proton, leaving the proton in a spin state reversed from that in which it started. The electrons are free to form spin coupled states with other protons, some of which are in the $|+\rangle$ state and so can be flipped to a $|-\rangle$ state. Since the protons are only weakly coupled to the lattice, they relax to their equilibrium state relatively slowly; by this process of microwave pumping, the proton $|-\rangle$ state is populated at the expense of the $|+\rangle$ state and the magnitude of the proton polarization approaches that of the electron polarization. Thus, the proton polarization can be given as:

$$P = -\tanh\left(\frac{h\nu_e}{2kT}\right) \quad (3)$$

which is enhanced by the magnetic moment (μ) factor $\mu_e/\mu_p \approx 660$ over the thermal equilibrium polarization given by:

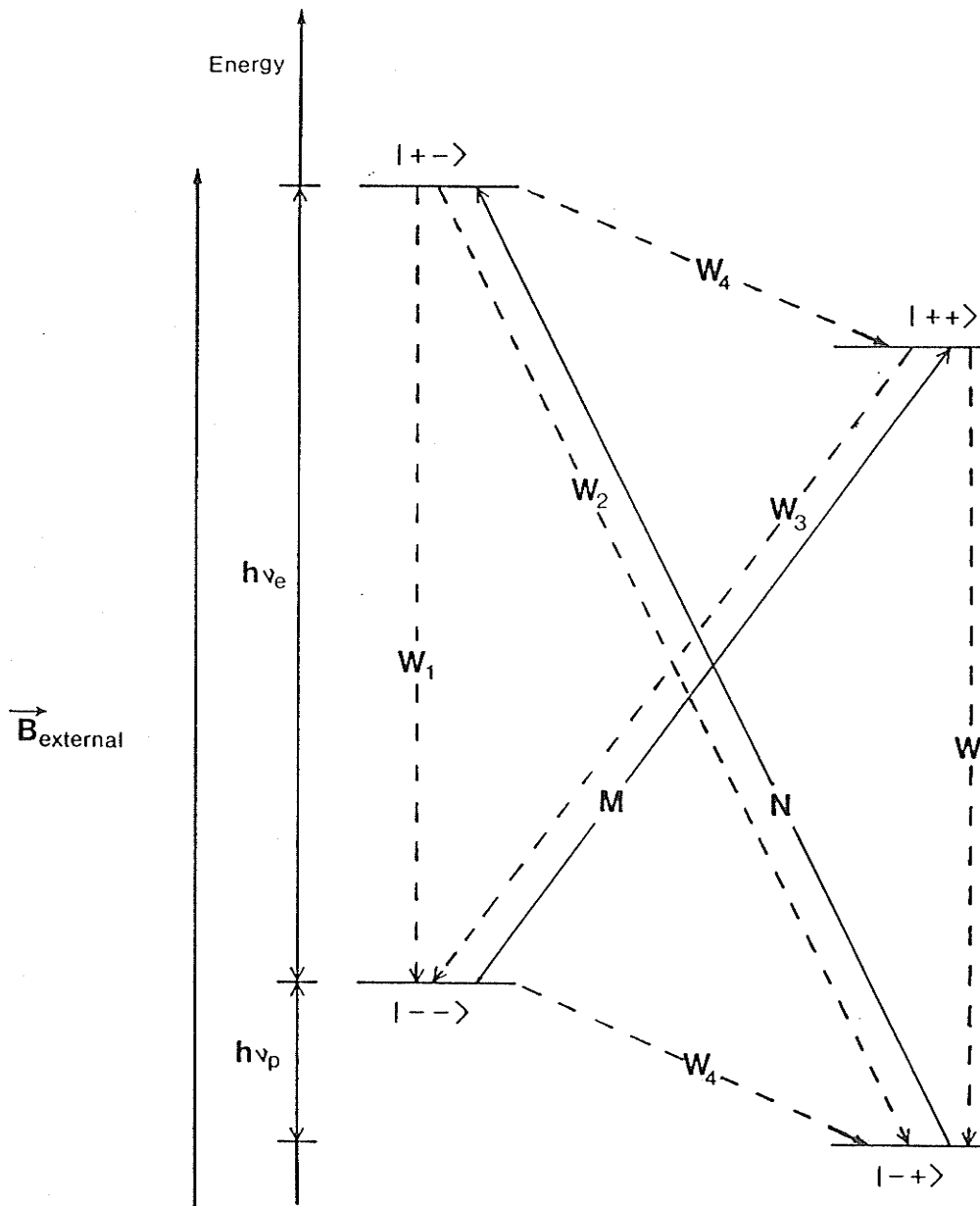


[Fig. 2]

Energy level diagram of electron-proton system in an external magnetic field \vec{B} . The state $|m_e m_p\rangle$ for electron and proton spin up (+) orientation is labelled as $|++\rangle$. The solid lines represent microwave pumped transitions whereas the dashed lines represent the decay of excited states (relaxation transitions).

$$P_{TE} = -\tanh\left(\frac{h\nu_p}{2kT}\right) \quad (4)$$

where h is Planck's constant (in J·s) and ν being the transition frequency (in Hz). [Eq. 4] can be related to [Eq. 1a] by performing the following substitution:

$$\nu_p = \frac{\omega_p}{2\pi} \quad (5a)$$

$$= \frac{\gamma B}{2\pi} \quad (5b)$$

where ω_p is the proton angular frequency in the magnetic field \vec{B} .

In the above example, microwave photon energy of $h(\nu_e + \nu_p)$ resulted in the enhancement of the population of the proton $[-\rightarrow]$ state, causing a negative proton polarization. Similarly microwave photons of energy $h(\nu_e - \nu_p)$ will saturate the transition M [Fig. 2], resulting in a positive proton polarization.

It becomes evident from the above discussion that in order to obtain a significant proton polarization using the dynamic nuclear polarization method, three criteria must be met. First, the external magnetic field used to produce the Zeeman splitting of the electron-proton (e-p) energy levels [Fig. 2], must be extremely homogeneous, to ensure that the microwave photon energy matches the energy difference between the two states involved in the transition N or M throughout the sample (a microwave photon frequency uncertainty of $\Delta\nu = \pm 0.003\%$, requires the external magnetic field homogeneity to be known to $\pm 8 \times 10^{-5}$ T). Second, the external magnetic field, henceforth referred to as the polarizing field, must be large to ensure that thermal excitations kT can not exceed the energy difference between any

two neighbouring spin states. Thus, by eliminating spin state mixing, the polarization process is preserved. Finally, the temperature must be low; this has the effect of decreasing the thermal excitations kT which in turn increases the electron polarization [Eq. 3].

Once the target sample is polarized by the dynamic nuclear polarization method, the microwave irradiation is stopped, the polarizing field is reduced and the sample polarization is maintained in a weaker external magnetic field called the holding field. The lowering of the polarizing field is done to ensure that the perturbations in the incoming and outgoing charged particle trajectories during the experiment are small.

The target polarization in the holding field as a function of time (t) and initial polarization (P_0) can be expressed in the following form:

$$P(t) = P_0 e^{-\frac{t}{\tau}} \quad (6a)$$

where τ is the target polarization decay time in the holding field and is given by the following empirical relation which applies to our experimental conditions [Ref. 10]:

$$\tau = 0.7 \times 10^{17} \frac{B^4}{CT^6} \quad (6b)$$

In the above equation, B is the holding field (in T), C is the concentration of the electron donor material (in molecules \cdot ml $^{-1}$), T is the sample temperature (in K) and τ is the target polarization decay time (in hours). During the experiment, the FST sample (with electron donor concentration of 6×10^{19} molecules \cdot ml $^{-1}$) was cooled to ~ 45 mK in a 0.257 T holding field to attain polarization decay times that were on the average 620 hours, when using [Eq. 6b]. Large polarization decay

times were desirable during the experiment to ensure a relatively stable target polarization throughout the data taking period.

II.3 The He-3/He-4 Dilution Refrigerator

The milliKelvin temperatures necessary to attain a large polarization decay time was achieved by a Helium-3/Helium-4 (He-3/He-4) dilution refrigerator.

II.3.a Liquid Mixture of He-3 and He-4

The operating principle of the dilution refrigerator is based on the unique properties exhibited by mixtures of He-3 and He-4 at low temperatures. To best understand these properties consider the phase separation curve for a liquid He-3/He-4 mixture [Fig. 3] [Ref. 11] at temperatures below 1.5 K.

Below about 0.8 K the liquid mixture spontaneously separates into the two isotope components, one of the phases being rich in liquid He-3 and the other rich in liquid He-4. But since the He-3 phase has a lower density it floats on top of the He-4 rich phase. As the temperature is lowered further, the relative amounts of He-3 and He-4 in the two phases change; below about 40 mK the upper phase is essentially pure liquid He-3 whereas the lower dilute phase is made of liquid He-4 of which 6.4% [Ref. 12] is dissolved liquid He-3.

The fact that in the dilute phase the He-3 solubility does not change from 6.4% as the temperature is lowered to absolute zero is of paramount importance for the success of the dilution refrigerator.

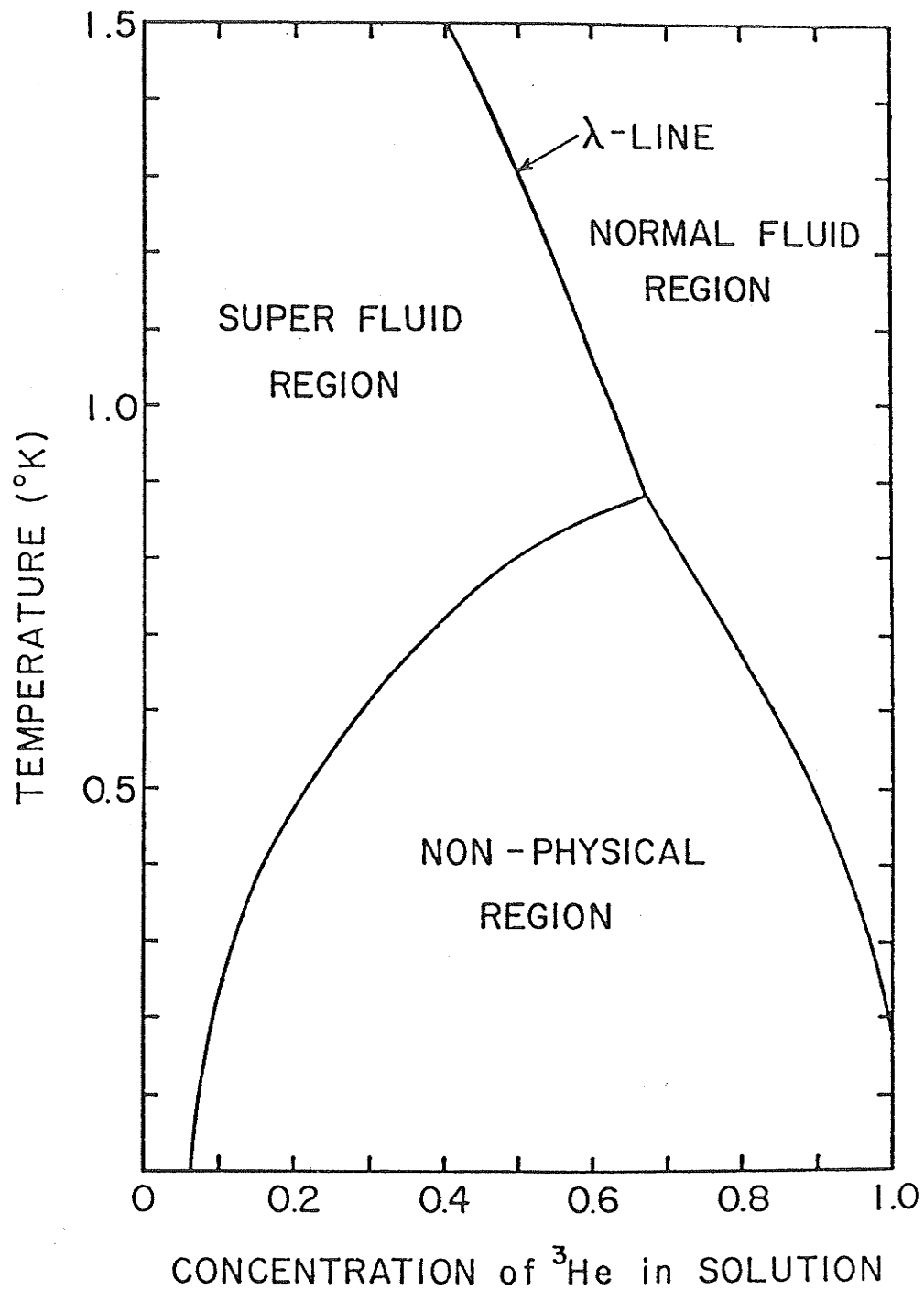


[Fig. 3]

Phase separation curve for a liquid He-3/He-4 mixture below 1.5 K.

II.3.b The Principle of Dilution

Because liquid He-4 has zero nuclear spin, at temperatures below 0.5 K it undergoes a phase transition to a quantum mechanical ground state (Bose condensate) with superfluid properties. Also, since very few phonons are excited the liquid is thermally inert. As a result of this, we may describe the He-4 in the dilute phase as a "supporting medium" for the active He-3 atoms. Thus the upper phase of liquid He-3 is in equilibrium with its own vapor (He-3 atoms in the lower dilute phase).

When atoms of He-3 move downward from the liquid to the dilute phase the temperature is lowered because energy is needed to overcome the interatomic forces. But because the concentration of He-3 atoms in the dilute phase remains constant at 6.4% as the temperature is lowered below 40 mK, the cooling process can be made continuous by recirculating the He-3 atoms from the dilute phase to the pure He-3 liquid phase. This is precisely what is done in a He-3/He-4 dilution refrigerator.

II.3.c Theory of Operation of a Dilution Refrigerator

To describe the cooling that takes place when one mole of He-3 crosses the phase boundary isothermally, consider a vessel (mixing chamber) containing the phase-separated He-3/He-4 mixture in thermal equilibrium at a temperature less than 0.1 K [Fig. 4] [Ref. 11].

Since the upper phase is essentially pure He-3, the molar entropy in this phase is the molar entropy of pure liquid He-3 (s_3) which has been shown experimentally [Ref. 13] to be:

$$s_3 = c_1 RT \tag{7}$$

where c_1 is a constant equal to 2.7 K^{-1} , T is the mixing chamber

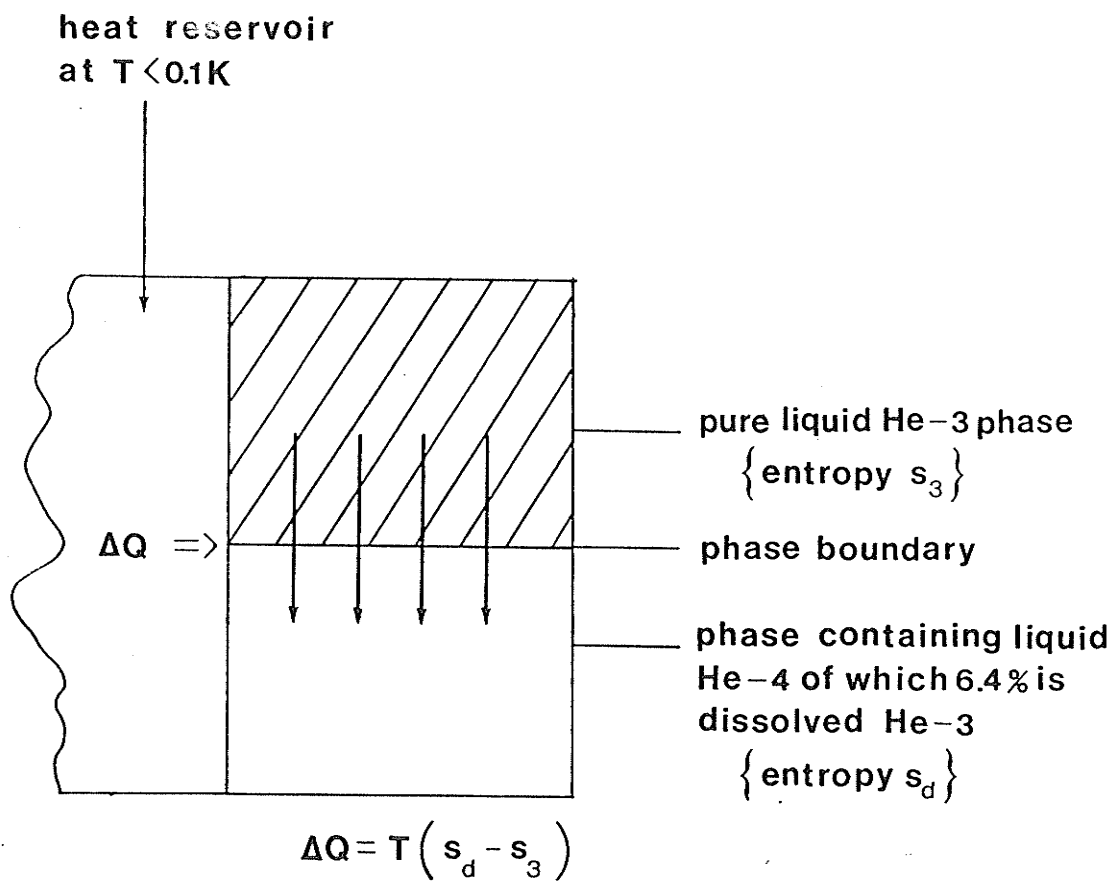


[Fig. 4]

Schematic of the dilution process.

temperature (in K) and R is the gas constant (in $\text{J}\cdot\text{mol}^{-1}\cdot\text{K}^{-1}$). Because in the dilute phase the He-4 is a Bose condensate (thus has zero entropy) the total entropy in the lower phase (s_d) is just the entropy of the He-3 "vapor" which has been theoretically [Ref. 14] and experimentally [Ref. 15] shown to be that of an ideal Fermi gas. Thus the molar entropy in the dilute phase is given by the entropy of a Fermi gas [Ref. 16], which is:

$$s_d = \frac{\pi^2 RT}{2T_F} \quad (8)$$

with

$$T_F = \frac{\hbar^2}{2km_3} \left(\frac{3\pi^2 N}{V} \right)^{2/3} \quad (9)$$

where N is the number of He-3 atoms in the dilute phase, V is the volume occupied by the He-3 atoms in the dilute phase (in m^3), T_F is the Fermi temperature (in K) and m_3 is the effective mass of a He-3 atom in the dilute phase, which is 2.4 times [Ref. 17] that of the He-3 atom mass (in kg). Because 6.4% of the dilute phase is occupied by He-3 atoms then:

$$\frac{N}{V} = 0.064 \left(\frac{\rho_{\text{He-4}}}{m_4} \right) \quad (10)$$

where $\rho_{\text{He-4}}$ is the density of liquid He-4 (in $\text{kg}\cdot\text{m}^{-3}$) and m_4 is the He-4 atom mass (in kg).

Evaluating [Eq. 10], [Eq. 9] and [Eq. 8] we get:

$$T_F = 0.37 \text{ K} \quad (11)$$

and

$$s_d = c_2 RT \quad (12)$$

where c_2 is a constant equal to 13.3 K^{-1} .

If we now assume the mixing chamber to be in thermal contact with a

heat reservoir at a temperature below 0.1 K, [Fig. 4] the amount of heat (ΔQ) that can be withdrawn from the reservoir as one mole of He-3 is transferred from the pure He-3 phase to the dilute phase is:

$$\begin{aligned}\Delta Q &= T\Delta S \\ &= T(s_d - s_3) \\ &= c_3RT^2\end{aligned}\tag{13}$$

where c_3 is a constant equal to 10.6 K^{-1} .

If N_3 moles per second are transferred, the rate of heat extraction \dot{Q} (in $\text{J}\cdot\text{s}^{-1}$) is:

$$\dot{Q} = c_3N_3RT^2.\tag{14}$$

[Eq. 14] applies to the case in which He-3 is withdrawn from the dilute phase and is not returned to the pure He-3 phase. To make the dilution refrigerator continuous, the He-3 atoms in the dilute phase must be removed, cooled and returned to the pure He-3 phase. A means of doing this is shown in [Fig. 5].

To remove the He-3 atoms from the dilute phase, an unbroken column of dilute He-3/He-4 is conducted from the low temperature region ($T < 0.1 \text{ K}$) of the mixing chamber to a higher temperature region of $\sim 0.9 \text{ K}$ called the still. At the temperature of the still, the vapor above the dilute phase is very rich in He-3 so that cold He-3 gas can be removed by pumps and then recompressed at room temperature. The returning He-3 gas is then cooled to 4.2 K when it passes through a tubular heat exchanger in the separator that is in thermal contact with liquid He-4. The He-3 gas is cooled further and liquified when it passes through a tubular heat exchanger in the condenser that is in thermal contact with liquid He-4 at 1.6 K . The liquid He-3 is then cooled to

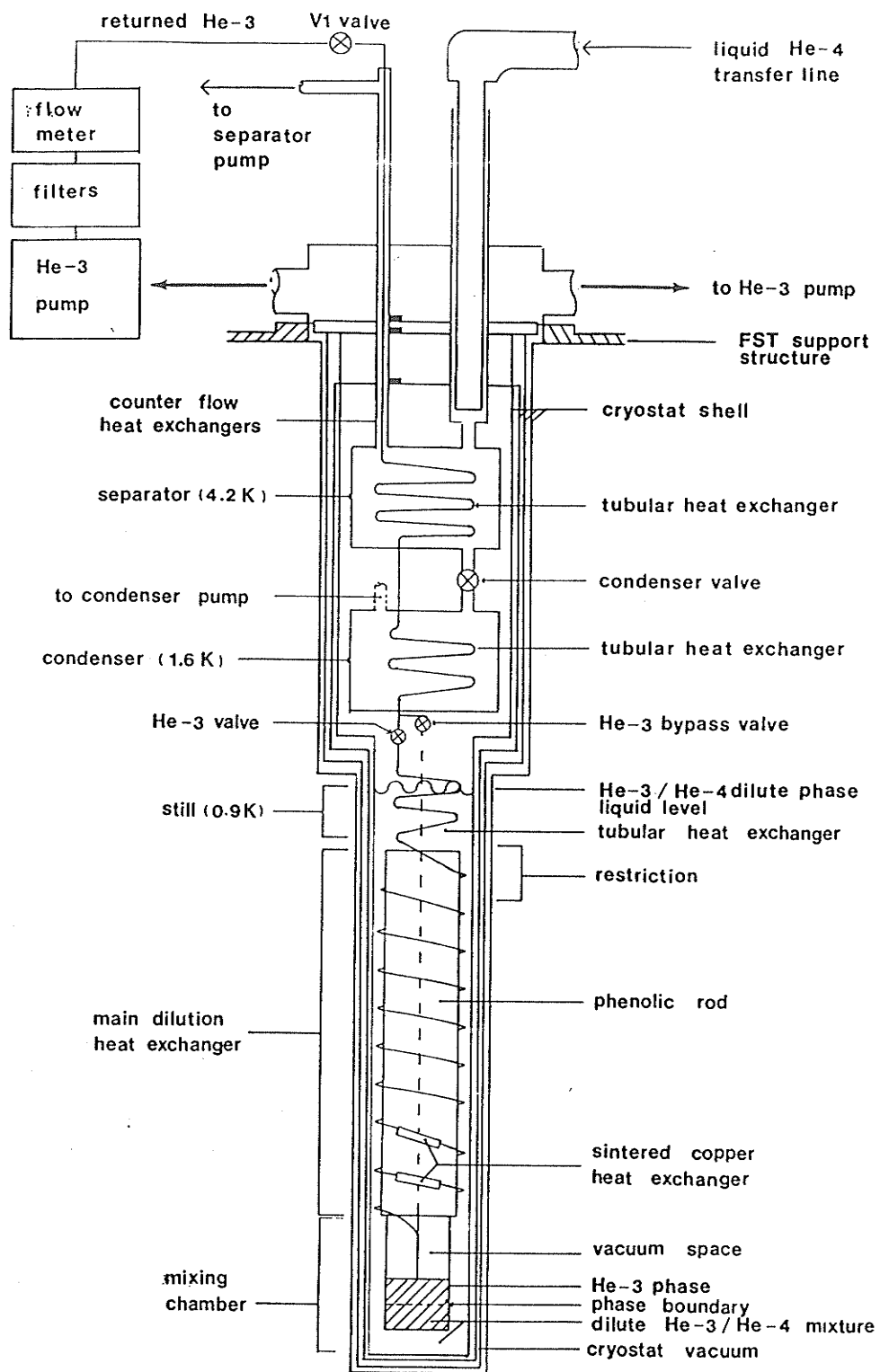


[Fig. 5]

Schematic of dilution refrigerator used in p-p elastic scattering experiment.

approximately the mixing chamber temperature when it traverses the still's tubular heat exchanger, the main dilution heat exchanger and sintered copper heat exchanger, all of which are in thermal contact with the cold He-3/He-4 dilute phase leaving the mixing chamber. The phase boundary is maintained in the mixing chamber by adjusting the amount of He-3 in the system.

The rate of heat extraction from the mixing chamber when it is operating continuously at a temperature below 0.1 K can be calculated using [Eq. 14]. This represents the total heat that can be removed from the surroundings during the dilution process. If we now assume that N_3 moles per sec of pure He-3 is entering the top of the mixing chamber at a temperature $T_i < 0.1$ K and that the dilute phase is leaving the bottom of the mixing chamber at a temperature T_{MC} , then [Eq. 14] can be rewritten for the case of continuous dilution as follows:

$$\begin{aligned} \dot{Q} &= N_3 [h_3(T_i) - h_3(T_{MC})] + \dot{Q}_e \\ &= c_3 N_3 R T_{MC}^2 \end{aligned} \quad (15)$$

with:

$$h_3(T) = \int_0^T c_3(T') dT' \quad (16)$$

where \dot{Q}_e is the external heat load (in $J \cdot s^{-1}$) applied to the mixing chamber. c_3 is the molar specific heat of pure He-3 at constant pressure (in $J \cdot mol^{-1} \cdot K^{-1}$) and h_3 the molar enthalpy of pure He-3 (in $J \cdot mol^{-1}$).

As it is seen in [Eq. 15], the total heat load \dot{Q} that is being

dumped into the mixing chamber is a result of two distinct processes. The first term is due to the He-3 fluid stream whereas the second term, Q_e , is the heat load on the mixing chamber from every other conceivable source. This is referred to as the external heat load and could be from the mixing chamber heater, or radiated heat from the heat shields [Fig. 5], or beam heating, or vibrations or any combination of these.

Using the experimentally [Ref. 18] determined C_3 value for the temperature region below 0.1 K:

$$C_3(T) = c_4 RT \quad (17)$$

in [Eq. 16] we get:

$$h_3(T) = c_5 RT^2 \quad (18)$$

where c_4 and c_5 are constants equal to 2.7 K^{-1} and 1.35 K^{-1} , respectively.

Substituting [Eq. 18] into [Eq. 15] we get the external heat load the mixing chamber can handle, that is:

$$Q_e = c_6 N_3 RT_{MC}^2 - c_5 N_3 RT_i^2 \quad (19)$$

where c_6 is a constant equal to 11.95 K^{-1} .

Setting $Q_e = 0$ in [Eq. 19] gives the low temperature limit that can be reached by the mixing chamber. This is found to be:

$$T_{MC} = 0.336 T_i \quad (20)$$

It becomes evident from the above equation that it is the heat exchanger efficiency (which eventually determines T_i) that governs the performance of the dilution refrigerator.

11.3.d Dilution Refrigerator External Heat Load Limitation

When a dilution refrigerator is used in an experiment to cool the target material to milliKelvin temperatures, it is imperative that the heat deposited in the target (mixing) chamber by the incident beam (as it traverses the PST), be below a heat load that is large enough to cause a substantial rise in the mixing chamber temperature. If this condition is not satisfied, the excess heat load would cause the target material to depolarize, by decreasing the target polarization decay constant [Eq. 6b]. It is seen then, that, the incident beam intensity will limit the magnitude of the polarization decay time.

For small values of Q_e , that is when $T_i \approx T_{MC}$, [Eq. 19] indicates that $Q_e \propto T_{MC}^2$. If one then separates Q_e into two terms:

$$Q_e = Q_h + Q_{ee} \quad (21)$$

where Q_h is the mixing chamber heater power (heat load rate) and Q_{ee} the power due to all other external heat sources. One can then obtain the heat leak from the external sources, Q_{ee} , by plotting Q_h vs T_{MC}^2 for various values of Q_h and then determining $-Q_{ee}$ from the Q_h intercept at $T_{MC}^2 = 0$. Prior to the p-p elastic scattering experiment, a mixing chamber power test, such as the one described above was performed [Fig. 6] at a base temperature (at $Q_h = 0$) of 37 mK and it was determined that the residual heat leak was 47.2 μ W.

During the p-p elastic scattering experiment, the mixing chamber temperature with beam loading was typically at 45 mK.¹ From [Fig. 6], this temperature corresponded to an incident proton beam

¹The mixing chamber temperature was determined from the conductance of a carbon resistor which was located beneath the mixing chamber. The temperature was then extracted from a calibration table.

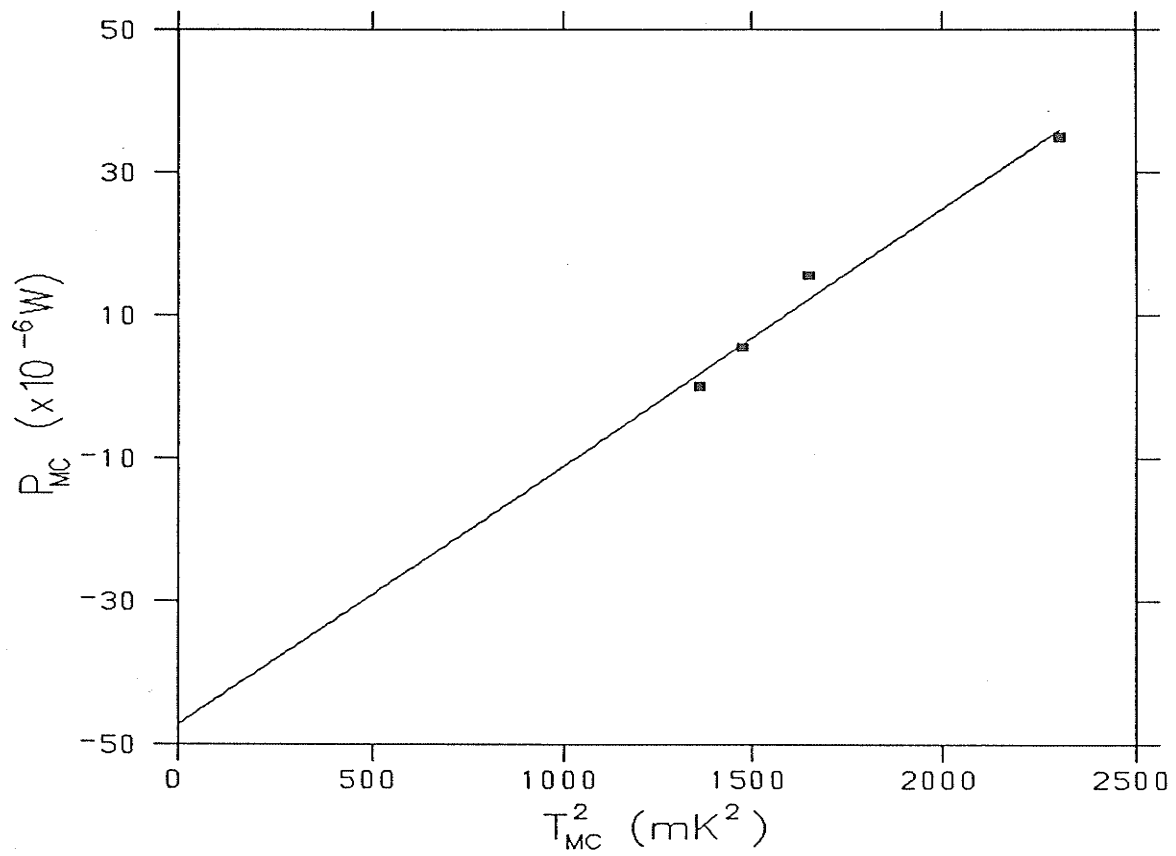


[Fig. 6]

Mixing chamber power test.

heat load rate on the target chamber of $25.7 \mu\text{W}$. Thus the total heat load rate on the mixing chamber due to all of the external heat sources was typically $72.9 \mu\text{W}$.

The polarization decay time as calculated from [Eq. 6b] for a temperature of 37 (45) mK was 1980 (620) hrs. Thus, the 8 mK temperature rise in the mixing chamber as produced by beam heating resulted in a 69% reduction in the target polarization decay time.

II.4 The Frozen Spin Target Apparatus

The FST [Ref. 19] used in the p-p elastic scattering experiment was constructed at the TRIUMF cyclotron laboratory. The target sample was a mixture of 95% 1-butanol [$\text{C}_4\text{H}_{10}\text{O}$], 5% water and the electron donor material EHBA(CrV), chemical formula [$\text{Na}((\text{C}_2\text{H}_5)_2\text{COCO}_2)_2\text{CrO}$] [Ref. 20], with a concentration of 6×10^{19} molecules per ml. The above mixture was frozen into beads of 1.5 mm diameter and stored in a liquid nitrogen (LN2) vessel.

The sample was chosen for its high fractional mass of polarizable protons and long spin-lattice relaxation time. Past experience using this type of sample [Ref. 21] has shown that proton polarization values as high as 0.97 can be reached, previously shown only for propanediol [Ref. 8]. It was also confirmed [Ref. 22] that butanol relaxation times that are longer than the ones for propanediol [Ref. 8] can be obtained.

The main components of the FST system consisted of:

- (a) a He-3/He-4 dilution refrigerator to obtain the milliKelvin temperatures desired for long target polarization decay times thus "freezing" the proton spin orientation;

²Formed when combining sodium dichromate and 2-ethyl-2-hydroxybutyric acid [EHBA].

- (b) a microwave source to polarize the target nuclei using the dynamic nuclear polarization method;
- (c) a magnet assembly that allowed the refrigerator to operate in a very homogeneous and strong magnetic field during the polarizing process and in a weaker holding field during the data taking period of the experiment; and
- (d) a NMR system to measure the target polarization.

II.4.a Procedure Used to Cool the Frozen Spin Target Sample

The following discussion refers to [Fig. 5]. The dilution refrigerator components: separator, condenser, phenolic rod³, vacuum chamber, target basket and the various heat exchangers were all constructed upon a center tube with diameter of 19 mm. Within the space of the central tube ran two NMR cables and a microwave guide which continued to pass through the vacuum chamber below the still to the mixing chamber. The mixing chamber comprised of three compartments: a target basket constructed of 2 mil copper with dimensions of 2 cm wide, 3.5 cm long and 5 cm high, and two vacuum chambers located above and below the target basket [Fig. 7]. The dilution refrigerator was mounted on the FST support structure and remained fixed throughout the course of the experiment. A cylindrical cryostat [Fig. 5] containing three radiation shields within its shell was mounted onto the FST support structure in such way to enclose the dilution refrigerator components. The cryostat was removed to load and unload the target material.

³The phenolic rod had machined grooves that fitted the components of the main dilution unit heat exchanger.

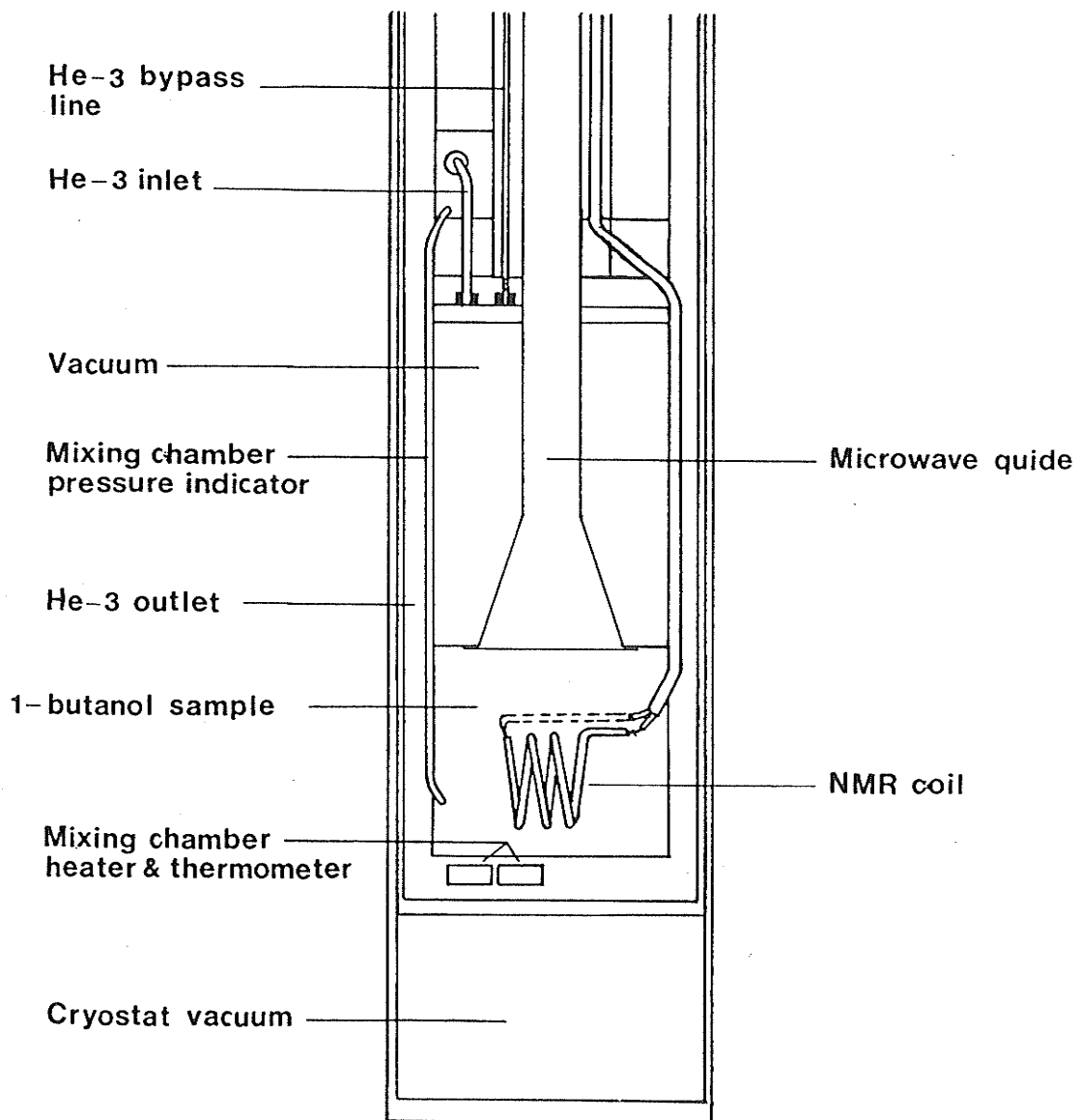


[Fig. 7]

Schematic of target chamber.

On the day before the target loading, the space between the radiation shields within the cryostat (which had not been mounted yet) was pumped on and the inner cavity space (space available for the dilution refrigerator) was filled with LN2. On the morning of the target loading, the cryostat was repumped and topped up with LN2. As the cryostat inner walls continued to cool to LN2 temperatures (~77 K), the target basket was prepared for the target loading. This involved the submerging of the target basket in a LN2 filled cup. Once the temperature of the target basket had stabilized, the LN2 filled cup was lowered to expose a 5 mm diameter hole located at the top of the target basket. The target beads were then loaded into the basket via a thin walled funnel and tube, in a LN2 stream (i.e. spoonfuls of LN2 and target beads). When the target basket was full of beads, the LN2 filled cup used to cool the target basket, was removed and a pre-cooling can was positioned in such a way to enclose the dilution refrigerator components. The pre-cooling can, which was essentially a long dewar flask, was filled with LN2. During this LN2 pre-cooling period, the liquid He-4 transfer line was installed and He-4 gas that had been stored at room temperature in tanks beneath the pump frame was introduced within the He-3 return line to flush away any air that may have been trapped. After the temperature of the dilution refrigerator components had stabilized, the pre-cooling can was removed from underneath the dilution refrigerator, the LN2 within the cryostat inner cavity space was removed and the cryostat was mounted onto the FST support structure. Once the cryostat was installed, the He-4 gas flow within the He-3 line was stopped and the He-3 space (space between cryostat inner wall and

dilution refrigerator) was pumped on to remove any remaining LN2 and air. The separator was pumped on and liquid He-4 transfer commenced when the pressure in the He-3 space was reduced enough to use a diffusion pump. Once the separator temperature began to decrease, the condenser was pumped on and the condenser valve was opened. As the liquid He-4 level within the condenser increased (monitored by a superconductive wire), an automatic condenser valve controller was activated to maintain the desired operating level. When the separator and condenser reached a temperature colder than the mixing chamber temperature (~ 77 K), a mixture of He-3/He-4 gas that had been stored at room temperature beneath the pump frame was introduced into the He-3 return line. The gas mixture was then circulated (path through dilution refrigerator is indicated by a solid line in [Fig. 5]) when the V1 and He-3 bypass valves were opened. Once the entire He-3/He-4 gas inventory was condensed power was supplied to the still heater. The heat shields in the meantime were also cooled by conduction from the bottom plate of the condenser and cold He-4 gas that was pumped out of the separator. As the separator and condenser approached their operating temperatures 4.2 and 1.6 K, the circulating gas mixture reduced the mixing chamber temperature from 77 to 1.6 K. Note though, that it was by pumping on the liquid He-4 that enabled the condenser to be lowered below the liquid He-4 boiling temperature of 4.2 K. To lower the mixing chamber temperature below 1.6 K, the circulating gas path was changed by closing the He-3 bypass valve and opening the He-3 valve, such that it now entered the still tubular heat exchanger and main dilution heat

exchanger. By continuing to circulate the He-3/He-4 gas mixture, the mixing chamber was cooled to the phase separation point, where it began to operate in dilution mode. A minimum mixing chamber temperature was attained by making small adjustments to the He-3/He-4 gas flow rate.

It took eight hours to cool the mixing chamber temperature from 77 to 1.6 K and an additional four hours to achieve an operating temperature of ~45 mK. A typical cool down curve for the dilution refrigerator when operating in dilution mode is illustrated in [Fig. 8].

II.4.b Procedure Used to Attain and Maintain the Frozen Spin Target Sample Polarization

To polarize the dilution refrigerator's target sample, a magnet assembly consisting of a room temperature coil (above) and superconducting solenoid (below) was raised such that the target basket (chamber) was located at the center of the superconducting solenoid [Fig. 9a]. The mixing chamber was warmed to 1.6 K by stopping the He-3/He-4 circulation and letting the refrigerator come to equilibrium with the condenser temperature. The superconducting solenoid was then turned on to produce a field of 2.55 T with homogeneity of $\pm 5 \times 10^{-5}$ T over a volume of 100 cm^3 (the solenoid homogeneity specifications were verified using NMR probes). At this temperature the area under the NMR absorption curve was measured to calibrate the NMR system (to be discussed in the following section). The target sample was then cooled to ~ 0.1 K and then polarized by the dynamic nuclear polarization method by irradiation with microwave photons of energy appropriate to obtain the desired target spin orientation. Polarization would then take place at a temperature estimated at 0.2 or 0.3 K. A polarization curve typical for the experiment is illustrated in [Fig. 10].

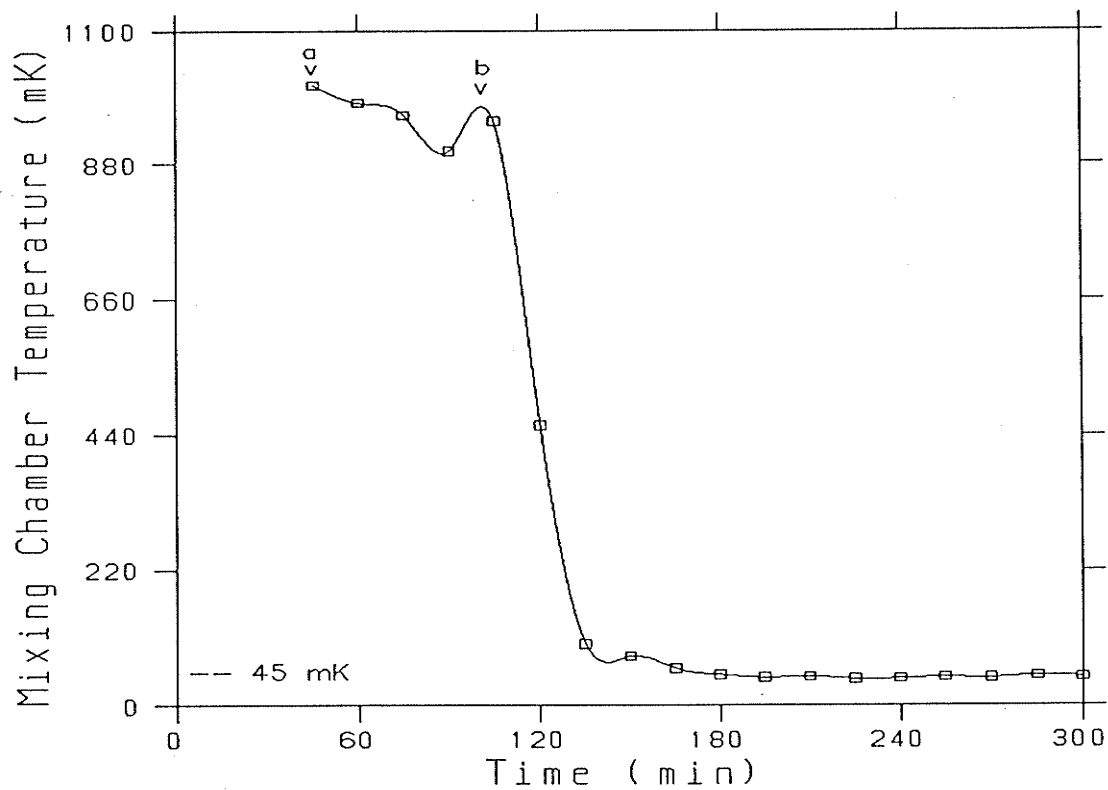
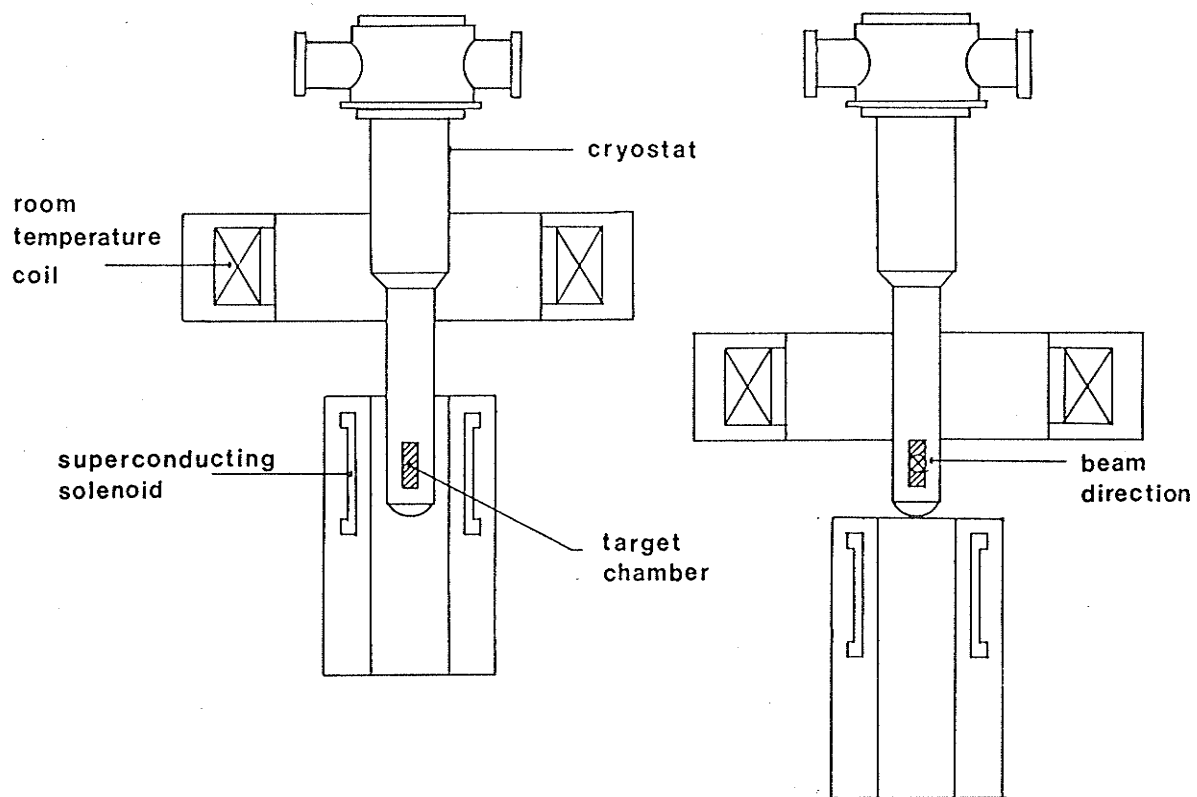


[Fig. 8]

Cool down curve of mixing chamber. At point "a" the refrigerator began to operate in dilution mode (~1 K). At point "b", a flow restriction valve was closed by a quarter turn. This enabled the refrigerator to stabilize at ~45 mK after 2 hours.



(a) Polarizing mode.

(b) Data taking mode.

[Fig. 9]

Magnet arrangement used in experiment.

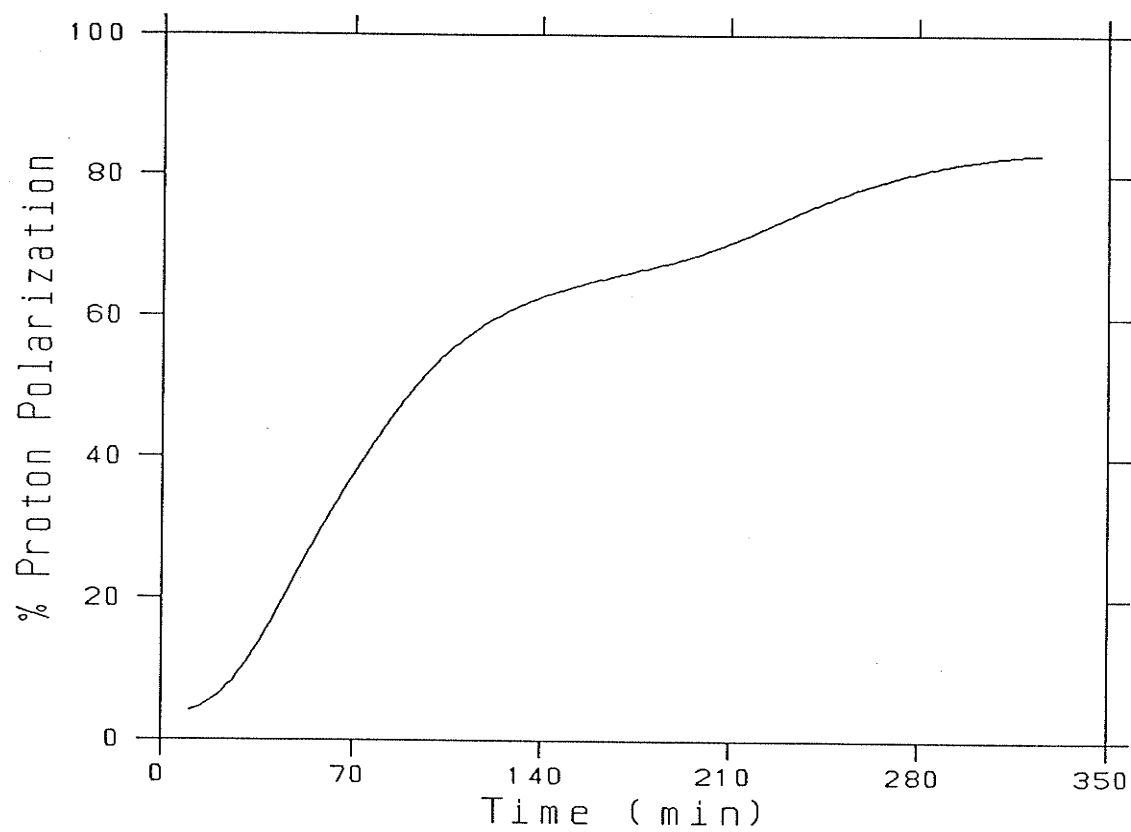


[Fig. 10]

A typical polarization curve obtained by the FST using the dynamic nuclear polarization method. The sample of 1-butanol was polarized in a field of 2.55 T at 1.6 K.

After approximately four hours of polarizing the microwaves were "turned" off and the refrigerator was allowed to cool to ~45 mK. The room temperature coil was energized with a current of 500 A and the entire magnet assembly was positioned such that the target chamber location was in the middle of the gap between superconducting solenoid and room temperature coil [Fig. 9b]. The target polarization was maintained in a holding field of 0.257 T.

The holding field was monitored using two Hall probes placed at fixed locations in the space between the room temperature coil and the superconducting solenoid. An original requirement was that the holding field be stable to ± 1 part in a thousand or to ± 0.25 mT.

11.5 Nuclear Magnetic Resonance

When a proton is placed in a static external magnetic field \vec{B}_0 , the proton's magnetic moment $\vec{\mu}$ and hence the spin precess about the magnetic field with an angular frequency of

$$\omega_0 = \gamma B_0 \quad (22)$$

where

$$\vec{\mu} = \gamma \hbar \vec{s} \quad (23)$$

regardless of the angle between $\vec{\mu}$ and \vec{B}_0 . In the above equation, B_0 is the magnitude of the external magnetic field, \hbar is Planck's constant and γ is the proton gyromagnetic ratio. The value of ω_0 is called the Larmor precession frequency of the proton in the static magnetic field \vec{B}_0 .

Consider now a system composed entirely of protons. In the presence of the static external magnetic field $\vec{B}_0 = B_0 \hat{k}$, the Hamiltonian for the interaction between each proton magnetic moment and the field

\vec{B}_0 is given as

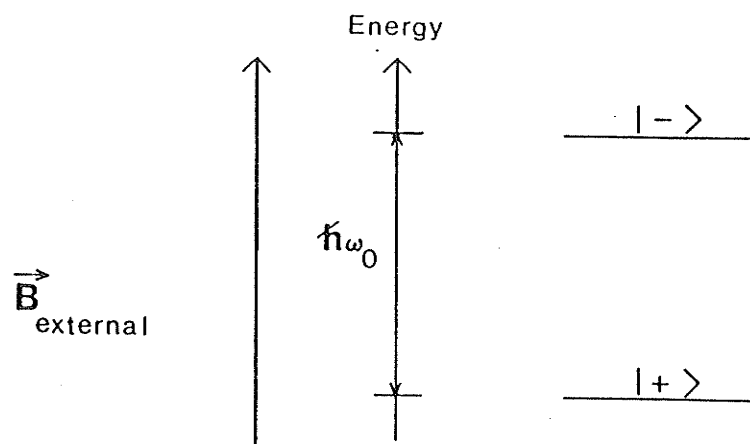
$$\begin{aligned} H &= -\vec{\mu} \cdot \vec{B}_0 \\ &= -\gamma \hbar B_0 S_z \end{aligned} \quad (24)$$

where

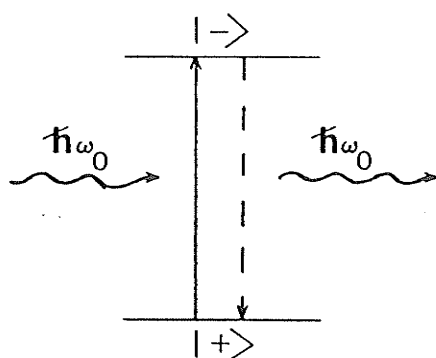
$$S_z = \left| \vec{s} \cdot \hat{k} \right| . \quad (25)$$

Because protons are spin 1/2 particles, S_z has two allowed values: $-1/2$ and $1/2$. Incorporating these two possible S_z values in [Eq. 24] we see that the protons in the system can occupy one of two energy states $| - \rangle$ or $| + \rangle$, depending on the value of S_z [Fig. 11a]. A transition from one proton spin state to the other can be produced by either emission or absorption of a photon of energy $\hbar\omega_0$, which is equal to the separation energy between the two spin states [Fig. 11b]. Because the amount of energy that must be absorbed by a single proton in the $| + \rangle$ spin state to undergo the upward transition to the $| - \rangle$ spin state is $\hbar\omega_0$, the relative populations of the two spin states can be determined from the amount of energy the system can absorb, at frequency ω_0 . (Note that the protons in the $| + \rangle$ spin state must be excited to the $| - \rangle$ spin state, in order to perform the polarization measurement).

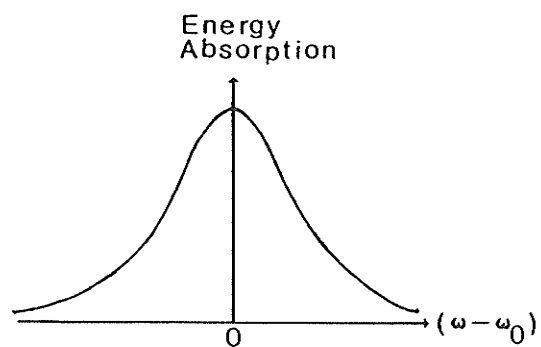
Since it is more realistic to represent the energy level states in [Fig. 11a] with a finite width (this finite width arises from the proton spin-spin collisions within the system which limits the lifetime of a given spin state), the sample proton polarization is related to the area under the sample energy absorption curve for electromagnetic irradiation that is scanned about the proton Larmor precession frequency ω_0 [Fig. 11c]. The frequency scanning is necessary to ensure that most



(a) Energy level diagram for proton system.



(b) Allowed transitions.



(c) Energy absorption spectrum.

[Fig. 11]

Energy level diagram of polarized proton states in static external magnetic field.

of the protons occupying the $|+ \rangle$ state have at one time or another have absorbed a quantum of energy with the appropriate frequency to undergo the upward transition to the $|- \rangle$ state. The NMR system uses this principle to produce a signal that is proportional to the sample polarization.

II.5.a Theoretical Consideration of the NMR Polarization Measurement

When a NMR system is used to measure the proton polarization of a given sample, the proton depolarization is achieved by a coil that is embedded in the sample [Fig. 7]. Let us once again consider the previously described proton system with the addition that the now embedded coil is perpendicular to the static external magnetic field \vec{B}_0 . When a current flows in the coil, a magnetic field \vec{B}_1 will be produced whose direction is along the coil's longitudinal axis and is perpendicular to the field \vec{B}_0 . The net effect of this field will be to introduce an additional torque, causing the proton magnetic moment vectors (which were originally aligned with and precessing about the magnetic field \vec{B}_0) to precess about the total field $\vec{B} = \vec{B}_0 + \vec{B}_1$ at some angle with respect to their previous alignments. Because the magnitude of the magnetic field \vec{B}_1 is oscillating in time with angular frequency ω , the total field \vec{B} precesses about \vec{B}_0 with angular frequency ω . When the resonance condition $\omega = \omega_0$ is met, the precession of the total field \vec{B} and the proton spins will be in phase, and radio frequency (rf) energy will be strongly absorbed by the sample; this is expressed below as

$$\text{rf power absorption} = - \vec{M} \cdot \frac{d\vec{B}_1}{dt} \quad (26)$$

where \vec{M} is the sample magnetization of the proton system, given as

$$\vec{M} = \frac{1}{V} \sum_{i=1}^n \vec{\mu}_i \quad (27)$$

with n being the number of protons in the volume V of sample and $\vec{\mu}_i$ being the individual proton magnetic moment.

As rf energy is absorbed by the sample at resonance $\omega = \omega_0$, changes in the sample magnetization and hence the sample polarization will occur as a result of proton depolarizations. The NMR system detects these changes in the sample magnetization by measuring the sample magnetic susceptibility $\chi(\omega)$, which for small rf excitation is given by

$$\vec{M} = \chi(\omega) \vec{B}_1 \quad (28)$$

where

$$\chi(\omega) = \chi'(\omega) - i\chi''(\omega). \quad (29)$$

Since the amount of rf energy absorbed by the sample at resonance $\omega = \omega_0$ is proportional to the sample polarization and since the relationship [Ref. 23] between rf energy absorption and $\chi(\omega)$ is

$$\text{rf power absorption} = 2B_1^2 \chi''(\omega) \quad (30)$$

the NMR system uses the absorptive term of the sample magnetic susceptibility, $\chi''(\omega)$, to perform the polarization measurement. Because not all of the protons see the same magnetic field due to differing local magnetic environments within the sample, the rf of the embedded coil is scanned about the proton Larmor precession frequency and the term $\chi''(\omega)$ is averaged over all the scanned frequencies. Thus, the target polarization (P) is proportional to

$$\int_0^{\infty} \chi''(\omega) d\omega . \quad (31)$$

The direct absolute calibration of [Eq. 31], which is the NMR polarization signal, requires knowledge of geometrical factors, the gain of various amplifiers, etc. This difficulty is overcome by comparing the rf energy absorbed with the sample highly polarized to the energy absorbed when the proton spin system is in thermal equilibrium at the temperature of a helium bath. Thus,

$$P = E \cdot P_{TE} \quad (32)$$

with

$$E = \frac{\int_0^{\infty} \chi''(\omega) d\omega}{\int_0^{\infty} \chi_{TE}''(\omega) d\omega} \quad (33)$$

where E is the enhancement in the NMR polarization signal over the thermal equilibrium signal and P_{TE} is the thermal equilibrium polarization given by [Eq. 1a]. During the course of the p-p elastic scattering experiment, proton polarizations as high as 84% were measured with the NMR system.

11.5.b Difficulties in Using the Nuclear Magnetic Resonance System to Determine the FST Polarization

It was pointed out in the introduction that the target polarization must be known to an absolute accuracy of $\pm 2\%$, if the $A_{yy}(\theta)$ parameter is to be measured to ± 0.03 (absolute). Systematic errors in the

NMR system arise from:

- (a) deviation from linearity of the NMR signal with target polarization;
- (b) non-uniformity of the polarization over the target volume, which could arise from the inhomogeneities in the microwave irradiation;
- (c) NMR system sampling of different parts of the target with unequal weight, indicating a polarization that is different from the average value of the sample; and
- (d) thermometer calibration near 1 K when the NMR system was calibrated with the TE method.

These errors limited the NMR [Ref. 19] system used in the $A_{yy}(\theta)$ experiment to attain an absolute calibration of no better than $\pm 4\%$ [Ref. 1].

Because of the above uncertainty in the target polarization, an independent absolute measurement of the FST polarization was required to calibrate the NMR system. This was done by performing a p-p elastic scattering experiment at an energy and angle where the p-p analyzing power is accurately known.

The main concern for the remainder of this thesis will be the p-p elastic scattering experiment, whose apparatus is discussed in the following chapter.

A list of the frozen spin target operating parameters is tabulated in [Table 1].

[Table 1]

Operating Parameters of Frozen Spin Target

Target volume (5 cm high, 2 cm wide and 3.5 cm thick)	35 cm ³
Target sample	1-Butanol beads
Bead diameter	1.5 ± 0.3 mm
EHBA concentration	6 x 10 ¹⁹ molecules/ml
Operating temperature (typically)	45 ± 5 mK
Flow rate of circulated helium gas ⁴	1.53 ± 0.02 l/min
Mixing chamber external heat load rate	72.9 μW
Holding field	0.257 T
Holding field reproducibility	± 0.25 mT
Polarizing field	2.55 T
Polarizing field homogeneity	± 5 x 10 ⁻⁵ T
Positive polarization microwave frequency	70.550 ± 0.002 GHz
Negative polarization microwave frequency	71.020 ± 0.002 GHz
Thermal equilibrium magnetic field	2.54 T
Thermal equilibrium temperature	1.6 K
Opening angle	Horizontal ± 93° Vertical + 11°, -8°

⁴Estimated concentration to be 40% He-4 and 60% He-3 gas, at STP.

CHAPTER III

EXPERIMENTAL APPARATUS

III.1 Introduction

The experiment was carried out at the TRIUMF cyclotron laboratory in the proton hall, via beamlines 4A and 4A/2 with an experimental layout as illustrated in [Fig. 12].

The unpolarized primary proton beam energy was monitored by a beam energy monitor (BEM) system consisting of two six element range counters placed behind the forward $\pm 17^\circ$ (lab) arms of the primary proton beam polarimeter. Because the primary beam was unpolarized the beam polarimeter was used in the experiment for intensity monitoring purposes only.

The secondary proton beam (which had a polarization vertical to the scattering plane) was produced when the incident protons were elastically scattered from a liquid hydrogen (LH2) or graphite (C) target (during the $A_{yy}(\theta)$ experiment, the above targets were replaced with a liquid deuterium target to produce the secondary neutron beam). The LH2 target was used when the experiment was performed using 497 MeV protons and the C target was used when using 512 MeV protons. Producing the secondary proton beam in this way, allowed the proton beam incident on the FST to be comparable in intensity to the neutron beam used in the $A_{yy}(\theta)$ experiment.

The secondary proton beam was collimated through a 3.37 m long iron and lead collimator and emerged at the 9° (lab) port, whereas the primary proton beam was dumped into a steel beam stop that was inserted in the 0° (lab) collimator port. The secondary proton beam polarization

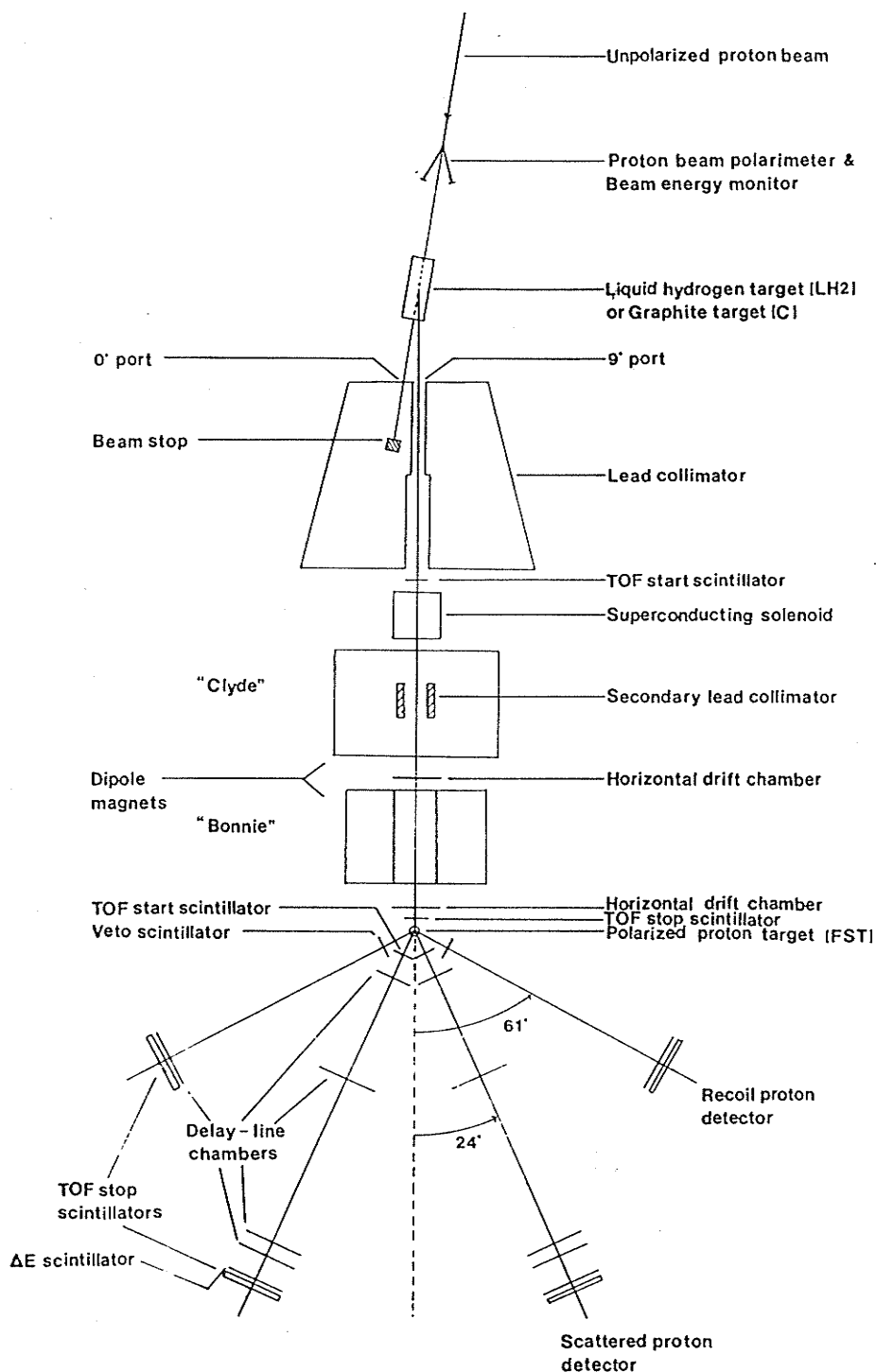


[Fig. 12]

Experimental layout used in the p-p elastic scattering experiment to calibrate the FST polarization. The diagram is not to scale. The apparatus depicted above was originally designed for the "Test of Charge Symmetry Breaking" experiment and was used in the $A_{yy}(\theta)$ experiment as well.

was rotated by 90° (into the horizontal) when the beam travelled axially through a superconducting solenoid magnet at the exit of the collimator. This was done to ensure that the observed scattering asymmetry was due to the FST polarization only [see Chapter IV]. A time-of-flight (TOF) system consisting of two scintillators placed as far apart as possible was used to select the protons incident on the FST. The dipole magnet "Clyde" was used to correct the solenoid magnetic field deflections of the secondary beam protons. The dipole magnet "Bonnie" was used to steer the secondary proton beam so as to illuminate the vertical extent of the target cell in three consecutive steps. Two horizontal drift chambers with active areas of 8 cm by 8 cm were originally set up upstream of the FST to estimate the position where the protons impinged on the FST via track reconstruction. But, because of the non-linear proton trajectories between the two drift chambers, only the horizontal drift chamber nearest to the FST was used for FST image reconstruction [see section IV.2.a.4].

The scattered and recoil protons originating in the FST were detected in coincidence in two left-right symmetric detection systems, which allowed first order cancellation of systematic errors arising from differences in left and right scattering angles, solid angles and detection efficiencies. Each detection system for scattered protons at 24° (lab)⁵ consisted of two functionally distinct systems supported by a boom: a TOF system for determining proton velocity consisting of a TOF

⁵These are the nominal scattering angles. During the experiment the detector systems were placed on the floor at angles adjusted for the holding field deflections [see Table 11].

start scintillator close to the FST and a TOF stop scintillator placed 2.934 m away, and four delay line chambers for track reconstruction of which three had an active area of 58 cm by 58 cm and one (the first one) of 30 cm by 30 cm. Each detection system for the coincident recoil protons at 61° (lab)⁶ consisted of two elements: a delay line chamber of active area 58 cm by 58 cm supplied x- and y- coordinates for the recoil proton track reconstruction from the FST scattering center and a large charged particle scintillator (of dimensions 105 cm high by 36.8 cm wide) functioning as a TOF stop scintillator for the recoil proton TOF. The scattered proton TOF start scintillator was used as the time reference. A scintillator with a 10 cm by 18 cm rectangular hole was located near the FST to veto recoil protons that had scattered from the FST cryostat shell.

III.2 Primary Proton Beam

III.2.a Beam Transport

After extraction from the cyclotron, the proton beam bends out of the main cyclotron magnet and travels along beamline 4V [Fig. 13]. The "combination magnet", 4VCM, adjusts the magnetic field in this region so that the extracted protons are directed down the beamline. The quadrupole magnet triplet 4VQ1, 4VQ2 and 4VQ3 then focuses the beam at a point inside the bending magnet, 4VB1, which directs the proton beam along beamline 4A.

⁶These are the nominal scattering angles. During the experiment the detector systems were placed on the floor at angles adjusted for the holding field deflections [see Table 15].

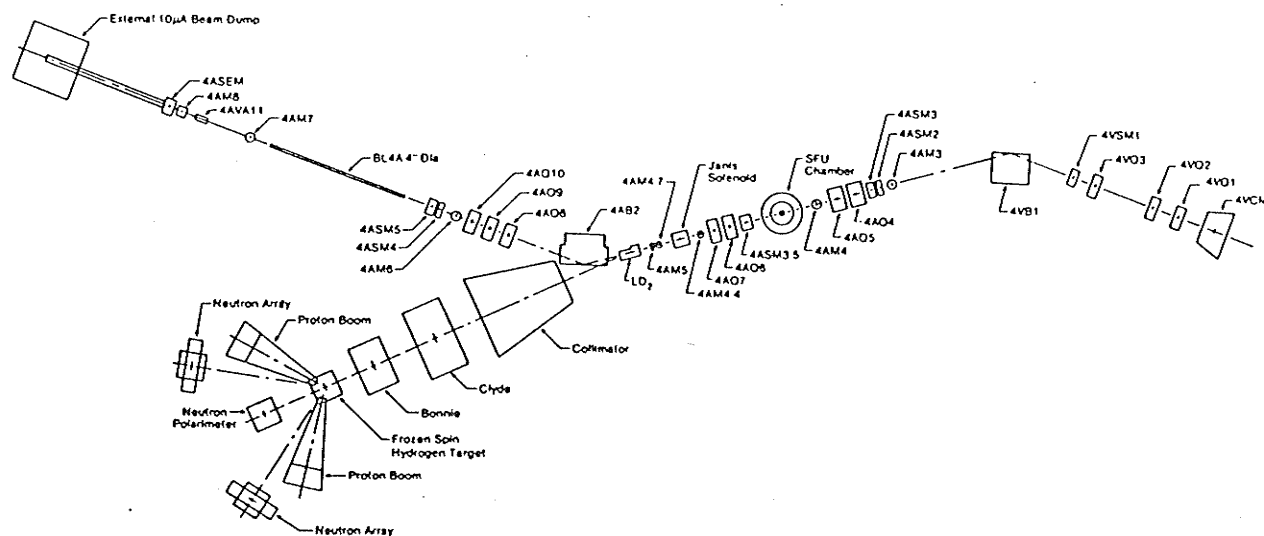


[Fig. 13]

Proton beam transport system. For a more detailed illustration, one may refer to the TRIUMF users handbook.

Due to the presence of stray magnetic fields (from the cyclotron), the steering magnet 4VSM1 was used to keep the extracted beam "on axis".

The beam transport along beamline 4A was monitored by remotely inserting various beam profile monitors (4AM3, 4AM4 and 4AM5) and the beam was kept on axis by adjusting the beam with several vertical and horizontal steering magnets (4ASM2 and 4ASM3). The beam was focussed by using the quadrupole magnet doublets (4AQ4-4AQ5 and 4AQ6-4AQ7).

The bending magnet, 4AB2, was turned off to allow the primary proton beam to be dumped into the 0° (lab) collimator port and to extract the secondary proton beam with minimal magnetic field deflections.

III.2.b Beam Energy and Intensity Monitoring

The proton beam energy monitoring system was located within the 1.5 m diameter Simon Fraser University (SFU) scattering chamber. The primary proton beam energy stability was monitored throughout the experiment by a system composed of a twin detector assembly (set symmetrically about the beam axis) viewing a kapton foil located 6.32 m upstream from the LH2 (or C) secondary beam production target center. The primary proton beam energy was measured by observing the p-p elastic scattering coincident events from the kapton foil at $\pm 17^\circ$ (lab) and determining the proton stopping distribution in a range counter assembly.

The beam energy monitor (BEM) sensitivity to changes in beam energy was ± 35 keV [Ref. 24] for a beam of 500 MeV. The BEM's could not determine the absolute beam energy because of the non-negligible uncertainty in the range-energy relations.

A coincidence was achieved when the scattered proton was detected

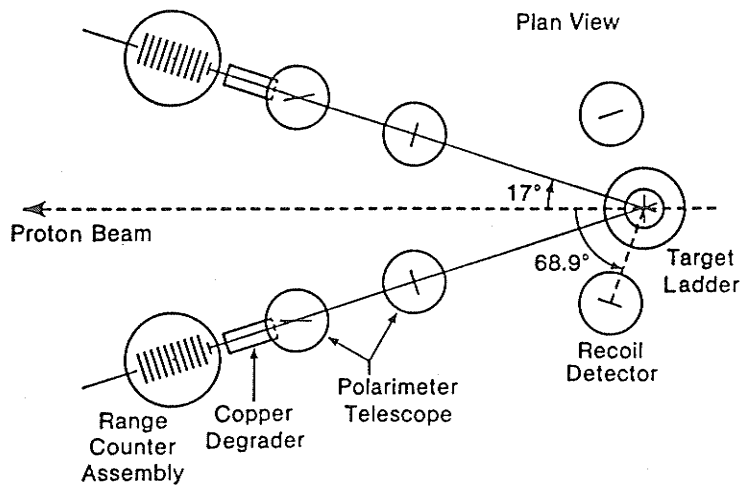
in the left⁷ (right) 17° (lab) primary proton beam polarimeter arm and the recoil proton was detected in the right (left) 68.9° (lab) recoil detector [Fig. 14a]. The choice of angles was determined by the maximum of the p-p analyzing power curve at 500 MeV.

Each of the polarimeter forward arms consisted of: two scintillators (A_1, A_2) for the polarimeter telescope, a copper degrader and six scintillators (counters), B_1 through B_6 , that had copper plates sandwiched between them. Counter B_1 was reduced in area to minimize the loss of protons from the range telescope due to multiple scattering. The scintillator A_2 was rotated by 68° lab to make the polarimeter insensitive [Ref. 25] to minor shifts (± 2 mm) in the beam centroid. The recoil detectors consisted of a single scintillator, A_3 .

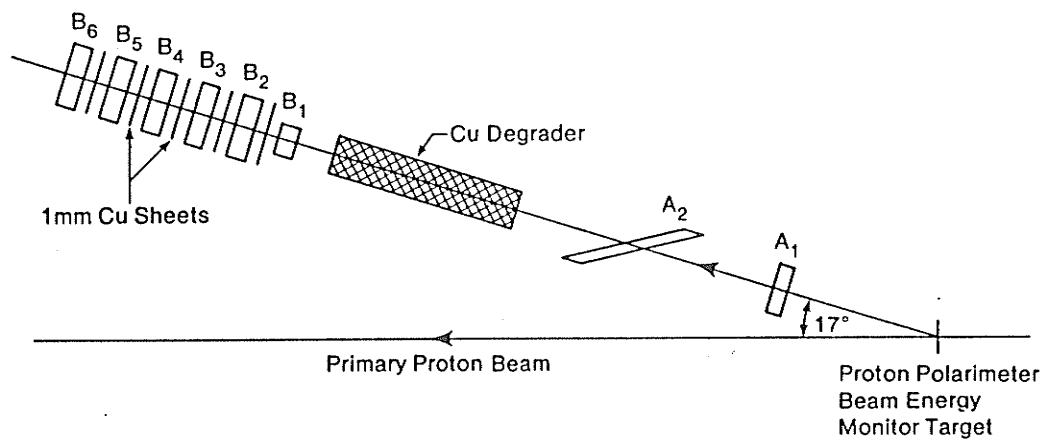
The range counter assembly coincidence requirement for a particle stopping in counter B_i was $(A_1 \cdot A_2 \cdot A_3 \cdot B_1 \dots B_i)$. The coincidences were electronically scaled as $(A_1 \cdot A_2 \cdot A_3 \cdot B_1), (A_1 \cdot A_2 \cdot A_3 \cdot B_1 \cdot B_2), \dots, (A_1 \cdot A_2 \cdot A_3 \cdot B_1 \dots B_6)$ [Fig. 15] and the number of protons stopping in the counter B_i were determined by taking the difference between successive scalers (using software).

The proton beam intensity was determined using the left and right polarimeter arms and knowledge of the p-p differential cross section, polarimeter target thickness and solid angle.

⁷Left is with respect to an observer looking along the primary proton beam direction, positioned at the kapton target [Fig. 14a].



(a) Plan view of polarimeters and beam energy monitor apparatus.



(b) Beam energy monitor details for a single polarimeter arm.

[Fig. 14]

Schematic of the BEM-Polarimeter apparatus.

The polarimeter accidental coincidence rate was determined [Fig. 15] by delaying the scattered proton counter (A_1 , A_2) signals by a single beam burst (43.5 ns) with respect to the recoil counter (A_3) signals.

During the course of the experiment the primary proton beam current was maintained at 110-140 nA which corresponds to a beam intensity of $(6.9 - 8.8) \times 10^{11}$ particles/sec. The corresponding secondary beam intensity was $(3.8 - 4.8) \times 10^6$ particles/sec. At these beam intensities, it required on the average ninety minutes of data collection to attain 100,000 p-p coincident events on tape that had taken place within the FST.

The specifications of the polarimeter-BEM assembly are tabulated in [Table 2].

III.3 Secondary Proton Beam

III.3.a Beam Production

The experiment was performed using two different primary proton beam energies of 497 and 512 MeV. This corresponded to a secondary proton beam energy of 469 and 501 MeV at the FST center. The second p-p elastic scattering experiment was not performed at 497 MeV due to the use of a different secondary proton beam production target. The target change was introduced to reduce the target changing over period between the A_{yy} experiment and the second p-p elastic scattering experiment, thus allowing more time for data collection.

Using a primary proton beam energy of 497 MeV, the secondary proton beam was produced by elastic scattering from a LH2 target. The target contained LH2 at a temperature of 17.1 K and a pressure of 166.2 kPa.

[Table 2]

Operating Parameters of Polarimeter - Beam Energy Monitor Assembly

Kapton target thickness	4.175 mg/cm ²
Beam energy monitor:	
B ₁ counter distance from kapton target	104.8 cm
Number of counters	6
Thickness of counters	1 cm
Thickness of Cu separators	1 mm
Counter size: B ₁	5 mm by 5 mm
B ₂ -B ₆	1 cm by 1 cm
Main degrader thickness: using LH2 production target	143.4 mm
using C production target	151.0 mm
Polarimeter telescope:	
Number of counters	2
Counter A ₂ size	1 cm by 2.5 cm
Counter A ₂ distance from kapton target	77.47 cm
Counter A ₂ solid angle	0.16 msr
Counter A ₂ polar angle range	+ 0.37°
Counter A ₂ azimuthal angle range	+ 1.26°
Counter A ₂ central angle	17°
Counter A ₂ rotation angle	68°
Recoil detector:	
Counter A ₃ size	2 cm by 1 cm
Counter A ₃ distance from kapton target	20.32 cm
Counter A ₃ solid angle	4.84 msr
Counter A ₃ polar angle range	+ 1.41°
Counter A ₃ azimuthal angle range	+ 3.0°
Counter A ₃ central angle	68.9°

The target chamber was 19.7 cm long (target thickness of 1.39 g/cm^2) by 50.8 mm in diameter, with walls of 0.25 mm stainless steel and end windows of 0.051 mm. When in operation the target was separated from the cyclotron vacuum by 0.13 mm stainless steel windows.

When the experiment was performed using 512 MeV primary protons, the secondary proton beam was provided via $^{12}\text{C}(p,p)$ scattering. The target consisted of 5 discs of graphite each of 50.80 mm diameter with thickness of 1.65 mm. The discs were spaced 50.80 mm center to center to give an overall length of 20.49 cm and thickness 1.49 g/cm^2 .

III.3.b Beam Collimation

The secondary proton beam used in the p-p elastic scattering experiment emerged at 9° (lab) to the primary beam direction through a 3.37 m long collimator assembly [Fig. 12].

The collimator was constructed of steel pipes that were welded to a steel frame filled with lead. The pipes were built in two sections. The downstream section was 1.5 m long and 12.8 cm in diameter while the upstream section measured 1.8 m long and 10.2 cm in diameter (the downstream section diameter was deliberately made larger than the upstream section diameter to reduce radiation at the secondary beam production target location). Unused ports were shut with steel plugs. In the 9° (lab) collimator port, rectangular apertures were cut into the collimator steel inserts, of which the upstream (downstream) pipe section contained 6(5), ranging from 39.1 mm horizontal by 18.6 mm vertical upstream to 46.1 mm horizontal by 32.2 mm vertical downstream.

The distance between the center of the LH2 (or C) target and the entrance and exit of the collimator was 2.92 m and 6.29 m respectively.

A second collimator was placed in the dipole magnet "Clyde", to eliminate protons that had undergone multiple scattering from the walls of the inner structure of the superconducting solenoid magnet (to be discussed in the next section) and upstream collimator walls. The secondary collimator consisted of lead bricks that were stacked into a 61 cm long space to form a 51.3 cm wide by 52.0 mm high⁸ aperture and were positioned 1.8 m downstream from the main collimator 9° (lab) port exit.

III.3.c Beam Polarization Rotation

Since the primary proton beam is unpolarized and the secondary proton beam is produced by elastic scattering, the secondary beam polarization (P_B) can be expressed by [Ref. 26]:

$$P_B = A_y(\theta) \quad (34)$$

where $A_y(\theta)$ is the analyzing power. The beam polarization was positive (i.e. vertical to the incident beam direction and pointing up) since $A_y(\theta) > 0$ and the protons scattered to the left. Using [Ref. 3] ([Ref. 27]), [Eq. 34] and $\theta = 9^\circ$ (lab), P_B was determined to be 0.41 (0.24) for a primary beam energy of 497 (512) MeV, which corresponded to an energy of 493 (510) MeV at the center of the LH2 (C) target.

A superconducting solenoid magnet [Fig. 12] with 0.26 m bore length and 2.104 T.m integrated field strength capability was used to precess the vertical proton polarization by 90° (clockwise) into the horizontal plane.

⁸This value was quoted as 50.8 mm in [Ref. 24], but the value used in the text was the result of an August 13, 1986 survey performed by Dr. C. Davis.

Conservation of parity [Ref. 26] then ensures that the beam polarization has no influence on the observed FST left-right scattering asymmetry.

The superconducting solenoid specifications are tabulated in [Table 3]. The upstream end of the solenoid was located 16 cm from the 9° (lab) collimator port exit, and the downstream end was 4.7 cm from the upstream face of the dipole magnet "Clyde". Because the magnetic field of "Clyde" extended into the solenoid's field and vice versa, a net force would be exerted on the solenoid's coils. To minimize this effect, a 0.95 cm thick soft iron field clamp was built on to the solenoid support structure. The reduction in the tail of the solenoid magnetic field distribution [Fig. 16] at the location of the field clamps (± 37 cm) is clearly visible. The field clamp consisted of four rectangular plates. The two side plates had dimensions of 22.86 cm by 72.39 cm, whereas the front and back plates had dimensions of 22.86 cm by 54.1 cm. A hole of radius 2.86 cm was centered in both the front and back plates to ensure the passage of the secondary proton beam. The field clamp hole radius was oversized by 0.32 cm to minimize secondary beam multiple scattering when entering and exiting the solenoid.

The solenoid integrated field strength necessary to rotate the secondary proton beam polarization by 90° was calculated from [Ref. 28]:

$$\int B \cdot d\ell = \frac{\pi}{2} \frac{\hbar c}{(mc^2)} (pc) \frac{1}{\mu_p} \quad (35)$$

where mc^2 is the rest mass of the proton (in MeV), pc is the proton momentum at the solenoid center (in MeV), $\hbar c$ is Planck's constant times the speed of light (in MeV·m) and μ_p is the proton magnetic moment (in MeV·T⁻¹).

[Table 3]

Superconducting Solenoid Specifications

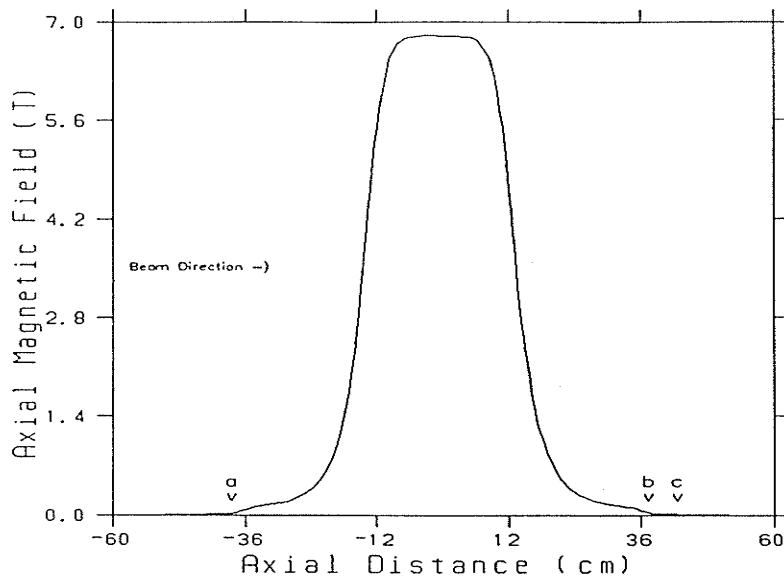
Cryostat:

Max. overall length	68.2 cm
Max. diameter	48.8 cm
Max. overall height	97.0 cm
Room temp. bore tube diameter	5.08 cm
Bore length	26.0 cm
Max. liquid helium volume	15.8 litres
Useful liquid helium volume	8.5 litres
Max./useful liquid nitrogen volume	10.4 litres
Liquid helium boil off ⁹ rate	4.2%/hr
Liquid nitrogen boil off ⁹ rate	3.3%/hr

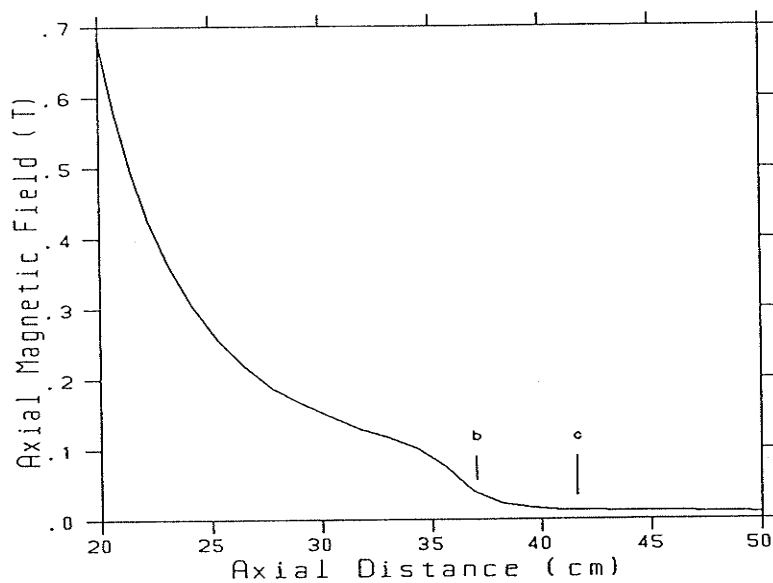
Magnet:

Max. central field	7.0 T
Current for max. central field	54.8 A
Homogeneity	$\pm 5\%$ of central field over 18 cm axis (-9 cm to + 9 cm)
Persistence (nominal)	1 part in 10^4 /hr
Inductance	23.25 H
Stored energy at full field	35 kJ
Switch heater current	50-60 mA
Switch heater resistance	100 Ω
Time to energize magnet	0.75 hrs

⁹When solenoid was in persistent mode.



(a) Axial magnetic field at superconducting solenoid.



(b) The scale at the downstream edge of the solenoid axial magnetic field has been expanded to illustrate the reduction in the magnetic field at the field clamp location.

[Fig. 16]

Axial magnetic field of superconducting solenoid. The field clamps are located at points "a" and "b", whereas point "c" indicates nearest face of "Clyde".

According to the solenoid specifications [Ref. 29], a central magnetic field of 7 T is obtained at a persistent mode current of 54.8 A and the $\int B \cdot d\ell = 2.104 \text{ T}\cdot\text{m}$. The persistent mode current (in A) required to produce a $\int B \cdot d\ell$ necessary to perform a 90° rotation in beam polarization is given by the relation

$$\frac{\int B \cdot d\ell}{2.104} \times 54.8 \quad (36)$$

The corresponding central axial magnetic field (in T) is determined from

$$\frac{\int B \cdot d\ell}{2.104} \times 7 \quad (37)$$

During the 497 (512) MeV data collection period of the experiment (which corresponded to an secondary beam energy of 473 (506) MeV at the superconducting solenoid center) the solenoid was operated [Ref. 30] at a persistent mode current of 51.7 (53.8) A and central axial magnetic field of 6.6 (6.8) T. The time required to place the solenoid in persistent mode from its room temperature state took between 2-3 hours depending on the number of times the solenoid quenched.

A field mapping of the superconducting solenoid when operating in a persistent mode current of 53.8 A was performed by using an alignment laser (directed along the solenoid axis) and a 10 T axial-field Hall probe. As the probe scanned along the axis of the solenoid, as indicated by the laser, measurements were made over regions for which the field was 0.01 T or more. The central field was at 6.8 T and the results of the field mapping are illustrated in [Fig. 16]. The spin precession angle for 506 MeV protons (energy of protons at solenoid when using a 512 MeV primary proton beam) was found to be $89.8^\circ \pm 1.8^\circ$.

III.3.d Beam Steering

When the secondary proton beam travelled axially through the superconducting solenoid a 0.06° horizontal deflection ($\delta\theta_{\text{obs}}$) was observed at the FST ($\delta\theta_{\text{obs}}$ was determined from two runs¹⁰, one with the superconducting solenoid on and one with it off, then observing the shift in the proton trajectories at the FST location). This implied a 0.1° deviation between the solenoid magnetic axis and the beam central axis. The solenoid misalignment angle θ_s was determined from the following equation:

$$\delta\theta_{\text{obs}} = \frac{q}{p} \times \sin\theta_s \times (\int B \cdot d\ell)_{\text{solenoid}} \quad (38)$$

where $\delta\theta_{\text{obs}}$ is the deflection angle observed at the FST due to the solenoid only, q is the charge of the proton (in coul.) and p is the known proton momentum at the FST center (in $\text{kg}\cdot\text{m}\cdot\text{s}^{-1}$).

The dipole magnet "Clyde" was used as a horizontal steering magnet to correct the secondary beam proton trajectories from the deflection that they had obtained from the solenoid misalignment.

Because the vertical dimension of the secondary proton beam was smaller than the vertical dimension of the target cell, the dipole magnet "Bonnie" was operated as a vertical steering magnet to direct the beam to illuminate different vertical sections of the target cell.

During the course of the experiment the magnetic field of "Bonnie" was changed at the start of each run, to illuminate a different

¹⁰The data collection period required to fill a single magnetic tape with information concerning $\sim 100,000$ p-p scattering events at the FST is referred to as a run.

vertical section of the target cell. Three separate consecutive runs were taken to illuminate the entire target cell.

The DAC settings and corresponding total deflection angles¹¹ for the dipole magnets "Clyde" and "Bonnie" are tabulated in [Table 4] and [Table 5] respectively. The DAC unit was a digital control of the magnet current, whose setting could be manually adjusted. A DAC setting of 0.01 for the dipole magnet "Bonnie" ("Clyde") corresponded to a $\int B_x \cdot dz$ ($\int B_y \cdot dz$) of 0.0024 (0.0033) T·m .

III.3.e Time of Flight

The experiment determined the target polarization from the observed scattering asymmetry and known analyzing power for p-p elastic scattering. Because the secondary beam was contaminated with lower and higher energy particles that had resulted from p-p inelastic scattering and reactions in the secondary beam production target, a TOF system was set up upstream of the FST [Fig. 12] to isolate the protons of interest [see section IV.2.a.1].

The TOF system, with specifications tabulated in [Table 6], was set up such that the start and stop scintillators had a maximum possible separation. This ensured maximum peak separation in the TOF spectrum.

Each start and stop scintillator was attached to a single photomultiplier tube via a light guide that contained four optical

¹¹How the total deflection angle was calculated from the solenoid misalignment and dipole magnetic deflections will be discussed in the following chapter.

[Table 4]

DAC Settings of "Clyde" and Corresponding Total Deflection Angles

DAC Setting	Secondary Beam Production Target	$\int B_y \cdot dz$ (T·m)	Horizontal Deflection Angle (in degrees)
0.02	LH2	0.0066	0.024
0.03	LH2	0.0099	0.037
	C	0.0099	0.035
0.04	LH2	0.0132	0.049

[Table 5]

DAC Settings of "Bonnie" and Corresponding Total Deflection Angles

DAC Setting	Secondary Beam Production Target	$\int B_x \cdot dz$ (T·m)	Vertical Deflection Angle (in degrees)
0.00	C	0.0000	0.000
0.01	C	0.0024	0.024
0.01 ¹²	C	-0.0024	-0.023
0.02	LH2	0.0048	0.051
0.05	C	0.0120	0.121
0.05 ¹²	C	-0.0120	-0.121
0.07	LH2	0.0168	0.177
0.10	C	0.0240	0.243
0.10 ¹²	C	-0.0240	-0.244
0.11	LH2	0.0264	0.279
0.15	LH2	0.0360	0.380

¹²The polarity of "Bonnie" was interchanged.

[Table 6]

Secondary Proton Beam TOF System Specifications

Start scintillator:

Material	Pilot-u scintillator
Width	4 cm
Height	2.8 cm
Thickness	0.08 cm
Distance from FST center	648.2 cm
Distance from collimator	7.8 cm
Distance from solenoid field clamp	8.2 cm
Light guide strip length	5 cm
Light guide rod: Length	5 cm
Inner two strip thickness	0.8 cm
Outer	0.6 cm

Stop scintillator:

Material	Pilot-u scintillator
Width	6 cm
Height	4 cm
Thickness	0.08 cm
Distance from FST center	47.7 cm
Light guide strip length	5 cm
Light guide rod: Length	2 cm
Inner two strip thickness	1.2 cm
Outer	0.8 cm

strips with the same length. In each case, signals from the photomultiplier tube were fed into a time to digital converter (TDC) using a constant fraction discriminator (CFD). The TOF was determined from the difference in the TDC outputs. A schematic diagram of the photomultiplier tube signals to the TDC, for either start or stop scintillator, is illustrated in [Fig. 17].

Because the CFD comes up often in the experimental electronic diagrams the reason for using this type of pulse discrimination will be explained here.

When charged particle interacts with the scintillation detector, the output pulse signal from the photomultiplier tube has an amplitude that is related to the energy deposited by the particle in the detector. A discriminator is used to select pulses that correspond to particle energies that are of interest. Two common discriminators are of the integral and differential type [Fig. 18]. The integral discriminator serves to pass pulses that have an input pulse height greater than the "threshold bias". The differential discriminator however, yields an output pulse only if the pulse falls between prescribed upper and lower "threshold" levels. The difficulty in using such discriminators arises from the relative timing dependence of the output pulse on the amplitude of the input pulse. This is illustrated in [Fig. 19] for the case of an integral discriminator.

Improved timing resolution is achieved with a constant fraction discriminator that is insensitive to the input pulse amplitude. The CFD functions with the following principle [Fig. 20]. Suppose a 20% fractional triggering level is used. The detector anode current pulse (input pulse) is first attenuated to 20% of its initial amplitude. The input pulse is also

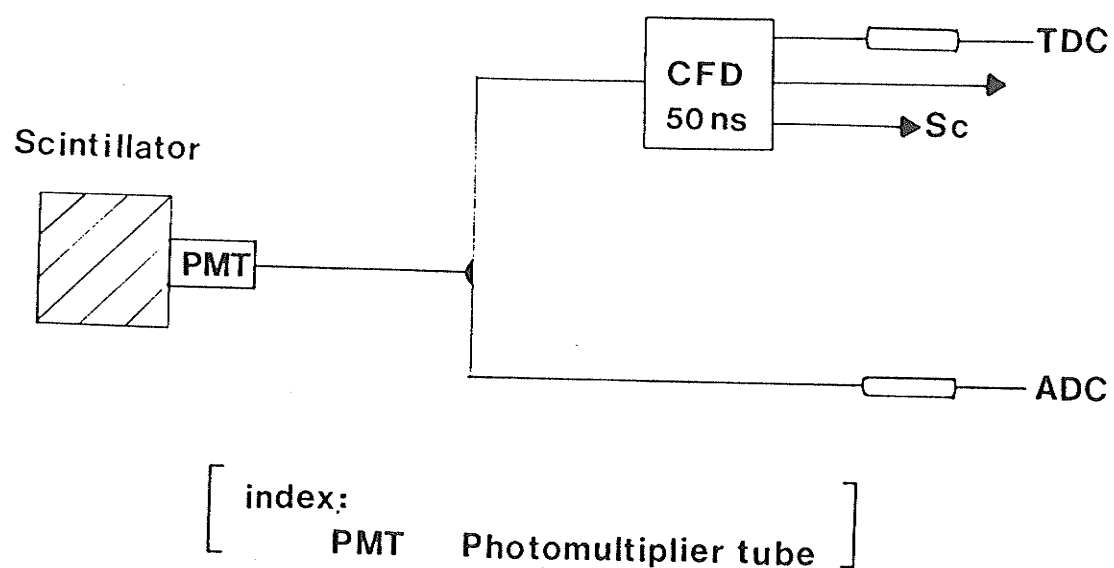
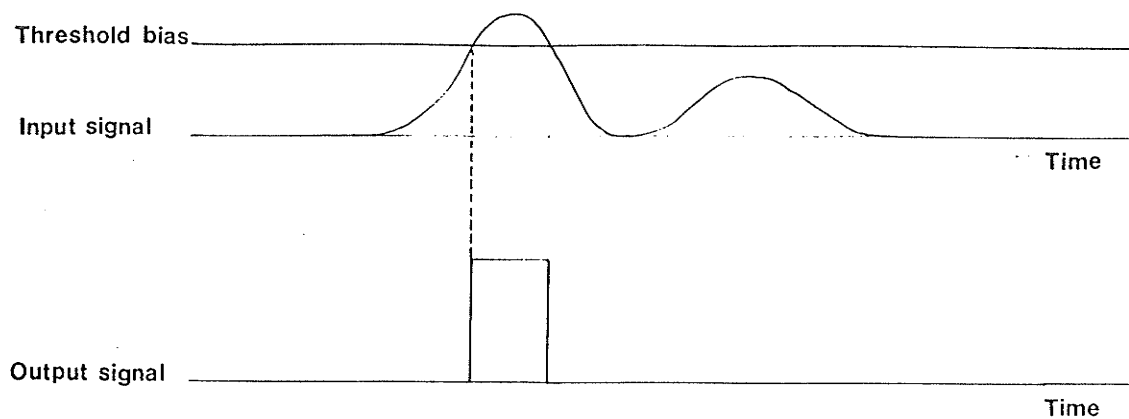
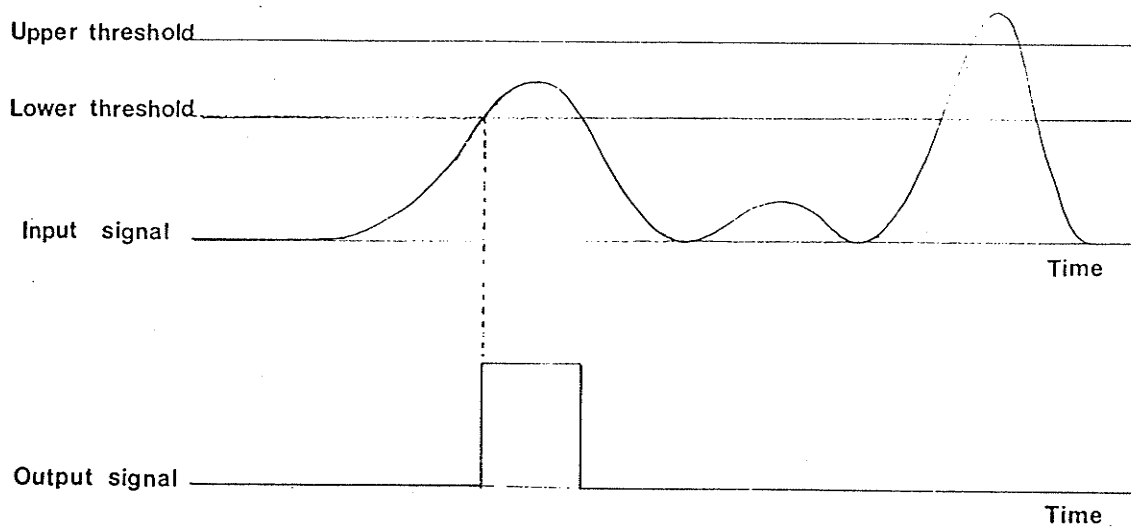


[Fig. 17]

Schematic diagram of electronics for either start or stop scintillator signals. The 50 ns indication in the CFD corresponds to the width of the output pulse. The ADC abbreviation is used for the analog to digital converter module.



(a) Action of an integral discriminator.



(b) Action of a differential discriminator.

[Fig. 18]

Types of pulse discrimination.

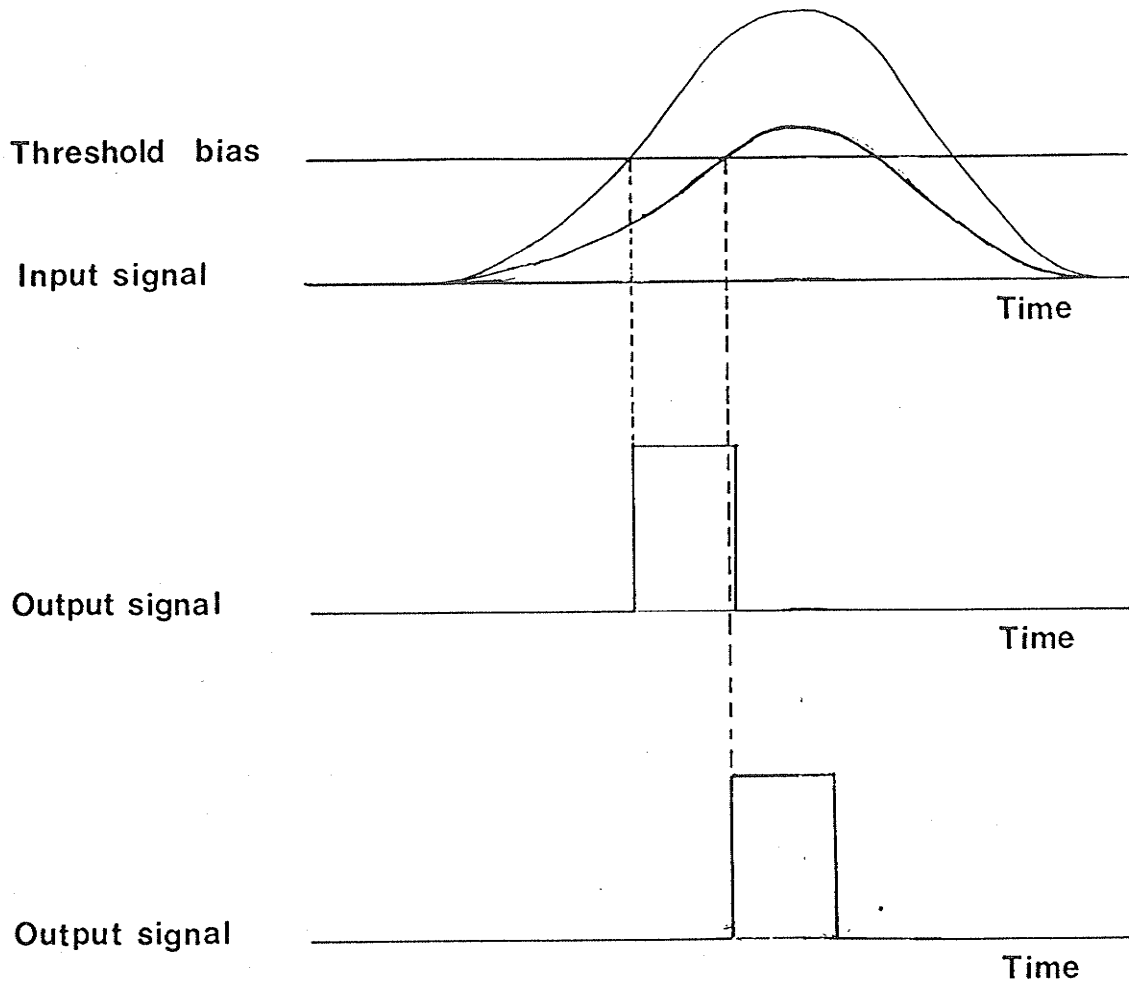


[Fig. 19]

The effect of input pulse of differing amplitude on the timing of the output pulse from an integral discriminator.

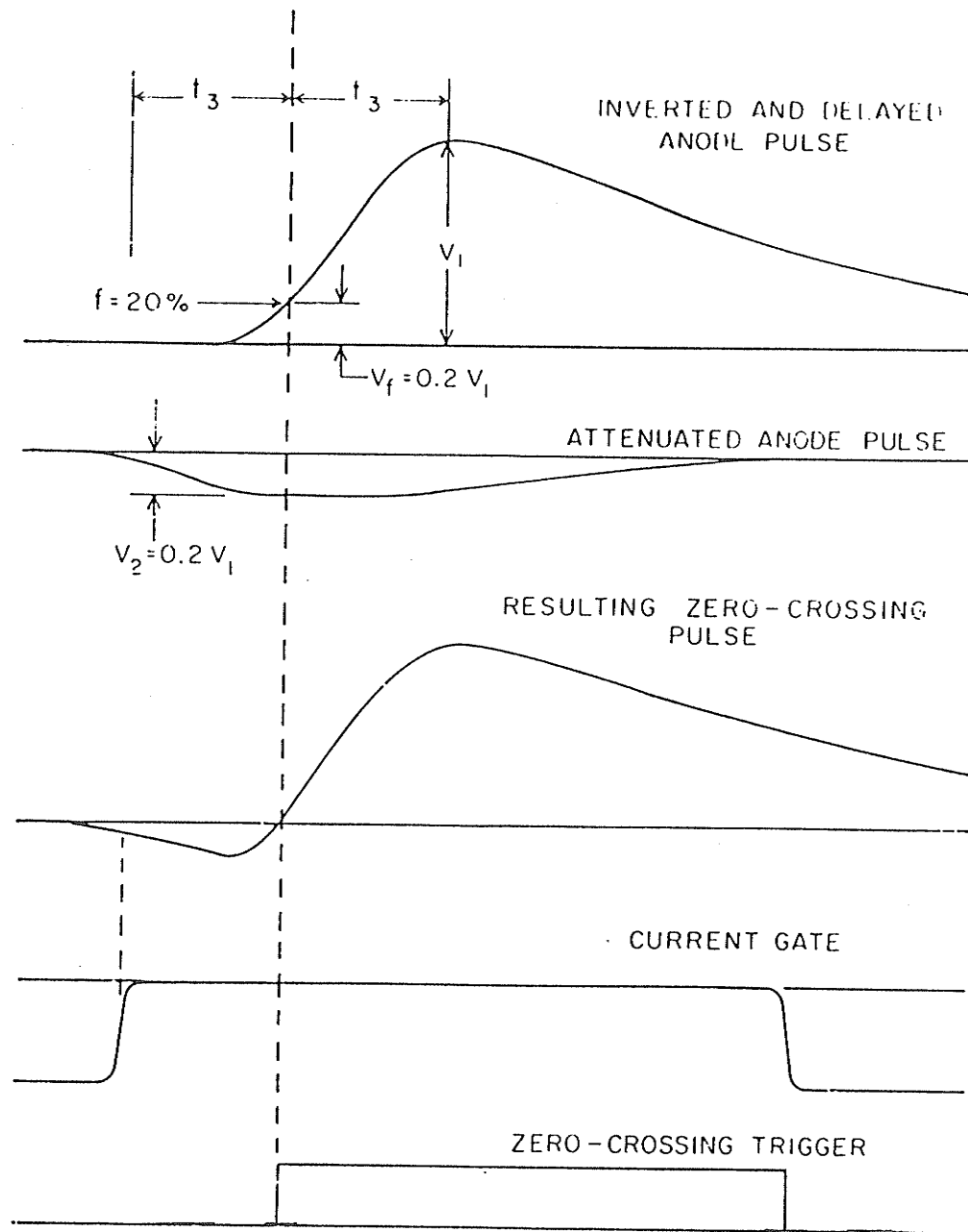


[Fig. 20]

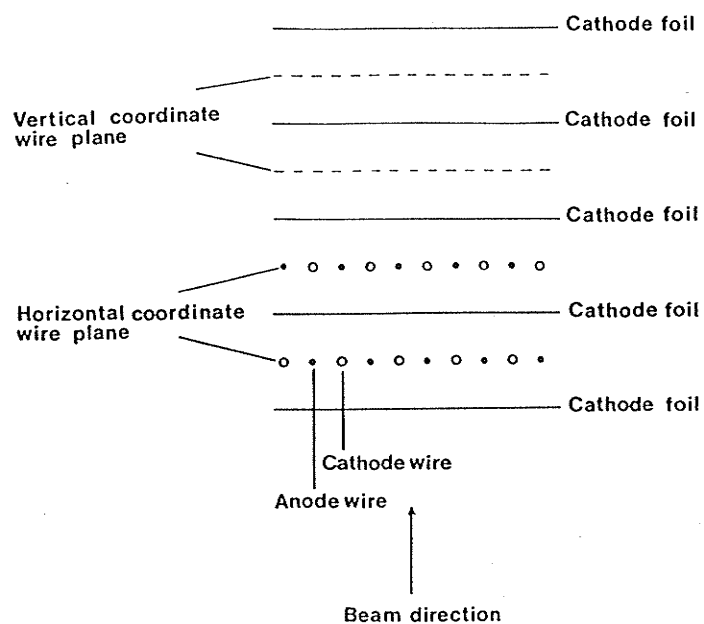
CFD principle of operation.

delayed by a time interval, t_3 , and inverted. The delay time t_3 is chosen such that the 20% phase point on the delayed and inverted pulse lines up with the maximum amplitude of the attenuated pulse. These two pulses are then added to produce the bipolar constant fraction timing pulse. As can be seen, the attenuated pulse exactly cancels the delayed and inverted pulse at the 20% phase point on the delayed pulse. A trigger circuit, which is enabled by the current gate signal, is arranged to trigger an output pulse at the zero-crossing point of the bipolar pulse. This corresponds to sensing the arrival of the same fraction of charge (i.e. 20%) regardless of the input pulse amplitude, for input pulses of the same shape.

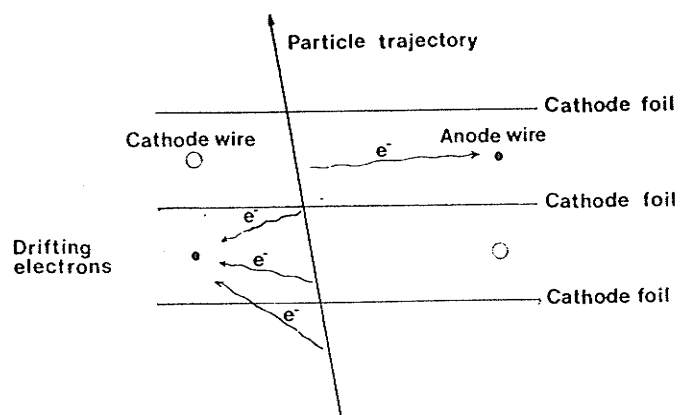
III.3.f FST Image Reconstruction

Of the two horizontal drift chambers, located 67.2 cm and 315.6 cm upstream of the FST [Fig. 12], only the drift chamber nearest to the FST was used to depict the FST image, see [section IV.2.a.4] for more details. The chambers were chosen for their high rate capabilities.

The internal construction of the drift chamber [Ref. 31] consisted of four wire planes and five cathode foils. Each wire plane was positioned at the midpoint between adjacent cathode foils [Fig. 21a]. Two of the four wire planes were used to provide the horizontal position readout and the other two were used for vertical position readout. Each wire plane consisted of sixteen pairs of alternating anode and cathode wires that had an adjacent anode and cathode wire spacing of 5 mm. The cathode and anode wires were made of 2 mil diameter Au-Be-Cu (mostly copper) and $\sim 1/2$ mil diameter gold plated tungsten wires respectively. The active area of each drift chamber was 8 cm by 8 cm.



(a) Schematic of horizontal drift chamber.



(b) Principle of operation of a drift chamber.

[Fig. 21]

The horizontal drift chamber.
Diagrams are not to scale.

The space between the cathode foils contained a gas whose composition was 70% argon and 30% isobutane. The separation distance between foils was 6.4 mm.

When a charged particle travels through the drift chamber [Fig. 21b] it liberates electrons and positive ions as a result of the argon gas ionization. The electrons begin to accelerate toward the anode wire under the influence of the electric field, and after a time $\sim 10^{-11}$ sec they reach an approximately constant drift velocity (typically 4 cm/ μ s [Ref. 31]). The magnitude of the drift velocity will depend on the electric field and pressure of the gas. As the electrons continue to travel through the gas they will begin to spread out due to diffusion, multiple scattering and secondary ionization. Once a signal that the particle has passed is received, the drift chamber then measures the spatial position of an ionizing particle from the electron drift times for the anode wires that are struck [Ref. 32].

The main drift chamber gas component is argon chosen for its high specific ionization, large multiplication (the additional charge released due to secondary ionization) at a relatively low working voltage, and its low cost. Because the photons that are emitted in the deexcitation of excited argon atoms (which had been initially excited via electron collisions) can photo-emit electrons from the cathode, the gas isobutane was added. This gas can absorb photons over a wide range of energies (since excited isobutane molecules have many rotational and vibrational energy levels) and then deexcite through elastic collisions or dissociate into simpler molecules.

Because it is desirable for the field to be uniform in the drift space, so that the horizontal or vertical spatial position of the

particle varies linearly with time, the field shaping cathode wires are incorporated in the wire plane.

To discriminate on which side of the struck anode wire the particle passed, there was a 2.5 mm (half of anode wire spacing) offset between two adjacent wire planes.

The operating voltage was set at -1.52 kV. A list of the materials the secondary proton beam passed through as it travelled through the drift chamber is tabulated in [Table 7].

III.4 The Frozen Spin Target

The FST has been discussed in some detail in the previous chapter; only topics relevant to the analysis will be present below.

III.4.a Magnetic Holding Field

During the data collection period of the experiment, the target sample was maintained at a mixing chamber temperature of $45 (\pm 5)^{13}$ mK and in a holding field of 0.257 T. This ensured average polarization decay times (~650 hrs) that were in excess of the experimental data taking period (~21 hrs). The holding field direction throughout the experiment was vertical to the secondary beam central axis and pointed up. Various field maps were made of the vertical component of the target holding field as a function of distance from the center of the target during the "Test of Charge Symmetry Breaking" experiment, using properly calibrated Hall probes. These field maps, which were taken at a distance of 3.81, 2.54, 0, -2.54 and -4.57 cm above and below the target

¹³Considering only statistical fluctuations. If the carbon resistor calibration is taken into account as well, the uncertainty becomes ± 10 mK.

[Table 7]

Horizontal Drift Chamber Material in the Secondary Proton Beam Path

Material	Thickness (cm)	Description
Aluminized mylar	0.00025	Cathode foil
Isobutane/argon	0.64	Drift chamber gas
Aluminized mylar	0.00025	Cathode foil
Isobutane/argon	0.64	Drift chamber gas
Aluminized mylar	0.00025	Cathode foil
Isobutane/argon	0.64	Drift chamber gas
Aluminized mylar	0.00025	Cathode foil
Isobutane/argon	0.64	Drift chamber gas
Aluminized mylar	0.00025	Cathode foil

cell, were used to correct the incident, scattered and recoil proton trajectories for the deflection that they had undergone in the presence of the holding field. The holding field deflection angles for the above field maps are tabulated in [Table 8]. How these deflection angles were calculated will be discussed in the following chapter. A sample plot of the vertical component of the holding field as a function of radial distance from the FST in the horizontal beam plane is illustrated in [Fig. 22].

III.4.b Target Support Structure

To minimize background and multiple scattering, the insulation and support structure material used in the construction of the FST was kept to a minimum. Two 50 cm³ vacuum spaces [Fig. 7] above and below the target cell were also incorporated to keep as much unwanted material out of the $A_{yy}(\theta)$ experiment neutron beam as possible, to reduce background in that experiment. A list of the FST material around the target cell is tabulated in [Table 9].

X-ray radiographs were taken of the FST target cell before the data collection period of the experiment. The results of these radiographs are tabulated in [Table 10].

III.5 Scattered and Recoil Proton Detection Systems

III.5.a Introduction

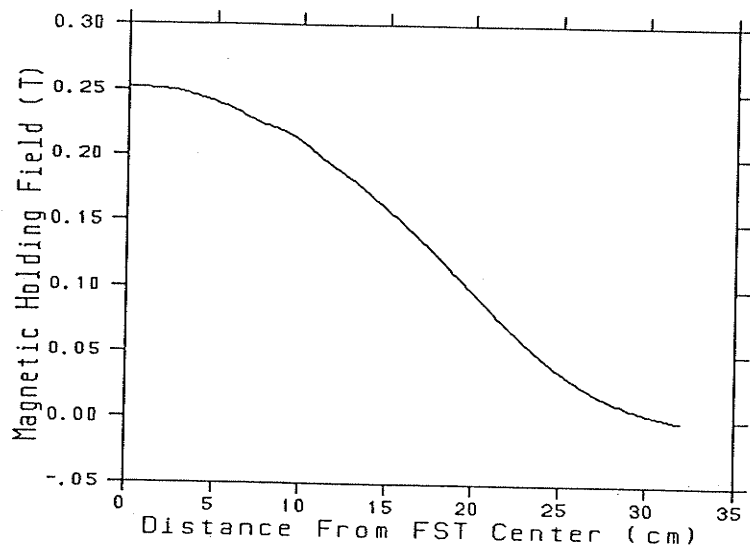
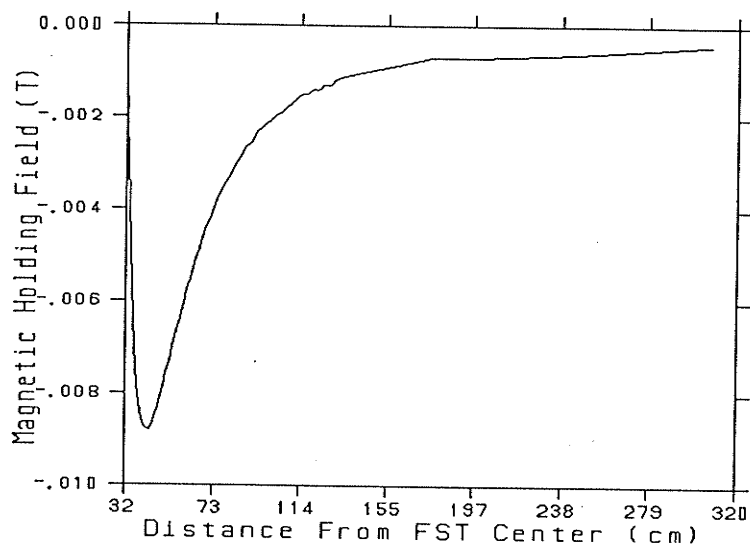
To determine the target polarization from the experimental data two criteria had to be met. First, the secondary beam protons had to be of a specific energy or momentum and second, the protons had to scatter elastically from the FST protons. A p-p scattering event is elastic

[Table 8]

Frozen Spin Target Holding Field Deflection Angles

Vertical Position (cm)	Secondary Beam Production Target	Horizontal Deflection Angle ¹⁴ (in degrees)
3.81	LH2	0.694
	C	0.667
2.54	LH2	0.680
	C	0.654
0.00	LH2	0.666
	C	0.640
-2.54	LH2	0.675
	C	0.649
-4.57	LH2	0.705
	C	0.678

¹⁴The above deflection angles were calculated using the secondary proton beam energy at the FST center. This corresponded to 469(501) MeV when using LH2 (C) as a secondary beam production target.

(a) Holding field with positive $\int B \cdot dl$.(b) Holding field with negative $\int B \cdot dl$.

[Fig. 22]

Holding field as a function of radial distance from the FST in the horizontal beam plane. To illustrate the holding fields zero crossing characteristic, the field map was plotted in two sections. It should be noted that figure 'a' and 'b' have been plotted using different coordinate scales.

[Table 9]

Frozen Spin Target Material in the Secondary Proton Beam Path

Material ¹⁵	Thickness (cm)	Description
1-butanol	1.9 ¹⁶	Target material (60% packing fraction)
Liquid helium	1.9 ¹⁶	Refrigerant fluid (40% packing fraction)
Copper	0.0054	Target cell thickness
Liquid helium	0.2790 ¹⁶	Refrigerant fluid
Stainless steel	0.0127	Inner vacuum vessel
Copper	0.0076	Inner heat shield
Mylar	0.0006	Insulation
Copper	0.0076	Middle heat shield
Mylar	0.0032	Insulation
Copper	0.0076	Outer heat shield
Mylar	0.0095	Insulation
Aluminum	0.1016	Outer vacuum vessel

¹⁵All of the materials are arranged in a concentric geometry around the FST.

¹⁶Because the target cell is rectangular and the inner vessel is circular, the above thickness will change depending on the path taken by the scattered or recoil proton.

[Table 10]

X-ray Radiograph Results of Frozen Spin Target

Description	Offset	
	Longitudinal ¹⁷ (mm)	Horizontal ¹⁸ (mm)
Cryostat location with respect to solenoid inner wall	-0.7 ± 0.2	-0.9 ± 0.2
Cryostat location with respect to pivot post	-1.0 ± 0.2	0.0 ± 0.2
Target cell location with respect to cryostat outer wall	0.5 ± 0.2	-1.0 ± 0.2
Target cell location with respect to pivot post	-0.5 ± 0.3	-1.0 ± 0.3

¹⁷The longitudinal axis is along the central beam axis and positive downstream the FST.

¹⁸The horizontal axis is horizontal to the central beam axis and is positive to the left of an observer looking downstream from the FST.

when kinetic energy is conserved in the p-p interaction.

In the experiment, the p-p elastic scattering events were detected in coincidence in two independent scattered and recoil proton detector systems. Two symmetric detector systems were set up left and right of the beam central axis [Fig. 23]. This aided in the first order cancellations of systematic errors arising from differences in detector efficiency, scattering angles and solid angles. The four detectors provided information from which kinetic energy, momentum, scattering angle and azimuthal angles were determined, which was sufficient information to identify p-p elastic scattering events from the following kinematic constraints:

- (a) energy sum;
- (b) transverse momentum sum;
- (c) opening angle and
- (d) coplanarity angle.

All of the above four constraints will be described in some detail in the following chapter.

For future reference, the experimental coordinate system is defined here as: a left event has the scattered proton to the right of the incident beam central axis (looking downstream of the FST) and the recoil proton to the left, a right event has the mirror symmetric definition [Fig. 23]. The z-axis is defined as positive, downstream of the FST, along the secondary beam central axis. The x-axis intersects the target in the horizontal plane and is defined positive on the left hand side of an observer looking downstream from the FST. The y-axis is vertical to the x-z plane and is defined positive above the plane. The

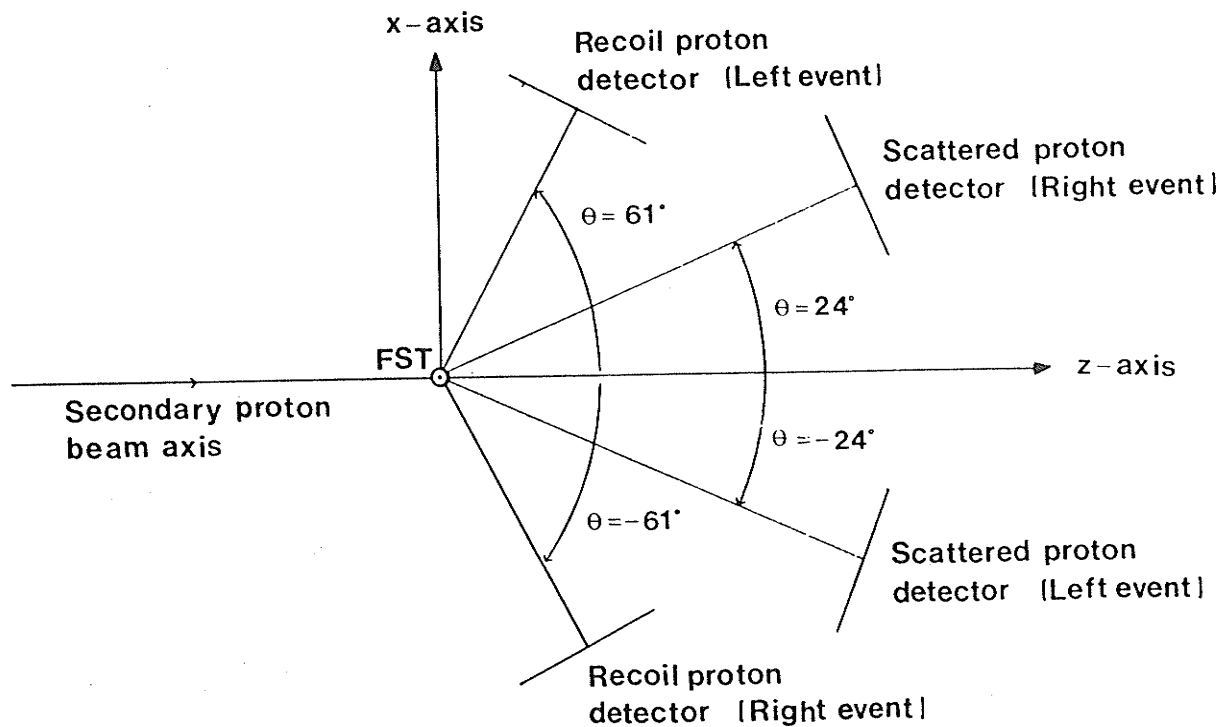


[Fig. 23]

Experimental coordinate system definitions as viewed from above. Note that positive y-axis comes out of the diagram.

physical detector angles are defined positive when the proton scatters to the left of the positive z-axis.

The two recoil and scattered proton detectors were placed at $\pm 61^\circ$ (lab)¹⁹ and $\pm 24^\circ$ (lab)¹⁹, respectively. At these angles the p-p analyzing power is accurately known to $\pm 1.5\%$ [Ref. 3].

III.5.b Scattered Proton Detection Apparatus

The scattered proton detection system consisted of a TOF system that was used to determine the scattered proton energy or momentum, and four delay-line chambers (DLC) which were placed between the two TOF scintillators to record horizontal and vertical coordinates for track reconstruction. The apparatus mentioned above was mounted on a rigid boom that was pivoted just below the FST center. This enabled the entire detection system to be rotated to whatever angle was required without having to re-align the detector components. The detector arrays were also used by the $A_{yy}(\theta)$ experiment. Details of the apparatus along the detector boom are listed in [Table 11].

III.5.b.1 Time of Flight

The TOF start scintillator, with specifications listed in [Table 12] has two photomultiplier tubes attached to the scintillator; one located at the top and one at the bottom. Each photomultiplier tube was attached to the TOF scintillator via light guides that contained six optical strips of equal length. The TOF stop scintillator consisted of

¹⁹These are the nominal scattering angles. During the experiment the scattered (recoil) proton detector systems were placed on the floor at angles adjusted for the holding field deflections [see tables 11 and 15].

[Table 11]

Positions of Scattered Proton Detection Apparatus Along Boom

Item	Distance ²⁰	
	Left Event (mm)	Right Event (mm)
TOF start scintillator	410.0	410.0
DLC 1	616.3	607.3
DLC 2	1669.3	1671.3
DLC 3	2831.5	2828.1
DLC 4	2999.5	2992.7
ΔE scintillator	3139.0	3137.0
TOF stop scintillator	3444.0	3444.0
Physical detector angle ²¹		
For LH2 target run	-25.28°	22.62°
For C target run	-25.35°	22.60°

²⁰All distances are given as the distance from the center of the FST to the center plane of the listed item and were measured to within ± 1.0 mm.

²¹The booms were aligned to these angles to take into account the holding field deflections of the scattered protons. The angles were measured to within $\pm 0.05^\circ$ (absolute scale).

[Table 12]

Scattered Proton Detection System TOF Start Scintillator Dimensions

Material	Pilot-u scintillator
Width	17.5 cm
Height	17.5 cm
Thickness	0.08 cm
Light guide strip length	17 cm
Light guide rod: Length	5 cm
Inner four strip width	3 cm
Outer two strip width	2.75 cm
Overall length ²²	131 cm
Photomultiplier tube shielding length	35 cm

²²Includes both photomultiplier tubes and light guides.

one large scintillator sheet of dimensions 67.0 cm wide by 69.0 cm high and thickness 6.4 mm. The TOF stop scintillator was viewed by four photomultiplier tubes: two located at the top and two at the base. In each case, signals from the photomultiplier tubes were fed into a TDC via a CFD. The associated scintillator TDC's were averaged and the TOF determined from the difference between averaged TOF start and stop TDC signals. Because of the TOF stop scintillators large dimensions, the timing signals had a position dependent correction [see section IV.2.b.2].

A simplified schematic diagram of the scattered proton detector system electronics is illustrated in [Fig. 24]. The ΔE scintillator had dimensions of 67.0 cm wide by 65.0 cm high and a thickness of 6.4 mm.

III.5.b.2 Track Reconstruction

The scattered proton track was reconstructed from hit coordinates in four DLC's each capable of recording vertical and horizontal coordinates. The DLC's, which are multiwire proportional chambers (MWPC) [Ref. 31], were chosen for their high detection efficiency (> 90%) of ionizing particles.

The reconstruction of the scattered proton track had a two-fold importance:

- (a) the proton scattering angle could be determined; and
- (b) the proton kinetic energy or momentum could be determined from the TOF, since the reconstructed proton track could be used to determine the proton path.

The first of the four DLC's in each scattered proton detection system had an active area of 30 cm by 30 cm, whereas the remaining three had an active area of 58.0 cm by 58.0 cm. It was not necessary

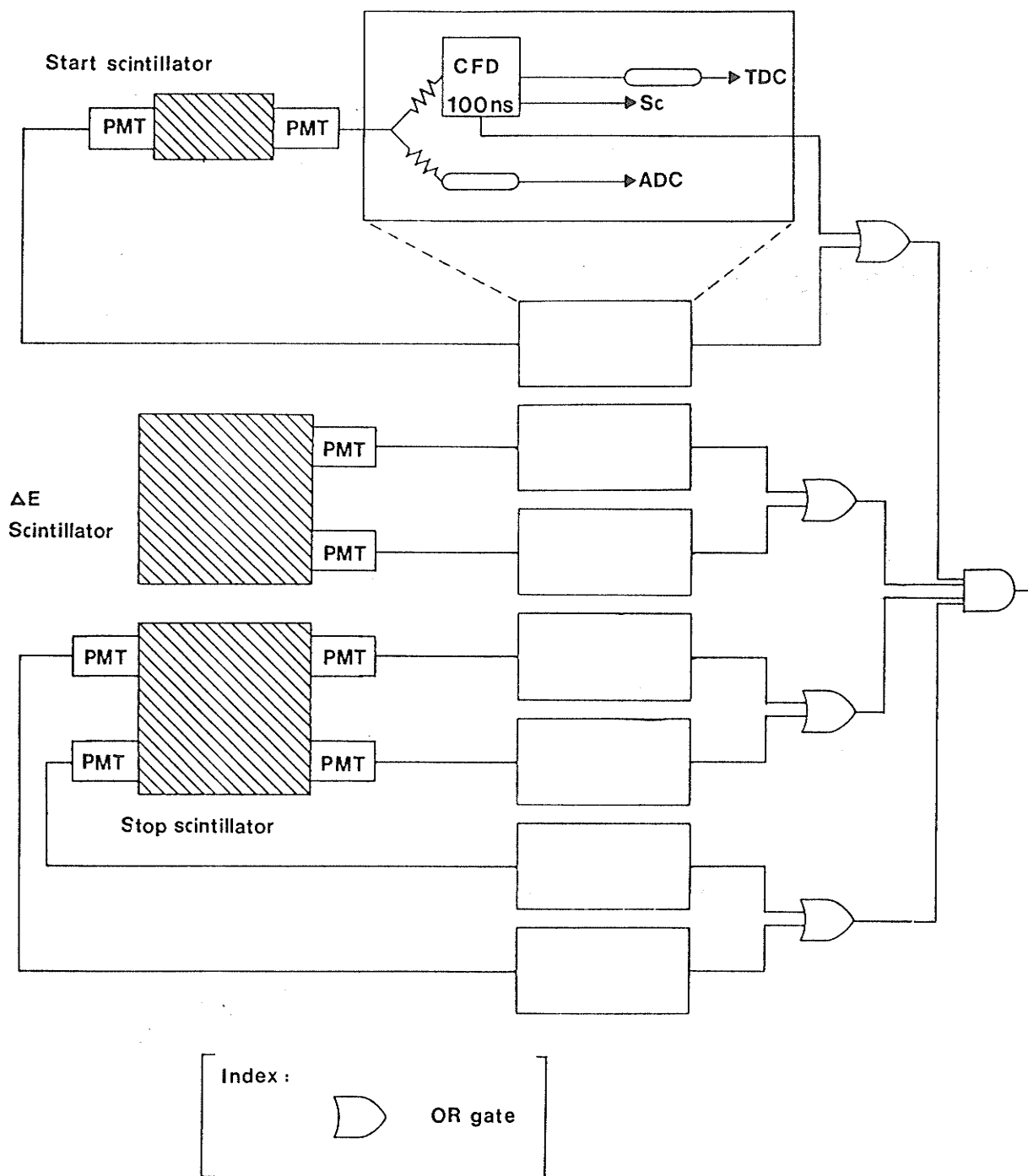


[Fig. 24]

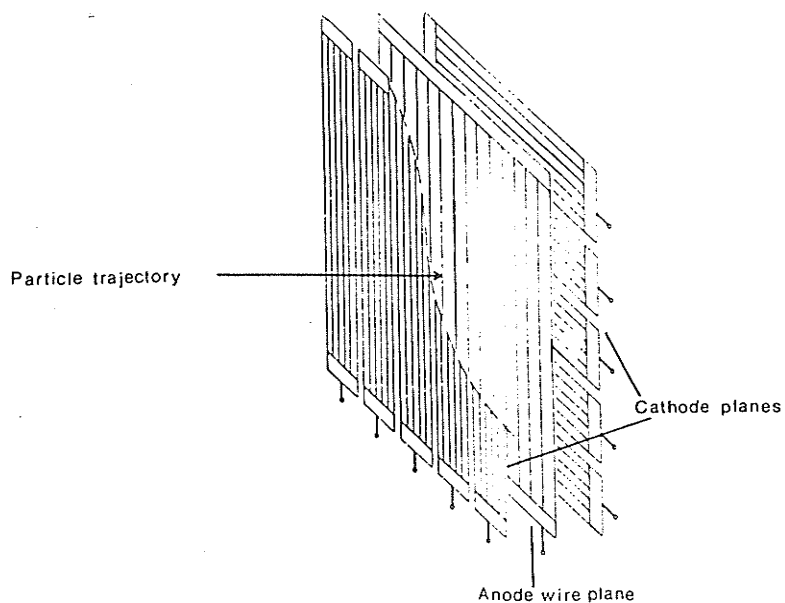
Scattered proton detector electronics.

for the first DLC to have a large active area since the solid angle projected to an area at the first DLC well within the 30 cm by 30 cm active region.

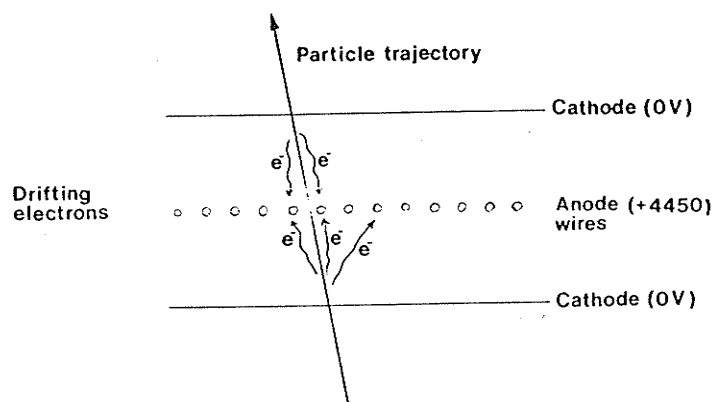
The following discussion will apply to the 58.0 cm by 58.0 cm DLC's but a similar description can be used for the 30 cm by 30 cm DLC's. Each DLC [Fig. 25a] consisted of two cathode planes and one anode wire plane that was sandwiched in between. The cathode planes consisted of copper-mylar laminate strips that had a separation of 0.5 mm. The copper strips were 3.5 mm wide and 20 μ m thick. The anode wire plane contained 291 vertically running wires that had a separation of 2 mm and were at a + 4550 V potential (the first DLC operated at + 3600 V). The copper strips of the cathode planes ran horizontally in one plane and vertically in the other, each ran perpendicular to their respective delay line, to which each cathode plane was capacitatively coupled.

A delay line is a transmission line that allows the spatial position of a particle to be determined from the difference in arrival times of the signals at the two ends of the line [Fig. 26]. The two delay lines on each chamber were mounted on the vertical and horizontal frames of the chamber and had a propagation of approximately 28 ns/cm.

The space between the cathode planes contained "magic" gas whose composition was 30% isobutane, 30% a mixture of 1% freon in argon and 40% argon bubbled through methylal. The gas flow rate was 65 cm³/min (the first DLC had a gas rate of 90 cm³/min). This was sufficient to counter-balance the electrostatic attraction between the anode and cathode planes. The separation distance between cathode planes was maintained at 6 mm.



(a) Schematic of delay-line chamber section.



(b) Principle of operation of a delay-line chamber.

[Fig. 25]

The delay-line chamber.
Diagrams are not to scale.

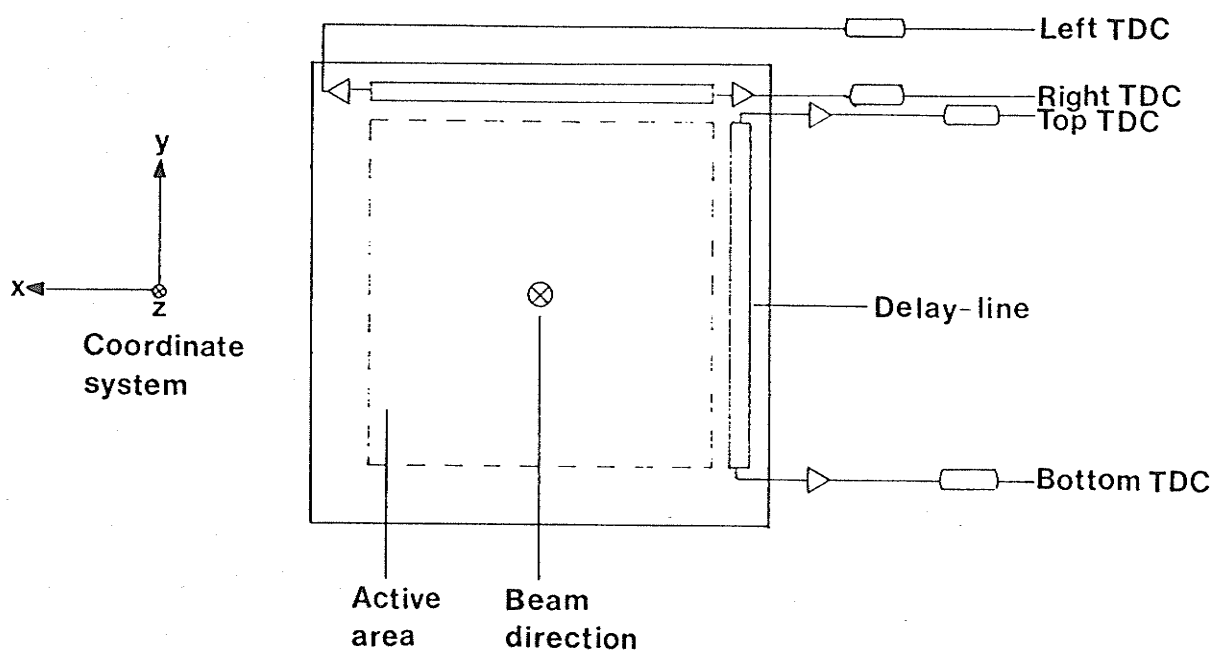


[Fig. 26]

Delay line chamber electronics. At each end of the delay line an amplifier-discriminator circuit is attached.

As the charged particle traveled through the DLC [Fig. 25b] a track of ionization was left in the gas. The resulting electrons are then collected at the anode wires, disturbing the potential temporarily. An image of the disturbance appears on the cathode plane strips and gives an electrical signal that travels along the delay-line, indicating that the particle has passed. Each anode wire in the DLC then operated as an individual proportional counter. As the electrons moved towards the anode wire under the influence of the large electric field their acceleration was large enough to cause secondary ionization near the wire, yet small enough so that the output anode wire signal was still proportional to the number of primary ion pairs.

As for the drift chamber, the main gas components of the MWPC are argon and isobutane. Because the dissociated products of the isobutane can recombine to form solid or liquid residues (i.e. polymerizes) that can build up on the cathode planes and cause serious distortions of the electric field in the chamber, the gas methylal (which is non-polymerizing) was added. Ionized methylal molecules, which have an ionization potential lower than that of the other gas components, were formed through ion exchange and were what eventually reached the cathode plane. Freon, which is a molecule with a large electron affinity, was also added to capture secondary electrons (i.e. preventing avalanching).

When a scattered proton travels through the DLC the ionization electrons collect at the anode wires from either side of the wires, this implies that the coordinate with cathode strips parallel to the

anode wires will have a resolution²³ of just the anode wire spacing ± 1 mm. The coordinate with cathode strips perpendicular to the anode wires will have a resolution²³ of ± 0.7 mm. A list of the DLC cathode strip geometry with respect to the anode wire direction is tabulated in [Table 13].

The DLC coordinate non-linearities were corrected from calibration tables that relate time delay to absolute coordinate position. These tables were constructed prior to the "Test of Charge Symmetry Breaking" [Ref. 33, 34] experiment and were obtained in the following fashion. The calibration of the coordinate with cathode strip parallel to the anode wire, referred to in this discussion as the horizontal coordinate, can be made by histogramming the time difference spectra of the horizontal delay line TDC's. Individual anode wires can be distinguished as sharp peaks, thus the characteristic "picket fence" signature. A calibration table can then be constructed from the number of peaks in the histogram and known peak (anode wire) separation. The vertical coordinate calibration is somewhat more complicated since no "picket fence" spectrum exists. This arises from the fact that the anode wires run vertically, the horizontal spectra are then discrete whereas the vertical spectra are continuous. The vertical coordinates of each DLC were calibrated by using the following scheme: the second and fourth DLC were rotated by 90° so that their vertically running anode wires were now running horizontally. This allowed the vertical (horizontal) coordinates in the first (second) and third (fourth) DLC to

²³How the DLC resolution was determined will be discussed in the following chapter.

[Table 13]

DLC Cathode Strip Geometry with Respect to Anode Wire Direction

DLC Identification	x coordinate ²⁴	y coordinate ²⁴
Left event:		
DLC 1	perpendicular	parallel
DLC 2	parallel	perpendicular
DLC 3	parallel	perpendicular
DLC 4	parallel	perpendicular
DLC ²⁵	parallel	perpendicular
Right event:		
DLC 1	perpendicular	parallel
DLC 2	parallel	perpendicular
DLC 3	parallel	perpendicular
DLC 4	parallel	perpendicular
DLC ²⁵	parallel	perpendicular

²⁴Coordinates are defined similarly to the experimental coordinate system with exception that it is with respect to an observer facing the DLC's positioned at the FST center.

²⁵These are the DLC's used in the recoil proton detector systems.

be calibrated by using the already calibrated "picket fence" spectra of the neighboring DLC's. The ray tracing between each pair of "picket fence" coordinate DLC's then allowed the non-linearities of the delay-lines in the "non-picket fence" coordinates to be mapped. This showed the deviations from linearity are on the order of ± 1 mm over the length of the delay lines [Ref. 34]. The individual TDC modules were calibrated electronically prior to the "Test of Charge Symmetry Breaking" [Ref. 33, 34] experiment.

In each DLC four BNC inputs were provided for pulser injection near each end of each delay line, with a separation of $552.5 (\pm 0.7)$ mm. These inputs were coupled directly to 1.6 mm wide copper strips which were in turn coupled capacitively to the cathode plane. These pulser fiducials were crucial for providing a check on the coordinate calibration. The materials which the scattered proton had to pass through as it travelled through the DLC are listed in [Table 14].

III.5.c Recoil Proton Detection Apparatus

The recoil proton detection system consisted of a TOF stop scintillator used to determine the recoil proton momentum or energy, a single DLC placed just in front of the TOF stop scintillator to provide coordinates for track reconstruction and a veto scintillator located near the FST to veto recoil charged particles that had scattered from the cryostat shell. The DLC and stop scintillator were mounted just in front of the $A_{yy}(\theta)$ experiment's neutron detection array [Ref. 33] which consisted of two stacks (second stack placed behind first) of seven scintillator bars each having dimensions 150 mm thick by 150 mm high by 1050 mm long. The neutron detection array was on a movable frame that allowed the

[Table 14]

Delay Line Chamber Material in the Scattered Proton Path

Material	Thickness
Aluminized mylar	25 μm
Magic gas ²⁶	14-20 mm
Mylar	25 μm
Copper cathode strip	20 μm
Magic gas	6 mm
Tungsten anode wire	20 μm
Magic gas	6 mm
Copper cathode strip	20 μm
Mylar	25 μm
Magic gas	14-20 mm
Aluminized mylar	25 μm

²⁶The thickness of the magic gas is listed as 14-20 mm because of the bulging of the outer foils of the DLC's.

detector to be positioned at any radial distance and angle (with respect to scattered proton detector pivot) without the need to re-align the individual detector components. During the $A_{yy}(\theta)$ experiment the DLC was moved aside via a linear bearing roller system. Details of the recoil proton detector apparatus with components relevant to the p-p elastic scattering experiment are tabulated in [Table 15].

III.5.c.1 Time of Flight

The TOF system used the scattered proton TOF start scintillator as the time reference. The TOF stop scintillator, also used in the $A_{yy}(\theta)$ experiment as a charged particle veto scintillator, consisted of three vertically running scintillator sheets that gave an overall dimension of 1086 mm wide by 1050 mm high. Each scintillator sheet had a thickness of 6.4 mm and width of 368 mm. The central sheet overlapped the two outer sheets by 9 mm on each side. In the p-p elastic scattering experiment only the central sheet was included in the recoil proton electronic trigger, that is, only the central sheet functioned as a TOF stop scintillator. Each scintillator sheet was viewed by two photomultiplier tubes; one located at the top and one at the bottom. In each case, signals were fed into a TDC via a CFD. The TDC signals from above and below each scintillator sheet were averaged and the TOF was determined from the difference between the average start and stop TDC signals with the appropriate timing considerations, which arose from the fact that the start signals did not originate at the FST center and the scattered proton electronic trigger (to be discussed in next section) was also involved. A simplified schematic diagram of the recoil proton detector system electronics for the components relevant to the p-p elastic scattering experiment is illustrated in [Fig. 27].

[Table 15]

Positions of Recoil Proton Detection Apparatus

Item	Distance ²⁷			
	Left Event		Right Event	
	LH ₂ runs	C runs	LH ₂ runs	C runs
	(mm)		(mm)	
Veto scintillator	410.0	410.0	410.0	410.0
DLC	2394.6	2409.1	2408.4	2397.4
TOF stop scintillator	2719.0	2733.5	2730.0	2719.0
Physical detector angle ²⁸	59.5°	59.5°	-62.5°	-62.5°

²⁷All distances are given as the distance from the center of the FST to the center of the listed item and were measured to within ± 1.0 mm.

²⁸The "neutron array" was aligned to these angles to take into account the holding field deflections of the recoil protons. The angles were measured to within $\pm 0.05^\circ$ (absolute scale).

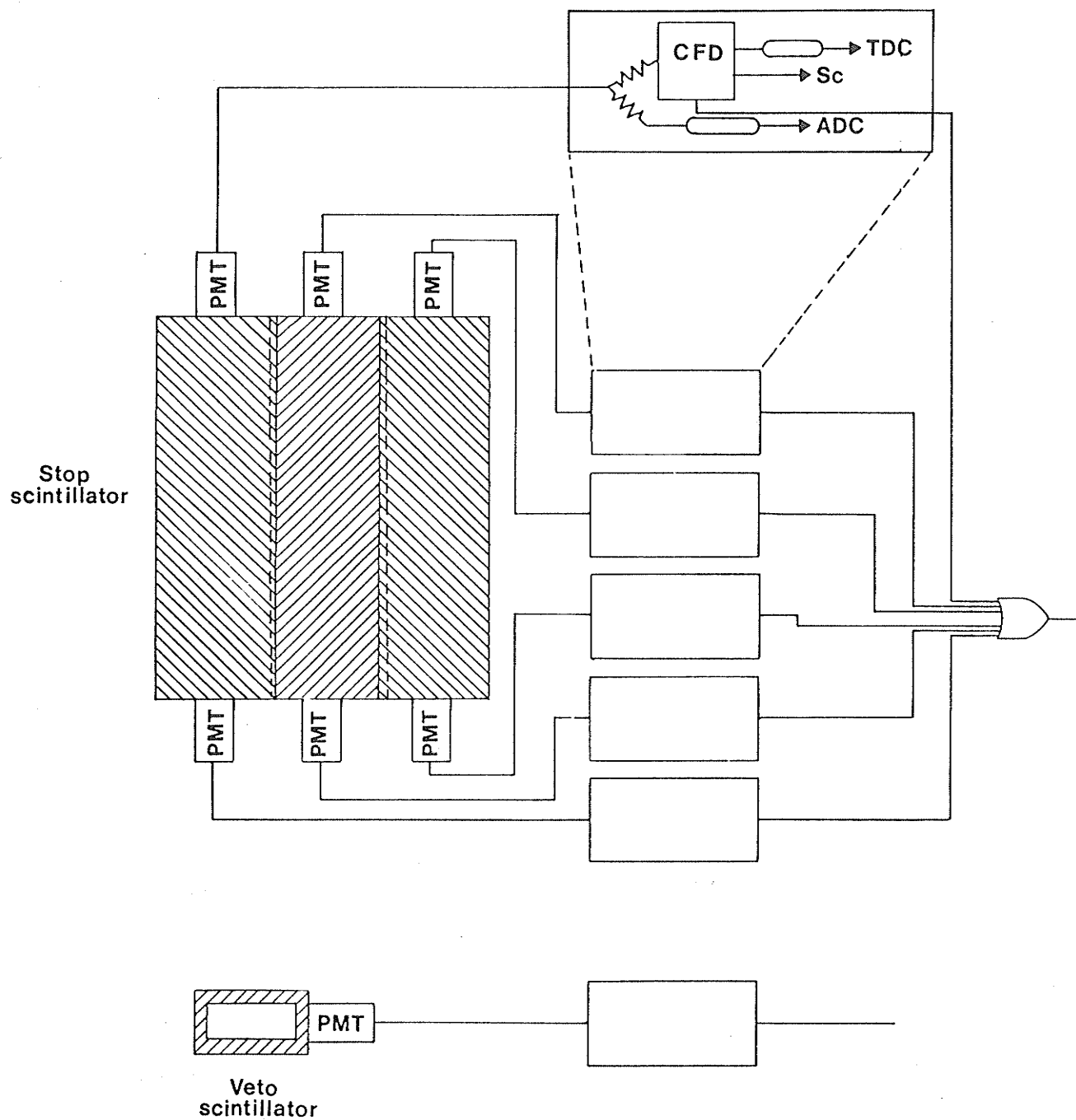


[Fig. 27]

Recoil proton detector electronics.

III.5.c.2 Track Reconstruction

The recoil proton track was constructed using the following scheme: the origin of the track was the point where the ray traced scattered proton track intersected the x equal to zero plane at the FST. The DLC that was mounted on the recoil proton detector supplied the second coordinates. The two overlapping regions (each 9 mm wide) on the TOF stop scintillator and the known widths of the neutron detector scintillator bars provided sufficient information to align the DLC on the recoil proton detector (using software).

III.5.c.3 Veto Scintillator

To eliminate protons that had undergone scattering from the FST cryostat shell, a veto scintillator (with a rectangular hole) was placed between the FST and recoil proton detector. The veto scintillator was set 410 mm from the FST center and was included in the recoil proton electronic trigger. The specifications of the veto scintillator are tabulated in [Table 16].

III.6 Trigger Logic

A simplified diagram of the electronic trigger system used in the experiment is illustrated in [Fig. 28]. The scattered proton latch (SPL) is triggered when the scattered proton TOF start (b), ΔE scintillator (c) and TOF stop scintillator (d) all fire, thus signifying that a particle has been detected by the scattered proton detector system. The SPL then commences to start the TDCs and ADC gate strobing. If the coincident recoil proton detector electronics (SPL reset inhibit in diagram) does not inhibit the SPL reset, the SPL

[Table 16]

Recoil Proton Veto Scintillator Dimensions

Material	Pilot-u scintillator
Scintillator thickness	0.32 cm
Overall width (scintillator)	16 cm
Hole width	10 cm
Overall height (scintillator)	25 cm
Hole height	18 cm
Light guide strip length	25 cm
Number of strips	6
Light guide rod: Length	10 cm
Inner four strip width	3 cm
Outer two strip width	2 cm
Overall length ²⁹	91 cm

²⁹Includes both photomultiplier tubes and light guides.

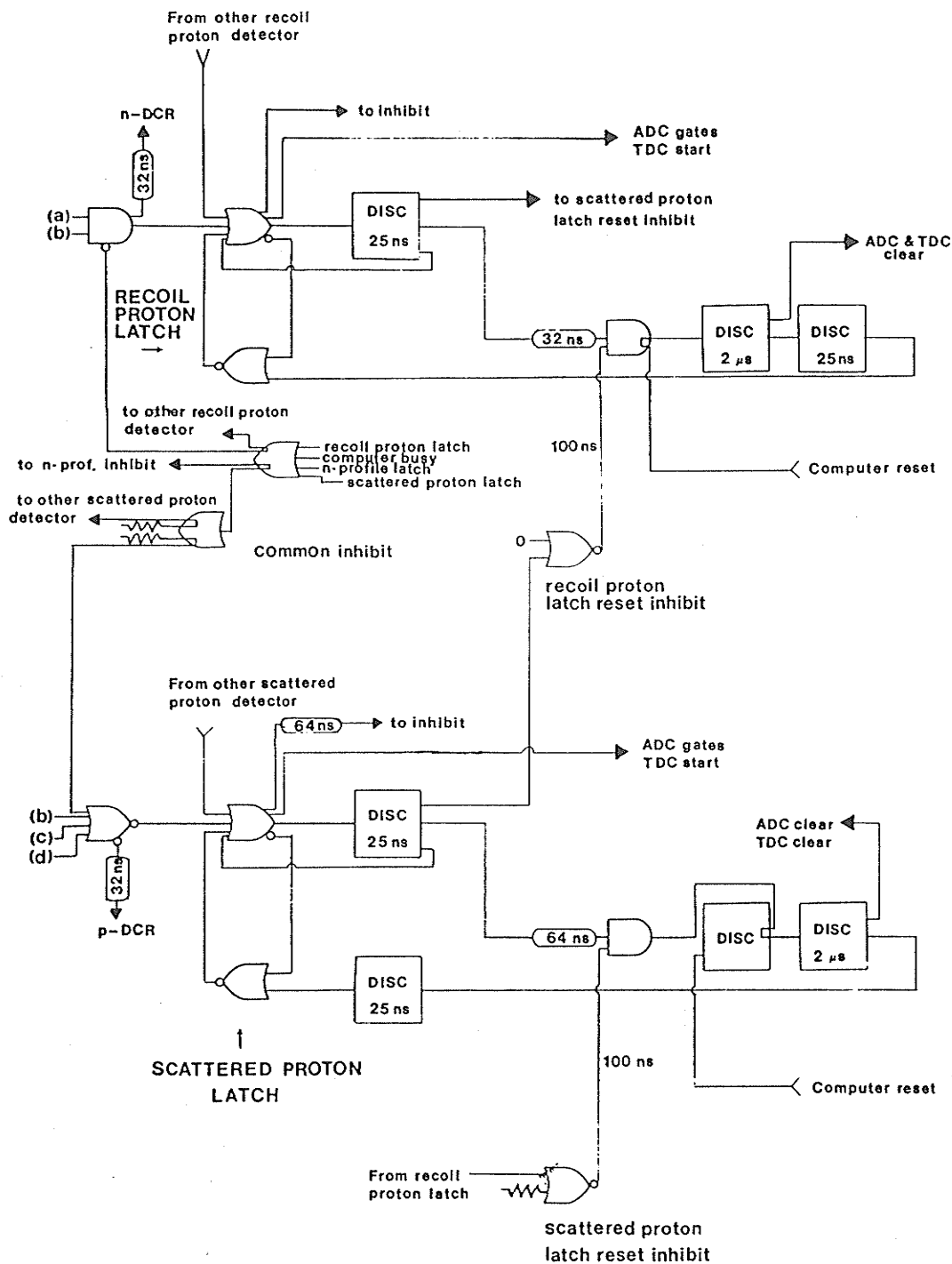


[Fig. 28]

Schematic of p-p elastic scattering experiment's trigger logic.

releases itself, the ADC and TDCs are cleared and it returns to its waiting state. If on the other hand the SPL reset is inhibited, which requires a signal from the recoil proton latch (RPL) to arrive within 100 ns of the SPL, the event is processed by the computer as the electronics waits (common inhibit in diagram), the computer reset is triggered, both ADC's and TDC's are cleared and the latch returns to its waiting state after being cleared by the computer. The RPL is triggered when both the scattered proton TOF start scintillator (b) and recoil proton TOF stop scintillator (central sheet) (a) fire, provided there is no recoil proton veto scintillator signal.

III.7 Data Collection and On-line Monitoring

Whenever a latch was set, the signals from the detector component electronics were interfaced to a Data General ECLIPSE computer system via three CAMAC crates. The computer then, by using the DACS data acquisition program, stored the data on tape at 1600 b.p.i. and provided the on-line monitoring of the data.

The information from the CAMAC crates was divided into eight event types, with each event type occupying a single tape block that had a maximum length of 1024 16-bit words. A summary of the eight event types is made in [Table 17]. For type 2 events, that is p-p coincident events observed by both recoil and scattered proton detectors, the identification of the left (right) events was made by setting the least significant (next higher) bit within a digital coincidence register (DCR) unit. The DCR bit map is tabulated in [Table 18].

The time it took to collect the 100,000 events on tape varied from one to two hours depending on the primary beam current. Every tape

[Table 17]

Event Type Summary

Event Type	Description ³⁰
1	Contained information for scalers 1-60. The data was read as clock events every 5 seconds.
2	Contained all the DCR bit, ADC, TDC and wire chamber information for a given p-p coincident event.
3	This event type was used in the $A_{yy}(\theta)$ experiment for the neutron beam profile monitor and polarimeter events.
4	Contained information concerning all the LeCroy mainframe high voltage settings. These events were read as clock events every 10 minutes.
5	Contained information for scalers 61-136 and were treated in the same way as type 1 events.
6	Spare - was not assigned.
7	This event type contained information concerning the operation of the FST. These events were read every 5 minutes as clock events.
8	Spare - was not assigned.
9	This event type was used in the $A_{yy}(\theta)$ experiment for the button events, which were used to calibrate the neutron bars.

³⁰The above event type summary was used by both $A_{yy}(\theta)$ and calibration experiments.

[Table 18]

DCR Bit Map Summary

Bit Number	Description ³¹
0	Left event
1	Right event
2	Left button event
3	Right button event
4	Pulser event (software set)
5	DLC trip
6	Polisis spin Up and not Busy
7	Polisis spin Down and not Busy
8	Polisis spin Off and not Busy
9	RF signal present
10	Polisis Busy
11	Pulser
12	Enable neutron profile monitor (switch 1)
13	Enable neutron polarimeter (switch 2)
14	p single mode (switch 3)
15	n single mode (switch 4)

³¹The above bit map is for the lower order bits of the DCR and was used by both $A_{yy}(\theta)$ and calibration experiments.

was identified by the assignment of a run number. A list of the various runs, with information pertinent to the data analysis, is tabulated in [Table 19] and [Table 20].

During the course of each run the following on-line monitoring was performed:

- (a) the output signals of the various ADC and TDC modules were monitored by plotting a two dimensional spectrum with the channel number on the x-axis and the word number (module identification within a tape block) on the y-axis;
- (b) the high voltage settings in all the LeCroy mainframes were checked at the beginning of each run;
- (c) there was continuous checking of all scalers and their rates;
and
- (d) at the beginning of each run the FST x- and y-coordinate image (via track reconstruction of upstream horizontal drift chambers) was checked to ensure proper proton beam illumination on the FST.

During the collection and on-line monitoring of the data, there was no data rejection. This was left to the off-line data analysis that will be the main concern of the following chapter.

[Table 19]

Tape Summary of p-p Elastic Scattering Experiment
Using LH2 as a Secondary Beam Production Target

Run Number	"Clyde" DAC Setting	"Bonnie" DAC Setting	- PNMR
213	0.02	0.15	-0.790
214	0.02	0.07	-0.777
215	0.02	0.02	-0.766
216	0.02	0.02	unpolarized
217	0.02	0.07	unpolarized
218	0.02	0.15	unpolarized
219	0.02	0.07	unpolarized
220	0.02	0.07	unpolarized
222	0.04	0.07	0.799
223	0.04	0.02	0.798
224	0.03	0.15	0.797
225	0.03	0.07	0.796
226	0.03	0.07	0.794
227	0.03	0.02	-0.834
228	0.03	0.11	-0.830
229	0.03	0.11	-0.827
230	0.03	0.11	-0.824
231	0.03	0.11	-0.820

[Table 20]

Tape Summary of p-p Elastic Scattering Experiment
Using C as a Secondary Beam Production Target

Run Number	"Clyde" DAC Setting	"Bonnie" DAC Setting	\bar{P} NMR
271	0.03	0.05	0.821
272	0.03	0.00	0.820
273	0.03	0.05	0.819
274	0.03	0.10	0.818
275	0.03	0.10	0.817
276	0.03	0.10 ³²	0.815
277	0.03	0.10 ³²	0.814
278	0.03	0.10 ³²	0.813
279	0.03	0.10 ³²	0.812
280	0.03	0.10	-0.820
281	0.03	0.05	-0.819
282	0.03	0.00	-0.818
283	0.03	0.10 ³²	-0.817
284	0.03	0.10 ³²	-0.816
285	0.03	0.10 ³²	-0.815
286	0.03	0.10	-0.814
287	0.03	0.05	-0.812
288	0.03	0.01	-0.811
289	0.03	0.01 ³²	-0.810
290	0.03	0.05 ³²	-0.809
291	0.03	0.10 ³²	-0.807
292	0.03	0.10	-0.806

³²The polarity of "Bonnie" was interchanged.

CHAPTER IV

DATA ANALYSIS**IV.1 Introduction**

Because the goal of the p-p elastic scattering experiment was to calibrate the polarization measurement made by the NMR system, the p-p elastic scattering experiment will henceforth be referred to as the calibration experiment. The data that will be presented in this work are the results of the calibration experiment performed before and after the second $A_{yy}(\theta)$ data collection period (June 1987). The first calibration experiment was performed with a 469 MeV secondary proton beam produced at 9° (lab) to a primary beam of 497 MeV striking a liquid hydrogen (LH2) target. The second calibration experiment was performed at 501 MeV when a 512 MeV primary proton beam underwent 9° (lab) scattering from a graphite (C) target.

Even though both calibration experiments were performed at the TRIUMF facility, the entire data analysis was undertaken at the University of Manitoba. The analysis was performed on VAX-11/750 and MicroVAX II computer systems using the analysis program PERSEUS which was modified to suit the experiment. The analysis program was originally written to analyze the E121 "Test of Charge Symmetry Breaking" data.

IV.2 Analysis of p-p Scattering Events

As the protons in the secondary beam, henceforth referred to as the incident beam, impinge on the FST, they can undergo elastic or inelastic scattering or reactions. This section will concern itself with

presenting the various incident, scattered and recoil proton information that will be used to isolate elastic scattering events from inelastic ones and reactions.

IV.2.a. Incident Proton Analysis

IV.2.a.1 Time of Flight

During the first calibration experiment the time resolution of the incident proton time of flight (TOF) system, located upstream of the FST [Fig. 12] with TOF scintillator separation of 600.5 cm, was experimentally found to be ± 0.5 ns (one standard deviation of proton peak in TOF spectrum) which corresponded to a proton peak width of 62 MeV (two standard deviations of proton peak in energy spectrum).

Because the TOF system had an energy resolution of ± 31 MeV, the systematic error contribution to the FST polarization measurement, due to this error in the incident proton beam energy, would have been

$$\frac{\Delta P}{P} = \frac{\partial A_y(\theta)}{\partial E} \bigg|_{\substack{\theta = 24^\circ \\ E = 469 \text{ MeV}}} \cdot \left[\frac{\Delta E}{A_y(\theta)} \right] = 0.032 \quad (39)$$

where E and ΔE is the incident beam energy and its uncertainty (in MeV). The p-p analyzing power and its derivative was determined [Ref. 3] to be 0.4092 and $4.2 \times 10^{-4} \text{ MeV}^{-1}$ respectively. One can see then that the TOF system energy resolution is insufficient to achieve the desired $\pm 2\%$ absolute error accuracy in the FST polarization measurement. For this reason, the TOF system was used solely to introduce a cut on the momenta of the incident proton beam. The two horizontal drift chambers located

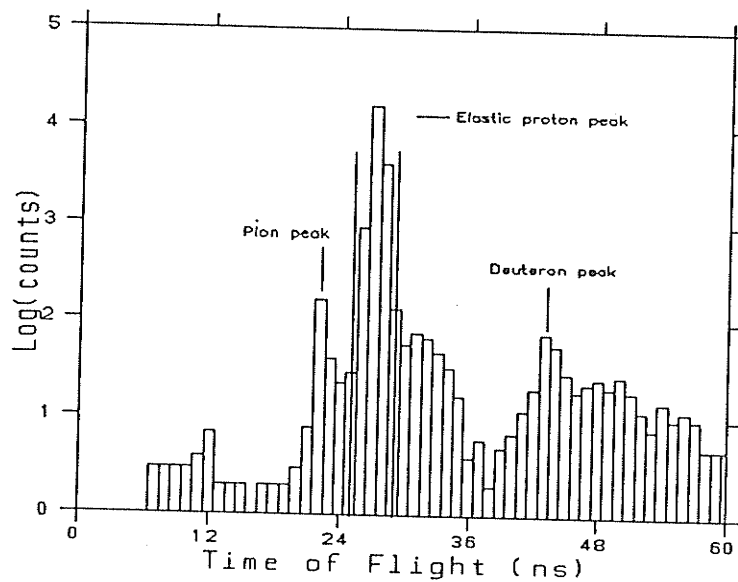
between the two TOF scintillators were not used to correct the incident proton path length, for the following two reasons:

- (a) the incident proton trajectories were not straight paths as a result of the various magnetic field deflections; and
- (b) the incident proton track reconstruction efficiency was low (this point is illustrated in section IV.2.a.4).

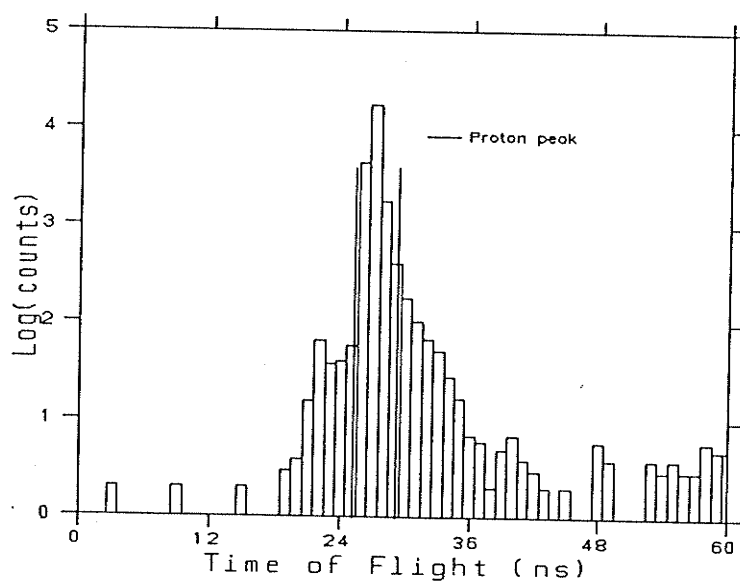
The incident proton TOF was calculated from

$$p\text{-TOF} = (\text{TDC}_{\text{stop}} - \text{TDC}_{\text{start}}) \cdot 0.05 + \text{offset} \quad (40)$$

where TDC_{stop} and $\text{TDC}_{\text{start}}$ are the TDC channel number positions of the stop and start TOF scintillators, the multiplicative factor 0.05 converts TDC channel numbers to nanoseconds and electronic delays were accounted for by the addition of an offset. The TOF spectra typically seen during the LH2 and C runs are illustrated in [Fig. 29]. The main peak in the LH2 TOF spectrum corresponded to the elastic proton peak and the two minor peaks corresponded to the deuteron and positive pion peaks from the proton reaction $pp \rightarrow d\pi^+$. The C TOF spectra consisted of a single peak that contained protons from both elastic and inelastic scattering that had taken place within the graphite target. The TOF systems timing resolution was not sufficient to separate the protons from the two scatterings. The vertical lines in the diagrams illustrate the software cut that was imposed to isolate the proton peak. On the average 74% of the FST p-p scattering events fell within the incident proton TOF software cut.



(a) For LH2 runs.



(b) For C runs.

[Fig. 29]

Incident beam TOF spectrum.

IV.2.a.2 Proton Beam Energy

The absolute primary proton beam energy was taken to be the cyclotron beam energy as determined from the stripper foil radius and was known to within ± 1 MeV. Because of the non-negligible uncertainty in the range-energy relations, the BEM system was used only to obtain an estimate on the variation of the primary proton beam energy with run number.

The proton beam energy at the center of the FST was deduced from the cyclotron primary proton beam energy after subtracting energy losses of the protons through the various materials traversed. The proton beam energy losses from cyclotron exit to FST center are tabulated in [Table 21]. The energy loss contributions were calculated by using the energy loss program LOSS, whose data are based on the Bethe-Bloch equation with corrections at low energy. Results from the program LOSS are good to better than 5% for protons in the 10-1000 MeV region, noting that density effects at high energies have been approximated. The proton beam energy at the center of the FST was 469 MeV when using LH2, and 501 MeV using C as a secondary beam production target.

The primary proton beam energy can be determined from the BEM system by knowing the number of protons that stop in each of the six scintillators, B_1 through B_6 [Fig. 14b]. If for example, N_i protons have stopped in the i th scintillator B_i , then the beam energy is calculated from

[Table 21]

Primary Proton Beam Energy Losses

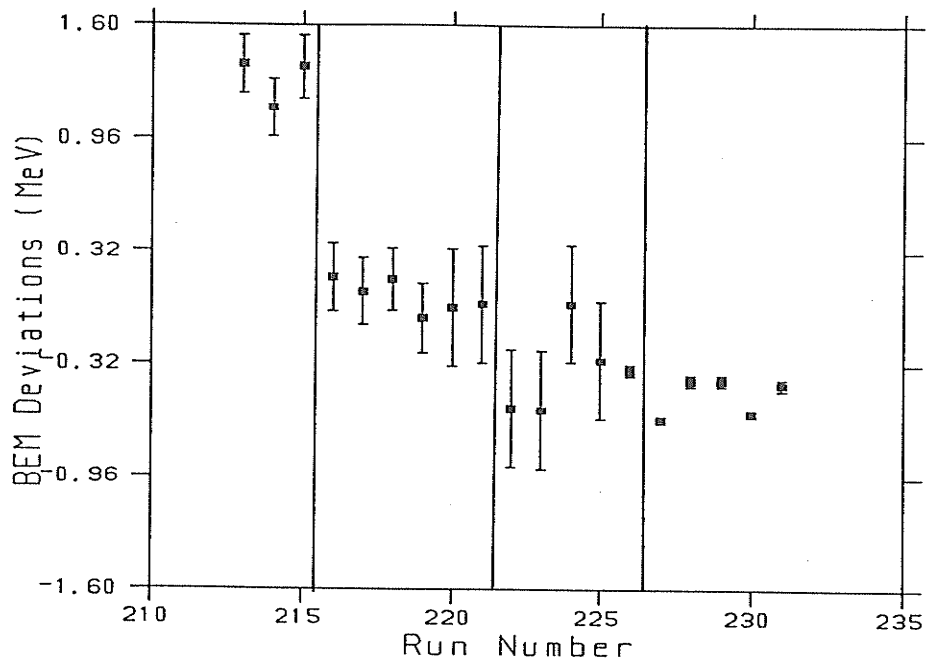
	LH2 run (MeV)	C run (MeV)
At cyclotron exit	497.0	512.0
At BEM kapton foil exit	497.0	512.0
At center of secondary beam production target	493.0	510.3
After 9° (lab) scattering at center of secondary beam production target	477.9	509.0
At secondary beam production target exit	476.8	507.3
After passing through 317.13 cm of air	475.8	506.3
At TOF start scintillator exit	475.6	506.1
After passing through 166.28 cm of air	475.1	505.6
At horizontal drift chamber exit	475.1	505.5
After passing through 124.22 cm of air	474.7	505.2
At horizontal drift chamber exit	474.6	505.2
After passing through 9.75 cm of air	474.6	505.1
At TOF stop scintillator exit	474.4	504.9
After passing through 21.55 cm of air	474.3	504.8
At FST center	469.0	501.2

$$\langle T \rangle_{\text{beam}} = \frac{\sum_{i=1}^5 a_i (N_i - N_{i+1})}{\sum_{i=1}^5 (N_i - N_{i+1})} \quad (41)$$

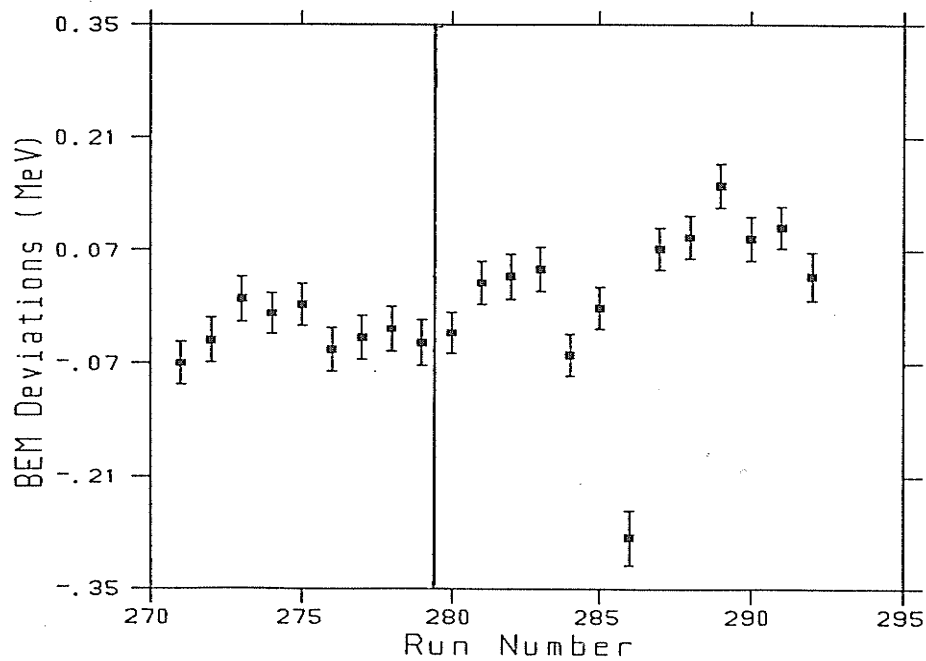
where a_i is determined from the range-energy tables and is the energy of the proton whose range extends up to the B_i scintillator or to the copper plate just after it. The number of protons that stop in the i th scintillator N_i , is determined from the trigger condition stated in [Section III.2.b].

The primary proton beam energy deduced in this manner was averaged over the measurements from the two symmetric (left, right) detector arms, of the BEM. [Fig. 30] illustrates the BEM deviations in the primary proton beam energy from the mean beam energy as a function of run number. The standard deviation for these primary proton beam energies was found to be ± 0.7 MeV and ± 0.1 MeV for the LH2 and C runs respectively (the LH2 beam energy deviations were somewhat higher due to electronic difficulties with the right BEM range counter assembly, the rectification of which is evident in [Fig. 30a] after run 225).

The uncertainty in the proton beam energy at the center of the FST was estimated to be ± 2 MeV and ± 1 MeV for the LH2 and C runs respectively. The incident beam energy uncertainty was estimated by adding in quadrature the beam energy uncertainty from the stripper foil radius position (± 1 MeV), the energy deviations from run to run as measured by the BEM system, and the 5% uncertainty in the total proton energy loss as a result of using the program LOSS. The differences in the estimated proton beam energy uncertainty for both calibration experiments was attributed to the 5% energy loss uncertainty



(a) For LH2 runs.



(b) For C runs.

[Fig. 30]

Primary proton beam energy deviation
as measured by the BEM system.

contribution. The systematic error contribution to the FST polarization measurement due to the incident beam energy uncertainty was calculated to be 0.2% and 0.1% (see Appendix C) for the LH2 and C runs respectively. The vertical lines in [Fig. 30], indicate periods during the calibration experiments which involved removing the stripper foil for access to change the FST polarization direction. The discontinuity in beam energy between runs 215 and 216 was a result of a beam tune.

IV.2.a.3 Magnetic Field Deflection Angle Corrections

Because the incident protons traversed the magnetic fields of the superconducting solenoid, steering magnet and FST holding field, their trajectories will be deflected in each of the above fields. Estimates of the individual magnetic field deflections were calculated and then used to correct the incident proton trajectories.

IV.2.a.3.i Magnetic Field Deflection Due to FST Holding Field

The angle by which the incident, scattered and recoil proton trajectories would be deflected due to the presence of the FST holding field alone was calculated from

$$\delta\theta_{\text{FST}} = \frac{\alpha}{p_{\text{in}}} \quad (42)$$

where p_{in} is the incident proton momentum (in $\text{MeV}\cdot\text{c}^{-1}$), and α is a constant that depends on the holding field's strength.

The coefficient α was determined in the following way. Proton paths leaving the FST center as a function of energy were computed as they passed through the scattered proton detector systems DLCs. A polynomial fit was then made to the paths and the paths were used to calculate each DLCs point of intersection. A straight line fit was then

made using the DLC intersection points which enabled the calculation of the proton deflection angle as it was observed by the scattered proton detector system (the linear fit was justified from the observations that the scattered proton deflections occur mostly in the first 10% or so of the path and the deviation from a straight line path was found to be very small, 0.7 mm for a 500 MeV proton). Knowing the proton deflection angle as a function of proton energy allowed the determination of the coefficient α to be made, by fitting the data to a $\frac{1}{p}$ dependence. The coefficient α took on the values in [Table 22] depending on the incident proton vertical target hit position (noting, that at the center of each of these regions, the field map of the FST holding field was known). The calculation of the coefficient α was made under the assumption that the holding field had only a vertical component (along the positive y-axis), thus, the proton deflections were always in the horizontal x-y plane.

The incident beam deflection angles tabulated in [Table 8] were calculated when using [Eq. 42], [Table 22] and the momentum values of 1049 MeV/c and 1091 MeV/c (which correspond to protons of energy 469 MeV and 501 MeV), when using the LH2 and C secondary beam production targets respectively. A typical deflection angle for the incident protons as they traversed the FST holding field during the LH2 (C) calibration experiment was in the order of 0.67° (0.64°).

IV.2.a.3.ii Magnetic Field Deflection Due to Superconducting Solenoid and Horizontal Steering Magnet

Because of superconducting solenoid focussing (focal length ~ 4 m) whose net effect was to reduce the dimensions of the secondary proton beam and the possibility that the solenoid could have been set with an offset

[Table 22]

FST Holding Field Deflection Coefficient

Vertical target hit position (mm)	Target geometry	α (deg·MeV/c)
50.8 to 31.8	Top	728
31.8 to 12.7		714
12.7 to -12.7	Middle	698
-12.7 to -31.8		708
-31.8 to -50.8	Bottom	740

along its y-axis, the dipole magnet "Clyde" was used to steer the incident proton beam onto the target. The horizontal deflection of the incident protons due to the superconducting solenoid and horizontal steering magnets' fields was calculated from

$$\delta\theta_{\text{Hori}} = \frac{S \cdot \delta\theta_{\text{Clyde}}}{S + T} \quad (43)$$

where T is the distance between the horizontal steering magnet center and the FST center, S is the distance between the solenoid center and the steering magnet, and $\delta\theta_{\text{Clyde}}$ is the deflection angle the protons would have undergone due to the horizontal steering magnets field alone, as in [Fig. 31a]. $\delta\theta_{\text{Clyde}}$ was calculated from

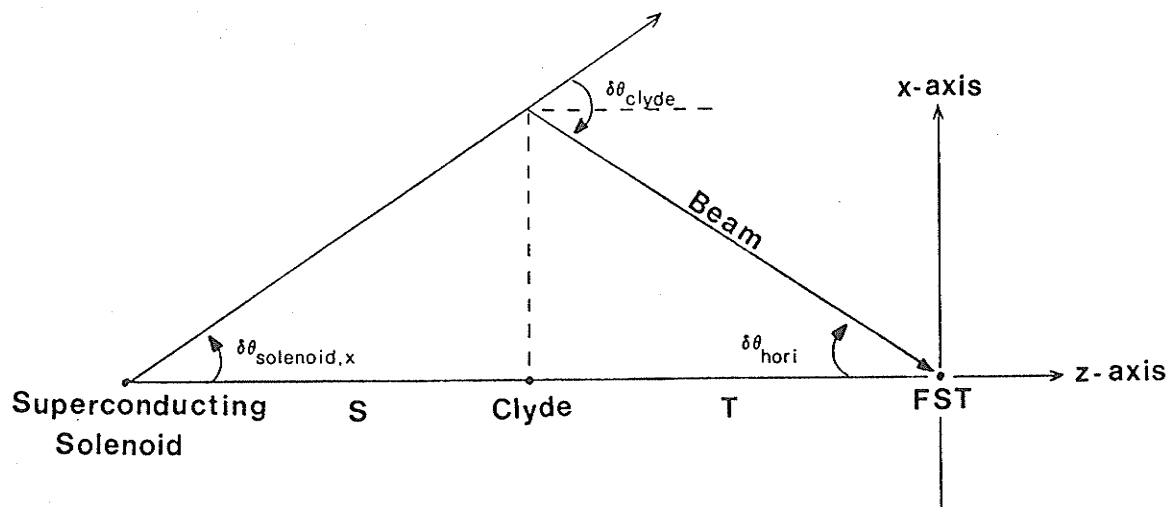
$$\delta\theta_{\text{Clyde}} = \delta\theta_{\text{FST}} \frac{(\int B \cdot dl)_{\text{Clyde}}}{(\int B \cdot dl)_{\text{FST}}} \quad (44)$$

The sign convention used in the above magnetic field deflection angles is illustrated in [Fig. 32]. The unprimed coordinate system corresponds to the incident proton reference frame at the FST center when the proton is travelling along the positive z-axis. The primed coordinate system corresponds to the incident proton reference frame when the proton is now travelling along the positive z'-axis as a result of the magnetic field deflection angle, θ . The deflection angles as illustrated were defined positive.

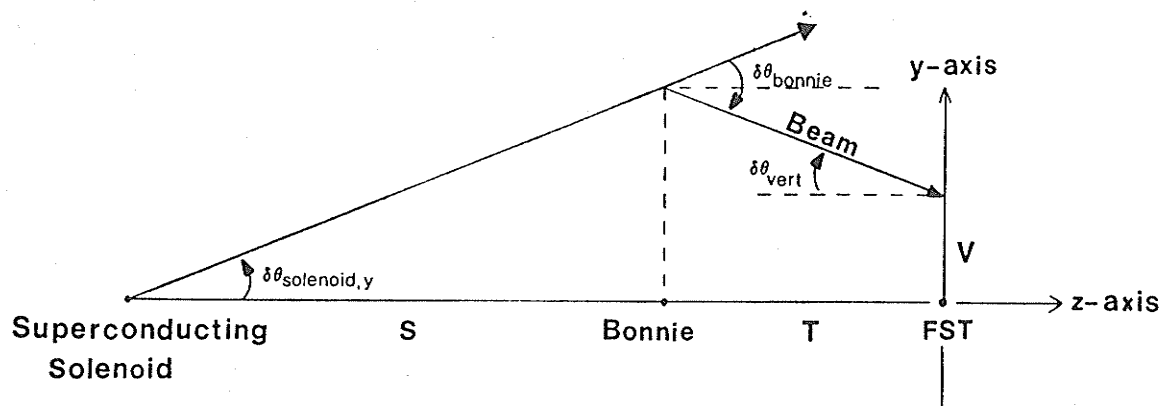
The total horizontal deflection angles tabulated in [Table 4], were calculated by using [Eq. 43], [Eq. 44] and [Table 8].

IV.2.a.3.iii Magnetic Field Deflection Due to Superconducting Solenoid and Vertical Steering Magnet

The dipole magnet "Bonnie" had two functions: to compensate for



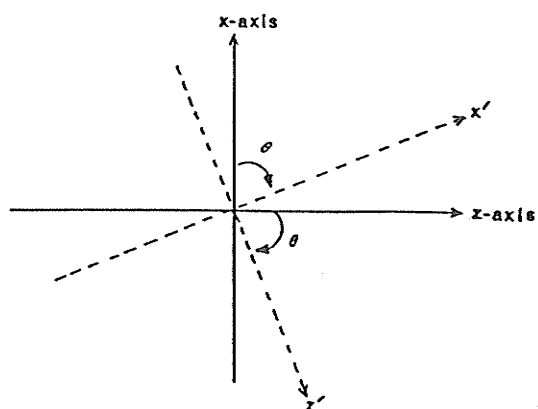
(a) Horizontal deflection angle geometry.



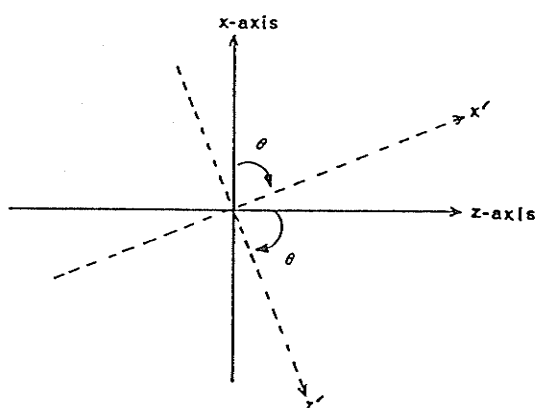
(b) Vertical deflection angle geometry.

[Fig. 31]

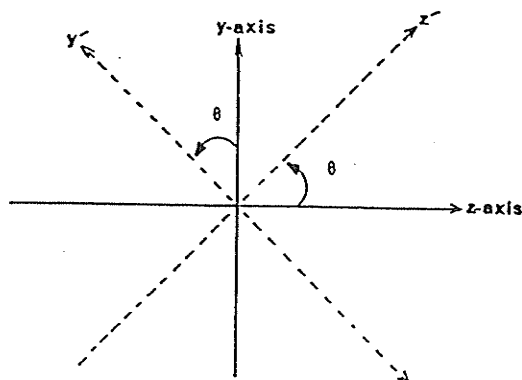
Magnetic field deflection angle geometry
for the incident beam protons.



(a) FST holding field deflection angle.



(b) Horizontal (or "Clyde") deflection angle.



(c) Vertical (or "Bonnie") deflection angle.

[Fig. 32]

Incident proton beam magnetic field deflection angle sign convention. All of the above deflections were defined as positive.

the possible horizontal misalignment in the superconducting solenoid and to steer the incident proton beam so as to illuminate the vertical extent of the target cell. The incident proton vertical deflection angle, resulting from the superconducting solenoid and vertical steering magnets' field, was calculated from

$$\delta\theta_{\text{Vert}} = \frac{S \cdot \delta\theta_{\text{Bonnie}} - V}{S + T} \quad (45)$$

which was derived from geometrical considerations of [Fig. 31b]. The distances T and S are defined as before but now with respect to the vertical steering magnet. The deflection angle $\delta\theta_{\text{Bonnie}}$ was calculated using an equation similar to [Eq. 44]. The value of V, which varied between "Bonnie" DAC settings, was determined from the difference between the y-coordinate target image centroid and the y = 0 point (center of FST as determined from the radiographs). [Table 23] tabulates the various values of V as a function of "Bonnie" DAC setting. The sign convention that was used in the above magnetic field deflection angles has also been illustrated in [Fig. 32].

The total vertical deflection angles stated in [Table 5] were calculated using [Eq. 45], [Table 8], [Table 23] and an equation similar to [Eq. 44].

IV.2.a.4 FST Image Reconstruction

To ensure that the p-p scattering events originated within the FST sample, software cuts were imposed on the FST coordinate images. To project the incident proton beam, say, along the FST x-coordinate, this would require both horizontal drift chambers to have had a valid x-coordinate return. The track efficiency would be the product of the

[Table 23]

FST y-coordinate Image Centroid

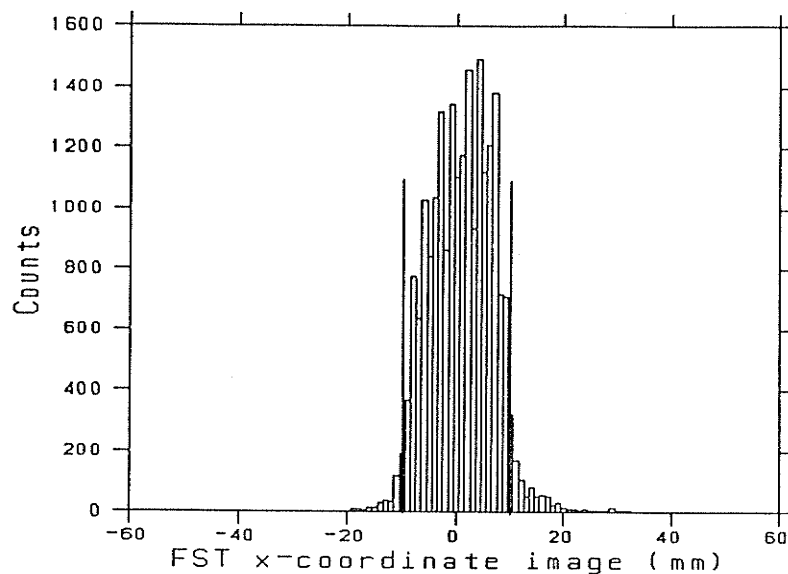
"Bonnie" DAC setting	Centroid	
	LH2 runs (mm)	C runs (mm)
0.00		2.98
0.01		3.76
0.01 ³³		-9.01
0.02	1.52	
0.05		8.46
0.05 ³³		-9.46
0.07	6.56	
0.10		13.98
0.10 ³³		-9.80
0.11	10.03	
0.15	14.46	

³³The polarity of "Bonnie" was interchanged.

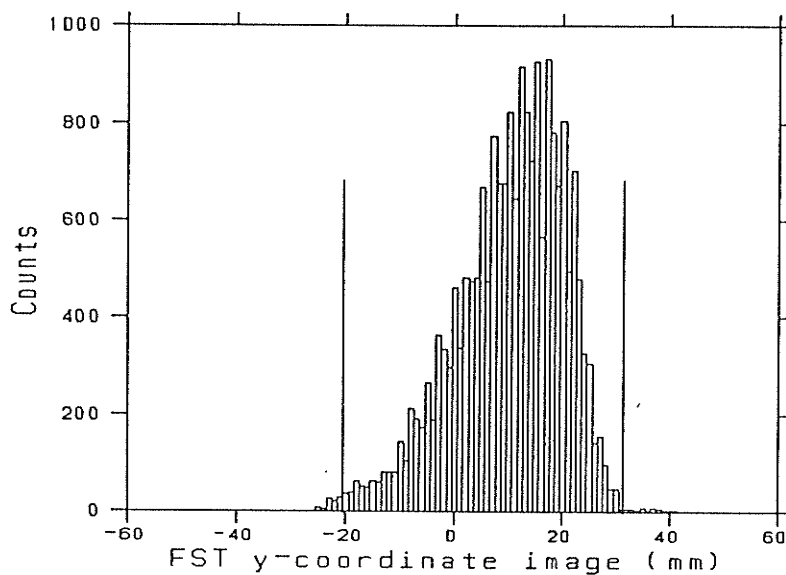
x-coordinate efficiency (ϵ) of both drift chambers, which was defined as

$$\epsilon = \frac{\text{number of events with valid coordinate return}}{\text{number of triggered events}} \quad (46)$$

The drift chambers typically had a x(y)-coordinate efficiency of 0.81 (0.87) which implies that the track efficiency would have been 0.66 (0.76) respectively. It is seen then that by requesting both drift chambers to have a valid coordinate return for a given event, fewer events would satisfy this condition thus reducing the experimental statistics when using FST image reconstruction as one of the data rejection conditions. In addition to the above difficulty, the true incident proton trajectory could not have been correctly represented by track reconstruction, for the reason that the true track was not straight as a result of magnetic field deflections. To allow us to retain the FST image reconstruction as a data rejection test, the coordinate distributions of the drift chamber nearest to the FST (located 67.2 cm upstream of the target) were used to depict the FST image. On the average 81 (87)% of the FST p-p scattering events fell within the x(y)-coordinate software cuts of the FST image, depicted as vertical lines in [Fig. 33]. Because the y-coordinate dimension of the incident beam was smaller than the physical y-coordinate dimensions of the target cell, runs were performed with different "Bonnie" DAC settings (thus steering the incident beam) to illuminate the vertical extent of the target cell. The cuts in [Fig. 33b] were deliberately chosen so as to enclose the various horizontal drift chamber y-coordinate distributions. The sharp edge in the y-coordinate distribution [Fig. 33b] is due to the physical cut off of the incident



(a) FST x-coordinate image, when using a "Bonnie" and "Clyde" DAC setting of 0.15 and 0.02 respectively.



(b) FST y-coordinate image, when using a "Bonnie" and "Clyde" DAC setting of 0.15 and 0.02 respectively.

[Fig. 33]

FST images obtained from the nearest horizontal drift chamber coordinate distributions during run 213.

proton beam by the top of the target cell. The tail of the distribution illustrates the lower tail of the incident beam about the vertical direction.

IV.2.b Scattered and Recoil Proton Analysis

IV.2.b.1 Track Reconstruction

As the scattered protons traversed the four DLCs mounted on the scattered proton detector system, each DLC provided x- and y-coordinates. But, because the position of the proton intersection for a given DLC coordinate was determined from the time difference of the TDCs located on opposite ends of the coordinate delay-line, the coordinate return may not have been a valid one, due to the TDC timeouts. To ensure relatively high track efficiencies the first two and last two DLCs were grouped together to form two pairs. In this way if one DLC in the pair had an invalid coordinate return the second DLCs coordinate return could still be used. Because of this arrangement, at least one x- and y-coordinate must be found in each pair. The software track reconstruction was then determined from a least squares fit to the track coordinates as obtained from the four DLCs.

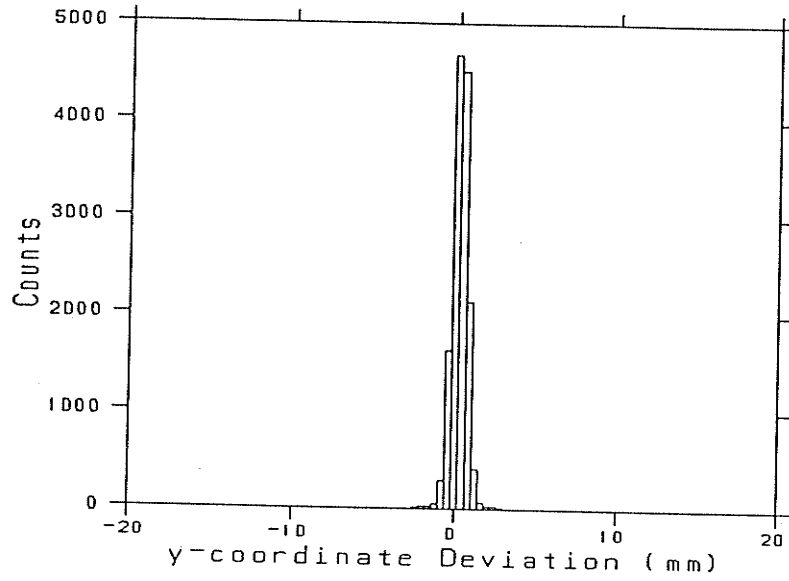
Each scattered proton detector was aligned via software, by allowing the centers of the FST coordinate images as deduced from the scattered proton track back projections, to coincide with the x-ray radiograph coordinate centers. The alignment was made by adjusting a x- and a y-coordinate global offset that was added to the x- and y-coordinate return of each of the four DLCs.

[Fig. 34] illustrates the typical DLC coordinate resolution found during the experiment. The resolution, defined as the difference between the actual DLC coordinate return and that of the least squares fit, was found to be ± 1.4 (± 0.8) mm (at FWHM) for the left event DLC 3 x(y)-coordinate. The DLC coordinate resolution centroids were set as close as possible to zero, by adjusting the coordinate return of each DLC with the addition of a small offset via software. The difference in the x-and y- coordinate resolutions for a given DLC is attributed to the intrinsic coordinate resolution that arises from whether the coordinate had the cathode strip plane parallel or perpendicular [Table 13] to the anode wire plane. The deviations from the intrinsic resolution (which is ± 1 (± 0.7) mm for a coordinate with cathode strip plane parallel (perpendicular) to the anode wire plane) are due to multiple scattering and the coordinate nonlinearities.

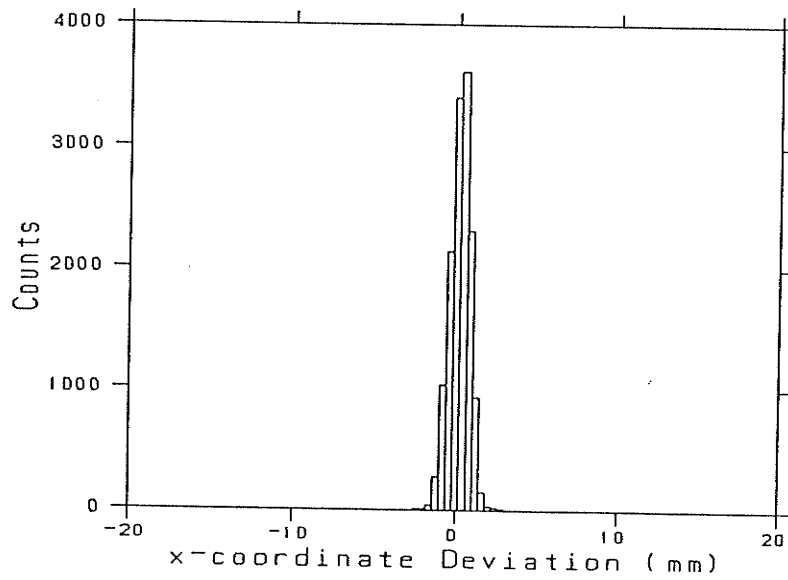
The average individual DLC coordinate efficiencies (ϵ), defined as [Eq. 46], observed during both calibration experiments are tabulated in [Table 24]. The individual DLC coordinate efficiencies were then used to calculate the track efficiency from

$$\begin{aligned} \epsilon_{\text{track}} = & \epsilon_1 \epsilon_2 \epsilon_3 \epsilon_4 + \epsilon_1 \epsilon_2 \epsilon_3 (1 - \epsilon_4) + \epsilon_1 \epsilon_2 (1 - \epsilon_3) \epsilon_4 \\ & + \epsilon_1 (1 - \epsilon_2) \epsilon_3 \epsilon_4 + (1 - \epsilon_1) \epsilon_2 \epsilon_3 \epsilon_4 + (1 - \epsilon_1) \epsilon_2 \epsilon_3 (1 - \epsilon_4) \\ & + \epsilon_1 (1 - \epsilon_2) \epsilon_3 (1 - \epsilon_4) + (1 - \epsilon_1) \epsilon_2 (1 - \epsilon_3) \epsilon_4 \\ & + \epsilon_1 (1 - \epsilon_2) (1 - \epsilon_3) \epsilon_4 \end{aligned} \quad (47)$$

where ϵ_1 through ϵ_4 are the coordinate efficiencies for DLC1 to DLC4. [Eq. 47] determines the coordinate track efficiency from the sum of all of the possible combinations the four DLCs can have a valid (ϵ) coordinate return, provided that at least one valid coordinate return is attained in each of the front and back DLC pairs. The total track



(a) Vertical coordinate resolution.



(b) Horizontal coordinate resolution.

[Fig. 34]

Coordinate resolution spectra for left event DLC 3, during run 271.

[Table 24]

Average DLC Coordinate Efficiencies

DLC identification	Coordinate	Average DLC efficiencies (ϵ)			
		Left events		Right events	
		LH2 runs	C runs	LH2 runs	C runs
Scattered proton detector:					
DLC 1	x	0.911	0.880 ³⁴	0.895	0.900
	y	0.912	0.848 ³⁴	0.901	0.889
DLC 2	x	0.934	0.931	0.938	0.922
	y	0.927	0.933	0.921	0.938
DLC 3	x	0.914	0.916	0.915	0.909
	y	0.922	0.904	0.913	0.914
DLC 4	x	0.930	0.907	0.910	0.927
	y	0.916	0.919	0.911	0.933

³⁴Due to a malfunction in the left event DLC1 during the $A_{yy}(\theta)$ data collection period (prior to the second calibration experiment), the chamber was replaced. The somewhat lower coordinate efficiencies could be due to incorrect discriminator level settings.

efficiency for either left or right event scattered proton detector systems was then calculated from

$$\epsilon_{\text{track,total}} = \epsilon_{\text{track,x}} \cdot \epsilon_{\text{track,y}} \quad (48)$$

where $\epsilon_{\text{track,x}}$ and $\epsilon_{\text{track,y}}$ are the individual x- and y-coordinate track efficiencies. The total track efficiencies for left and right events, for both calibration experiments, were typically around 0.97.

The track reconstruction of the recoil protons was determined by performing the following steps:

- (a) the scattered proton track was projected back to the FST $x = 0$ plane, which was used as the coordinate for the origin of the events (the $x = 0$ plane was preferred over the $z = 0$ and $y = 0$ FST image planes for the reason that the x-coordinate dimensions of the target chamber are much smaller, thus introducing less uncertainty to the origin coordinates);
- (b) the x- and y-coordinate return of the recoil proton detector systems DLC provided a second point; and
- (c) a straight line through the above two points was then used to represent the recoil proton track.

IV.2.b.2 Time of Flight

The scattered proton TOF information was obtained from the TOF start and stop scintillators mounted on the scattered proton detector boom [Fig. 12]. The timing signal from the TOF start scintillator was obtained as the software average of the top and bottom photomultiplier tube signals. There was no position dependent correction to the net timing signal since this detector had dimensions of 17.5 cm by 17.5 cm.

The TOF stop scintillators on the other hand, were made large due to the substantial increase in the scattered proton projected area, the TOF stop scintillator was placed 3034 mm downstream of the TOF start scintillator. The TOF stop scintillator timing signals were taken to be the software average of the signals that were produced by the photomultiplier tubes that had fired [Fig. 24]. Because of the TOF stop scintillator large dimensions, 67 cm by 67 cm, the timing signals had to have a position dependent correction.

To aid in the TOF stop scintillators signal averaging, the stop scintillator was segmented into five regions [Fig. 35]. Region 5 corresponded to protons that traversed the central region of the scintillator and the net timing signal was taken over the four individual photomultiplier tube signals. Region 1 on the other hand corresponded to protons traversing the top left hand corner of the scintillator and the net timing signal was taken by requiring only three of the four photomultiplier tube signals. The photomultiplier tube that was positioned horizontally across, in this case the photomultiplier tube nearest to region 2, was not considered in the software signal average for the reason that it had bad light geometry thus having unreliable signal information. A similar discussion can be made for regions 2, 3 and 4.

The position dependent correction to the TOF stop scintillator net signal was accomplished by dividing the entire stop scintillator into a grid pattern consisting of 18 segments along the x-axis and 28 segments along the y-axis. The transit times from each of these 504 elements to the various photomultiplier tubes had been previously determined prior

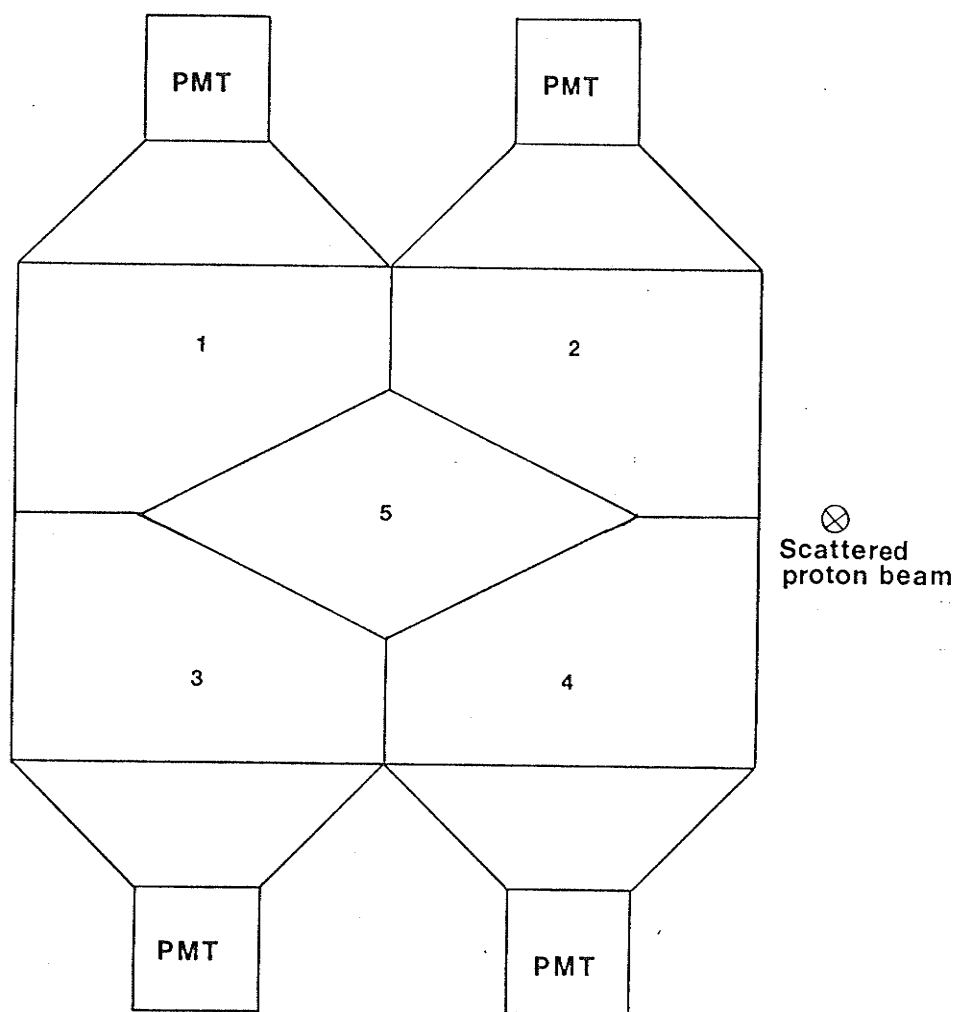


[Fig. 35]

Scattered proton TOF stop scintillator
region segmentation.

to the "Test of Charge Symmetry Breaking" experiment. The assignment of a particular element was achieved by projecting the scattered proton track to the TOF stop scintillator position and determining the point of intersection. The coordinates of this point, which are in the DLC coordinate system were then transformed into the 18 x 28 array coordinate system. During the analysis, the position dependent correction was subtracted from the software TDC sum of the various photomultiplier tube signals. The TOF for the scattered proton was then determined using [Eq. 40] with the various adjustments for the electronic delays.

During both calibration experiments, scattered proton TOF cuts were imposed on each of the 5 TOF stop scintillator regions for both left and right events, thus allowing the removal of some of the lower energy scattered protons.

The TOF efficiency was calculated using

$$\epsilon_{\text{TOF}} = \epsilon \cdot \epsilon_{\text{track, total}} \quad (49)$$

where ϵ is the number of times the TOF stop scintillator had a valid event (event firing 3 or 4 photomultiplier tubes) divided by the number of valid scattered proton tracks (which were defined as events whose proton tracks had at least one valid x- and y- coordinate return from each of the two DLC pairs). Because the efficiency ϵ was defined with respect to the number of valid scattered proton tracks, to make ϵ_{TOF} in terms of the number of trigger events, ϵ is multiplied by $\epsilon_{\text{track, total}}$. ϵ was typically 0.99 for both left and right events. The total scattered proton detection system efficiency was then calculated using

$$\epsilon_{\text{T}} = \epsilon_{\text{track, total}}^2 \cdot \epsilon \quad (50)$$

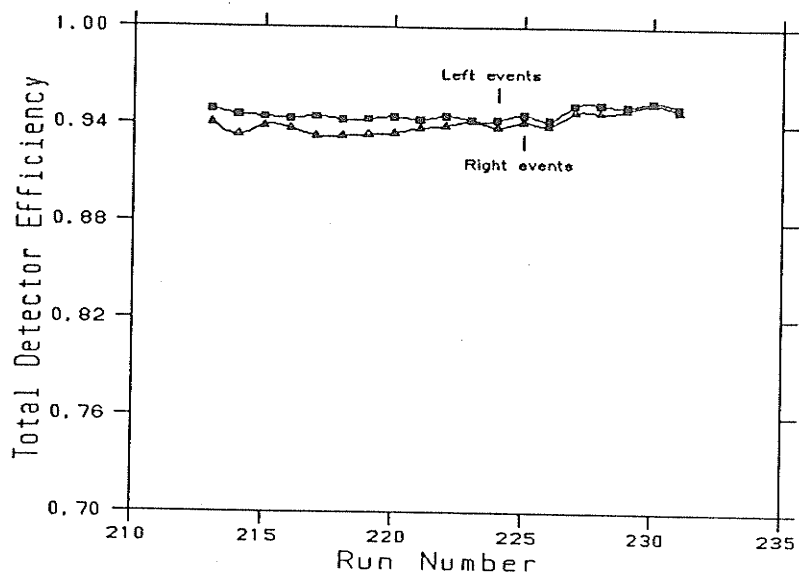
The recoil protons TOF efficiency was not used in [Eq. 50], for the reason that the recoil proton TOF stop scintillator must provide a valid hit to produce a valid coincident event. [Fig. 36] illustrates the variation in total detector efficiency with runs, for both calibration experiments. The general drop in the left event ϵ_T values during the C runs (as opposed to the LH2 run values), was attributed to the drop in the left event DLC1 efficiency [Table 24].

The recoil proton TOF was determined by using the TOF stop scintillator in the scattered proton detector system to produce the TOF start signal and the software averaged signal of the $A_{yy}(\theta)$ experiments central veto scintillator as the TOF stop signal. The TOF for the recoil proton was then calculated from

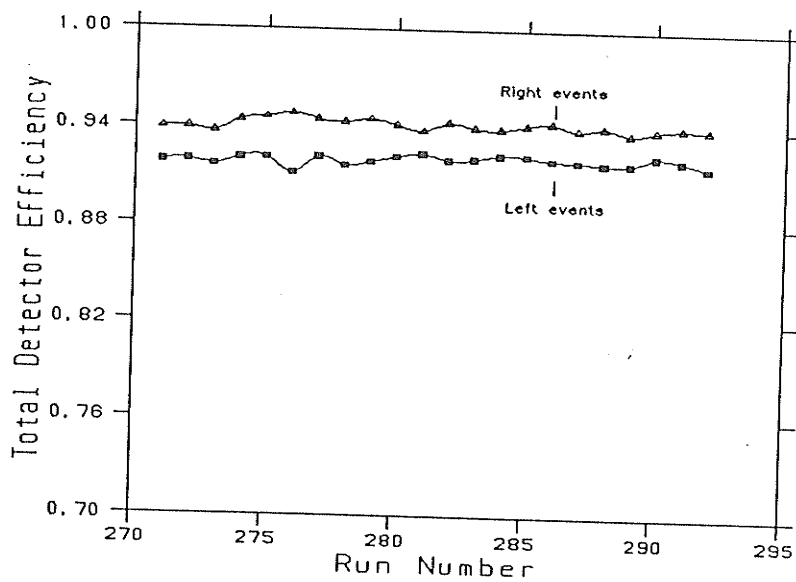
$$r\text{-TOF} = t_{\text{stop}} - t_{\text{start}} + \frac{410}{3444}(p\text{-TOF}) \quad (51)$$

where t_{stop} and t_{start} are the timing signal information (in ns) from the stop and start scintillators; p-TOF is given by [Eq. 40] for the scattered proton TOF. The third term in [Eq. 51] is the time it took the scattered proton to travel from the FST center to the TOF start scintillator location on the scattered proton detector system. Defining the recoil proton TOF in this way ensured coincident event identification. Software cuts were also imposed on the recoil proton TOF spectra. On the average, 93% of the FST p-p scattering events fell within these TOF software cuts, which are illustrated as vertical lines in [Fig. 37].

The low energy tails observed in [Fig. 37] are largely due to the energy losses of the protons as they traverse the various materials between scattering center within the FST and TOF stop scintillator. The



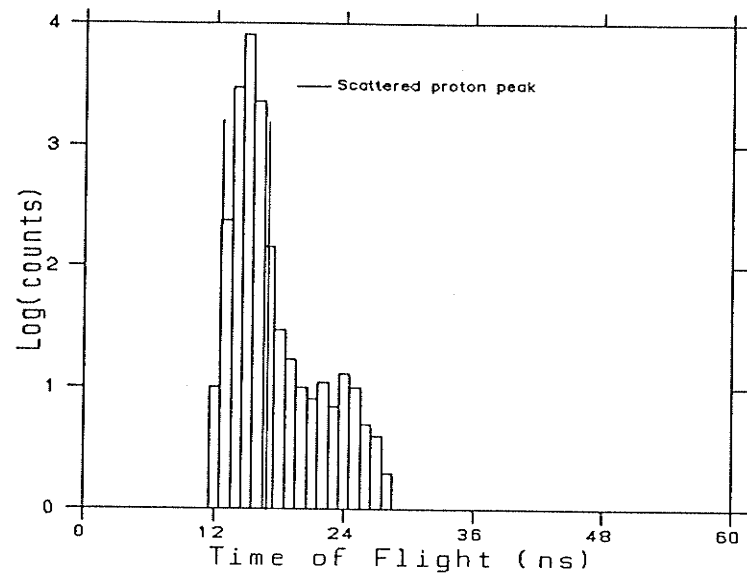
(a) For LH2 runs.



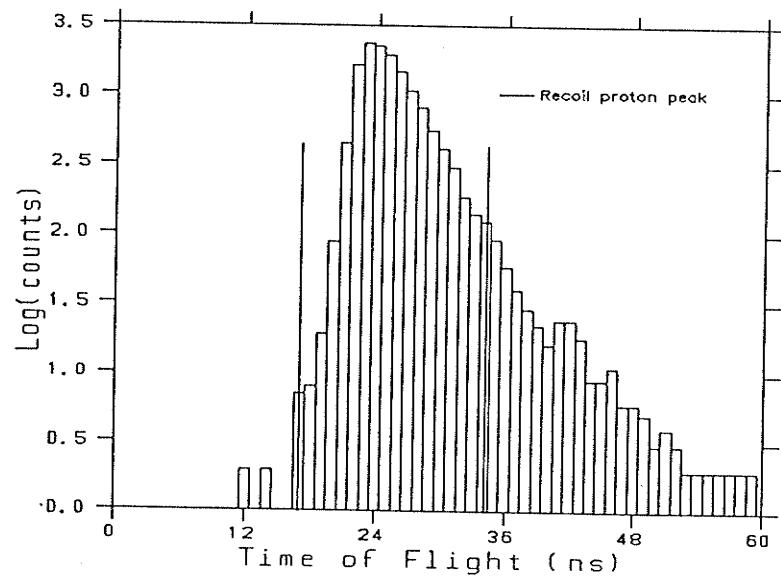
(b) For C runs.

[Fig. 36]

Total detector efficiency
variation with run number.



(a) TOF spectrum for scattered protons that projected within region 5 of the TOF stop scintillator.



(b) Recoil proton TOF spectrum.

[Fig. 37]

Scattered and recoil proton TOF spectra obtained during run 213 for left events.

amount of energy a given proton would have lost will depend on the angle at which it was scattered and the amount of multiple scattering that it had undergone. During both calibration experiments, the amount of multiple scattering typically undergone by the scattered and recoil proton (when being scattered, at 24° (lab) and 61° (lab)) was in the order of 0.6° and 1.1° respectively.

IV.2.b.3 Proton Energies and Momenta

The scattered proton energy was determined from the TOF information and the path length of the track between both TOF scintillators. The energy determined in this way is the average experimental energy (E_{exp}) of the scattered proton at the location of the TOF stop scintillator. The theoretical proton energy was calculated from

$$E_{\text{theo}} = E_{\text{kin}} - E_{\text{loss}} \quad (52a)$$

where E_{kin} is the kinematically expected energy and E_{loss} the energy the scattered proton would have lost as it traversed the various materials within its path. Both of the terms in [Eq. 52a] are a function of the proton scattering angle. E_{kin} was determined from the following relativistic expression

$$E_{\text{kin}} = \frac{2E_0 E_{\text{in}} \cos^2 \theta}{2E_0 + E_{\text{in}} \sin^2 \theta} \quad (52b)$$

where θ is the proton scattering angle in the laboratory reference frame, E_0 is the proton rest mass (in MeV) and E_{in} is the incident proton energy (in MeV) at the centre of the FST target.

The scattered proton energy error, defined as,

$$\Delta E = E_{\text{exp}} - E_{\text{theo}} \quad (53)$$

was reduced to near zero for each of the 5 TOF stop scintillator regions, for both left and right events. This was done by adding a constant to the timing signal to account for the electronic delays. This procedure enabled the centroid of the experimental energy of the scattered proton, as determined from a given region in the TOF stop scintillator, to be as close as possible to the theoretical energy. The experimental scattered proton energy at the PST sample scattering center location, was then determined using

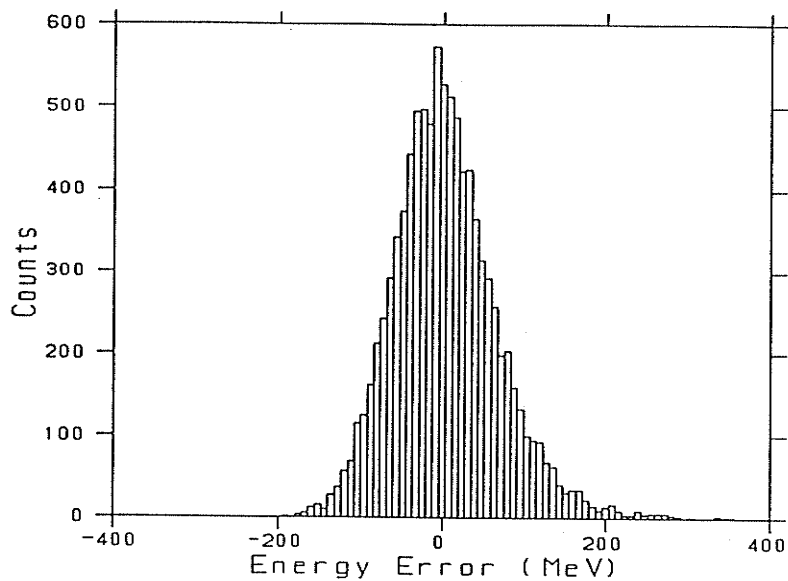
$$E = E_{\text{exp}} + E_{\text{loss}} \quad (54)$$

The scattered proton momentum could then be determined from [Eq. 54] by

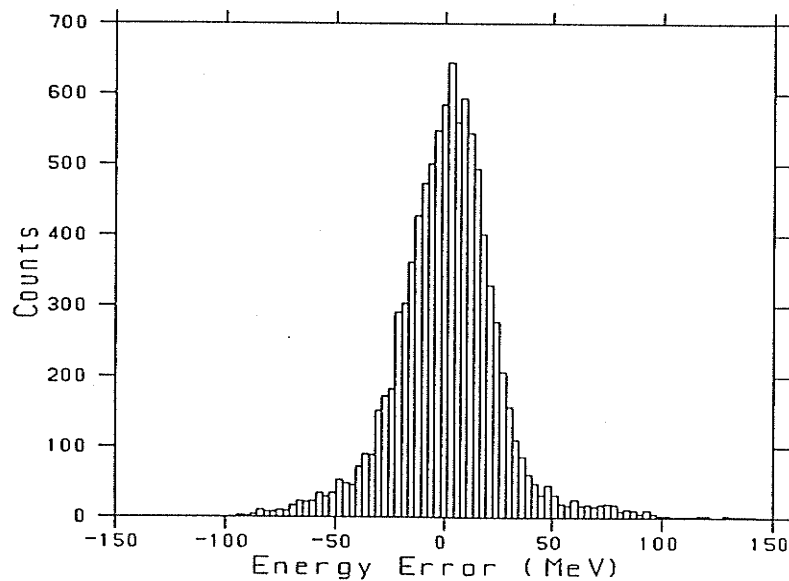
$$pc = [(E+E_0)^2 - E_0^2]^{1/2} \quad (55)$$

where E_0 is the rest mass of the proton (in MeV), p is the proton momentum (in $\text{MeV} \cdot c^{-1}$) and c is the speed of light.

The recoil proton energy and momentum were calculated using a method analogous to the procedure used above for the scattered proton energy. [Fig. 38] illustrates typical recoil and scattered proton energy error spectra as determined from [Eq. 53]. The widths of the energy error spectra were typically 48 MeV and 13 MeV (one standard deviation, σ) for the scattered and recoil protons respectively. The widths of these spectra are attributed to the timing resolution of the detectors (dominated by the timing signal from the TOF start scintillator), the energy spread of the incident beam and multiple scattering. The high energy tail in [Fig. 38a] resulted from the selection of the high energy TOF software cut in the scattered protons TOF spectra. To fine tune



(a) Scattered proton spectra.



(b) Recoil proton spectra.

[Fig. 38]

Scattered and recoil proton energy errors
observed during run 271 for left events.

the net scattered proton energy error distribution a global offset was added to each of the 5 TOF stop scintillator regions timing signals, for both left and right events. The centroid deviation from zero for the net scattered proton energy error distribution was a result of the fine tuning offset setting. The recoil proton energy error centroid deviation from zero was also a result of TOF offset settings.

IV.2.b.4 Scattered and Azimuthal Angles

For the scattered and recoil protons, the scattering and azimuthal angles are determined with respect to the incident proton direction. For the uncorrected³⁵ angles, the incident proton direction was assumed to be parallel to the positive z-axis. For a given scattered proton, the scattered angle, θ , was calculated from

$$\theta = \cos^{-1} \left[\frac{\hat{z} \cdot \vec{p}_s}{|\vec{p}_s|} \right] \quad (56)$$

where \vec{p}_s is the scattered proton momentum vector whose components are deduced from the reconstructed track. The azimuthal angle ϕ , in turn was calculated from

$$\phi = \tan^{-1} \left[\frac{\vec{p}_s \cdot \hat{y}}{\vec{p}_s \cdot \hat{x}} \right] \quad (57a)$$

³⁵These are the scattered and azimuthal angles calculated without any consideration of the FST holding field.

and was taken to be

$$\begin{aligned}
 \phi &= \Phi + 180^\circ && \text{if } \Phi < 0^\circ \text{ and } \vec{p}_S \cdot \hat{x} < 0 \\
 &= \Phi && \text{if } \Phi \geq 0^\circ \text{ and } \vec{p}_S \cdot \hat{x} > 0 \\
 &= 180^\circ + \Phi && \text{if } \Phi \geq 0^\circ \text{ and } \vec{p}_S \cdot \hat{x} < 0 \\
 &= 360^\circ + \Phi && \text{if } \Phi < 0^\circ \text{ and } \vec{p}_S \cdot \hat{x} > 0
 \end{aligned} \tag{57b}$$

The scattering and azimuthal angles were defined positive in the regions $0 < \theta < \pi$ and $0 < \phi < 2\pi$, and have been illustrated in [Fig. 39] for a proton which had undergone scattering with a proton incident along the z-axis of the experimental coordinate system.

As the scattered and recoil protons traversed the FST holding field, they underwent a deflection in the x - z plane. This deflection can be calculated from an equation similar to [Eq. 42]

$$\delta\theta = \frac{\alpha}{|\vec{p}_S| [\cos^2\theta + \sin^2\theta \cos^2\phi]^{\frac{1}{2}}} \tag{58}$$

where α takes on values shown in [Table 22]. The holding field corrected scattering angle, θ' , was then calculated from

$$\theta' = \cos^{-1} \left[\frac{\vec{p}'_{in} \cdot \vec{p}'_S}{|\vec{p}'_{in}| |\vec{p}'_S|} \right] \tag{59}$$

where \vec{p}'_{in} and \vec{p}'_S are the magnetic field corrected momentum vectors for the incident and scattered protons. The corrected momentum vector components were obtained from the uncorrected components by performing the following rotation

$$\begin{bmatrix} \sin\theta' \cos\phi' \\ \sin\theta' \sin\phi' \\ \cos\theta' \end{bmatrix} = \begin{bmatrix} \cos(\delta\theta) & 0 & -\sin(\delta\theta) \\ 0 & 1 & 0 \\ \sin(\delta\theta) & 0 & \cos(\delta\theta) \end{bmatrix} \begin{bmatrix} \sin\theta \cos\phi \\ \sin\theta \sin\phi \\ \cos\theta \end{bmatrix} \tag{60}$$

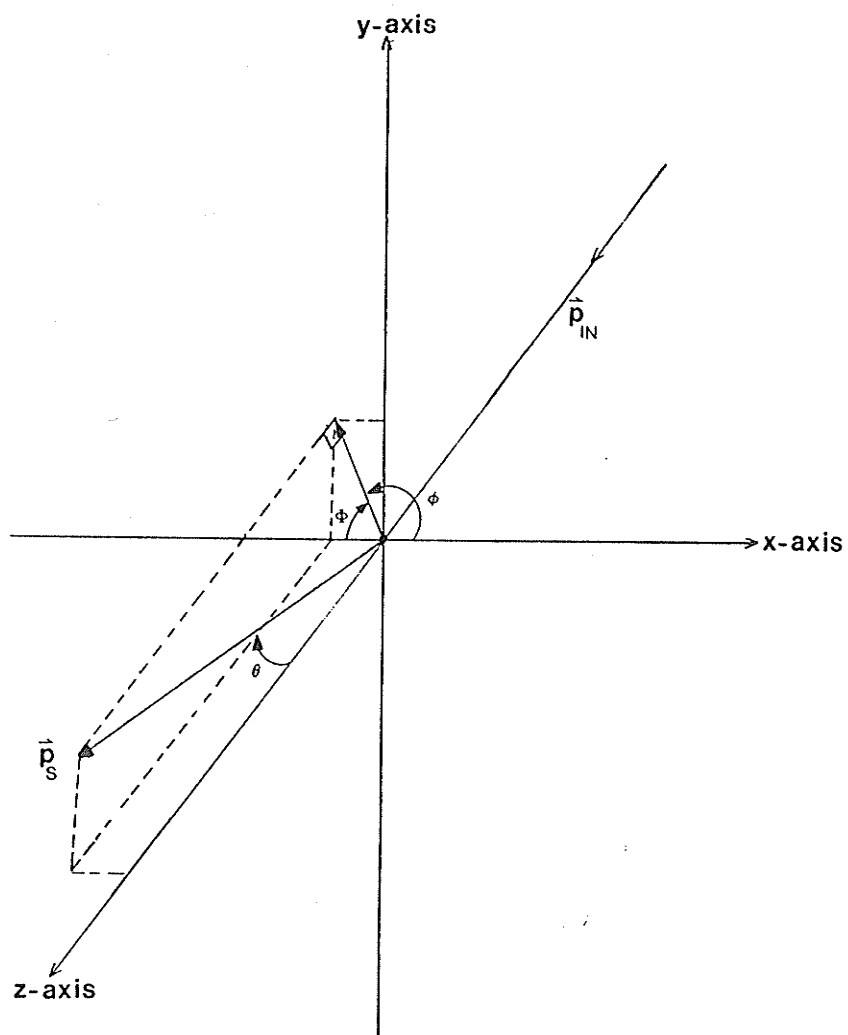


[Fig. 39]

Scattering and azimuthal angle
coordinate definitions.

which led to the equations:

$$\begin{aligned}
 \sin\theta' \cos\phi' &= \cos(\delta\theta) \sin\theta \cos\phi - \sin(\delta\theta) \cos\theta \\
 \sin\theta' \sin\phi' &= \sin\theta \sin\phi \\
 \cos\theta' &= \sin(\delta\theta) \sin\theta \cos\phi + \cos(\delta\theta) \cos\theta
 \end{aligned}
 \tag{61}$$

The use of the above rotation matrix can be explained by considering [Fig. 40]. Because the FST holding field was along the positive y-axis, a proton along a track depicted by the solid line underwent a deflection $\delta\theta$. The proton detectors then observed the proton to have a track depicted by the dashed line. Thus, to correct the proton momentum vector for the holding field deflection, $\delta\theta$ must be subtracted from the observed scattering angle θ . In other words, we must rotate the observed proton track by $\delta\theta$ in the counterclockwise direction. $\delta\theta$ in [Eq. 60, 61] is defined positive in the direction opposite to that illustrated in [Fig. 40].

[Eq. 60] and [Eq. 61] hold true for both scattered and recoil protons, but when these equations are used for the incident protons, the sign of $\delta\theta$ is reversed. This arises from the fact that the scattered and recoil protons are detected after they had undergone their deflection whereas the incident protons are detected (from the nearest horizontal drift chamber x- and y- coordinate distributions) before their deflection.

Typical total corrections to the scattering angles observed for the scattered (recoil) protons were 1.50° (2.30°) during the LH2 calibration experiment. Approximately 0.65° of these total deflections were due to the incident proton deflection. The systematic error contribution to the FST polarization measurement due to incorrect estimates of the deflection angles was calculated to be 0.02% (see Appendix C), which is

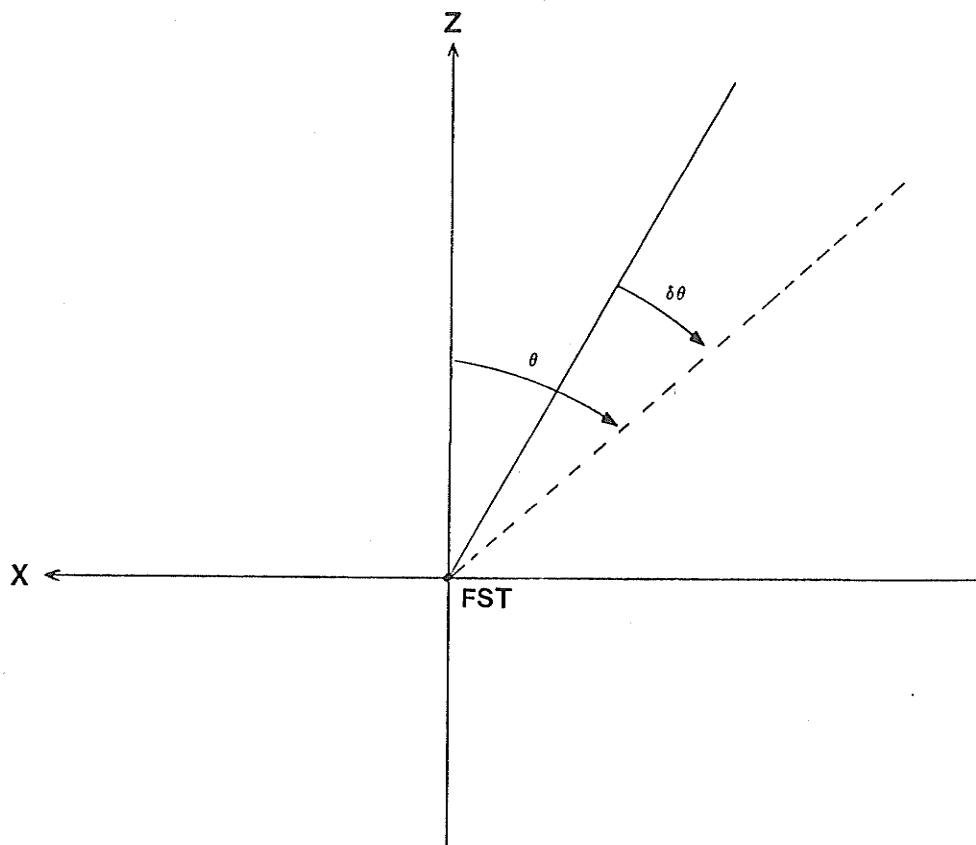


[Fig. 40]

FST holding field deflection
angle illustration.

negligible when compared to a 0.22% (see Appendix C) systematic error contribution that arose from a $\pm 0.05^\circ$ uncertainty in determining the proton detector physical angle settings.

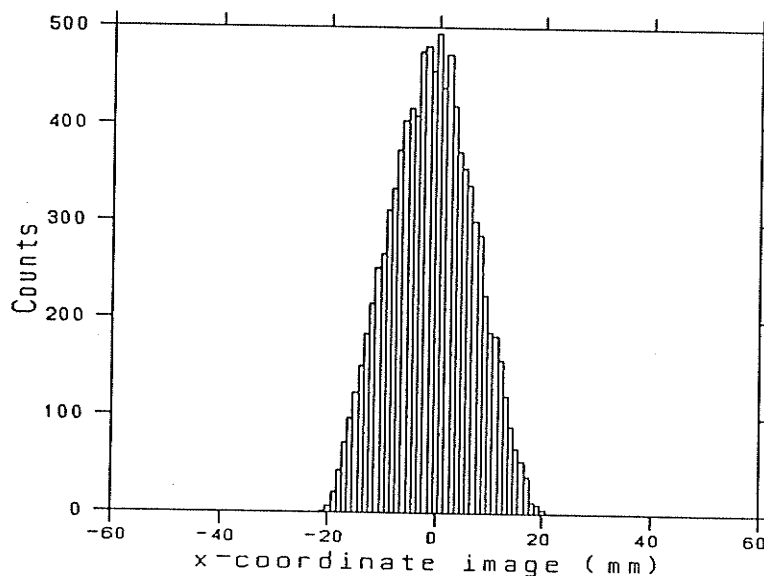
IV.2.b.5 FST Image Reconstruction

The FST image was also reconstructed for both left and right events by projecting the scattered proton tracks back to the FST y-z plane. Because the back-projected points were in the scattered proton detectors coordinate system they were mapped onto the experimental coordinate system by the proper geometric transformation. [Fig. 41] illustrates the FST x- and z-coordinate image reconstructions.

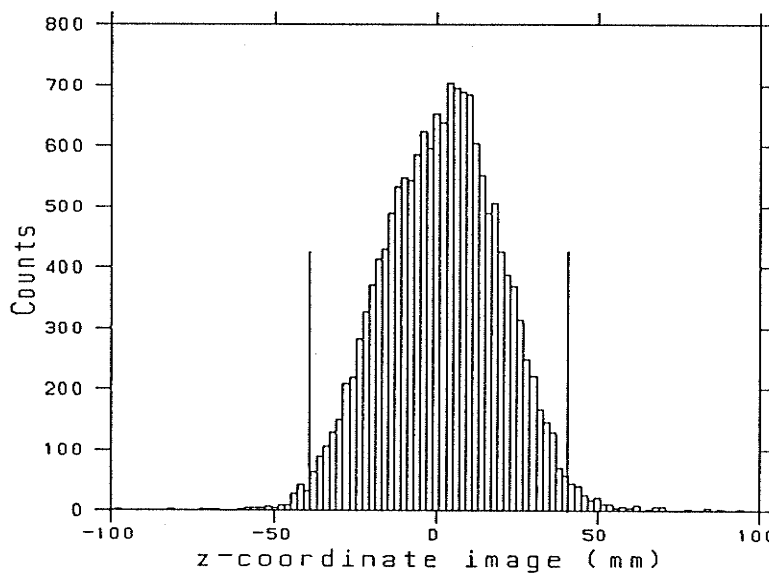
When a comparison is made between [Fig. 33a] and [Fig. 41a], the FST x-coordinate image reconstructed from the scattered proton tracks is observed to be not as well defined. This arose from the multiple scattering the scattered protons underwent as they traversed the FST, which was in the order of 0.6° (determined from the projected mean multiple scattering angle). Because of this effect, the FST x- and y-coordinate image software cuts were placed on the images as produced by the horizontal drift chamber nearest the FST. The FST z-coordinate image cuts [Fig. 41b] were placed on the image as produced by the scattered proton tracks and because of the multiple scattering were deliberately chosen to be loose. On the average, 93% of the FST proton scattering events fell within this software cut.

IV.3 Data Rejection

A summary of the various software cuts that were used during the analysis of each run, with typical individual contributions is tabulated



(a) FST x-coordinate image reconstruction when using a "Bonnie" and "Clyde" DAC setting of 0.05 and 0.03 respectively.



(b) FST z-coordinate image reconstruction when using a "Bonnie" and "Clyde" DAC setting of 0.05 and 0.03 respectively.

[Fig. 41]

FST image reconstruction using the scattered proton track projections of run 271. During this run, the incident beam was steered via "Bonnie" to the top of the target chamber.

in [Table 25]. The calculation of the individual software cut contributions involved the sequential application of the "events passing cut" column in [Table 25]. The tabulated data were taken from the analysis of run 271.

It is seen from [Table 25] that out of the 101600 events recorded on tape 271, 98.72% were coincident events and 26.7% of these coincident events actually passed all of the software cuts, corresponding to good p-p elastic scattering events.

The software cut labelled as "badword" in [Table 25] was actually a bit map composed of 13 essential conditions that must be satisfied in order to process a valid p-p scattering event. The "badword" bit map is tabulated in [Table 26]. The incorporation of this software cut in the analysis aided in the removal of events that could not be processed (bits 1 through 15) and events that did not satisfy the scattered proton TOF cuts (bit 0). Of the 16 "Badword" bits, the two most dominant effects were bits 0 and 9 (bit number 9 corresponded to events that did not have a valid scattered proton track reconstruction), which comprised 39% and 31% of the events that failed the "Badword" conditions.

IV.4 Constraints Used to Identify Elastic Scattering Events

Because in a p-p elastic scattering event both kinetic energy and momentum are conserved, numerical constraints on their measured values can be used to identify the elastic events from the p-p scattering events. In the present analysis the following four kinematic constraints were used.

[Table 25]

Software Cut Rejection of Data

Description	Total number of events	Events passing cut	% passing cut
Event type 2	101600	100298	98.72
Not a pulser event	100298	95018	94.74
Badword	95018	60648	63.83
Incident proton TOF cut	60648	45686	75.33
Scattered proton track ($\chi^2 \leq 6$)	45686	41538	90.92
FST x image cut	41538	34398	82.81
FST y image cut	34398	31168	90.61
FST z image cut	31168	29011	93.08
Recoil proton TOF cut	29011	26800	92.38

[Table 26]

Badword Bit Map Summary

Bit Number	Description
0	Scattered proton TOF cuts
1	Spare - not assigned
2	Spare - not assigned
3	Scattered proton track projected outside of the TOF stop scintillator
4	Scattered proton TOF stop scintillator gave less than 3 TDCs signals
5	Scattered proton TOF stop scintillator gave less than 4 TDC signals when all should have been present
6	Scattered or recoil proton energy less than 10 MeV
7	Scattered proton TOF start scintillator up-TDC timeout
8	Scattered proton TOF start scintillator down-TDC timeout
9	Not a good scattered proton event
10	Not a good recoil proton event
11	Spare - not assigned
12	Scattered proton track 'OK' but invalid scattering angles
13	Cosine of coplanarity angle greater than 1
14	Both left and right events indicated by DCR
15	No left or right event indicated by DCR

IV.4.a Energy Sum

This constraint was determined from

$$\Delta E_{\text{sum}} = \Delta E_{\text{s}} + \Delta E_{\text{r}} \quad (62)$$

where ΔE_{s} and ΔE_{r} are the scattered and recoil proton energy errors, as defined in [Eq. 53] with magnetic field corrections to the proton tracks accounted for. [Fig. 42a] illustrates a typical energy sum error spectrum with width of 50 MeV (one σ). The width of this spectra was due to the widths of the scattered and recoil proton energy error distributions [see section IV.2.b.3]. This can be illustrated by adding the two widths in quadrature, that is

$$[(48)^2 + (13)^2]^{\frac{1}{2}} = 50 \text{ MeV}. \quad (62a)$$

The energy sum error distributions high energy tail was a result of the selection in the high energy TOF software cut in the scattered protons TOF spectra, whereas its centroid deviation from zero was attributed to the scattered and recoil proton centroid deviations in their energy error spectra.

IV.4.b Opening Angle

The second numerical constraint that was used, was the opening angle defined as

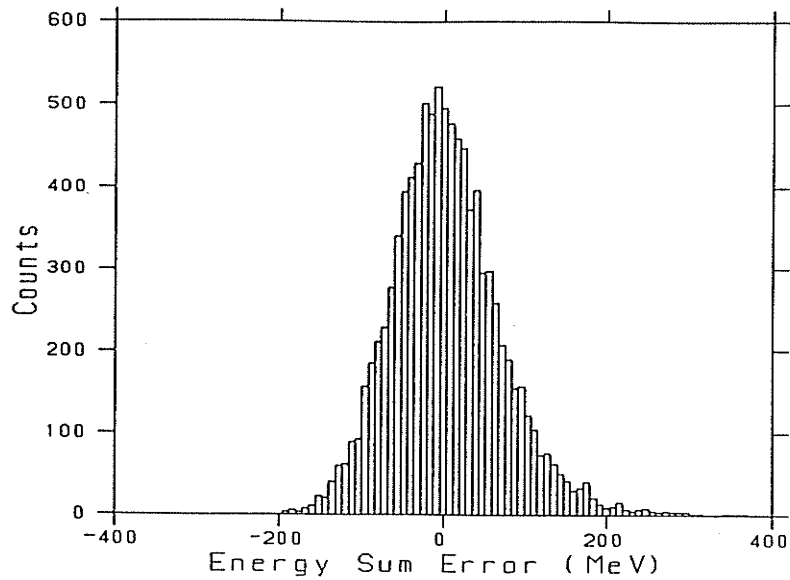
$$\theta_{\text{open}} = \theta'_{\text{s}} + \theta'_{\text{r}} \quad (63)$$

where θ'_{s} and θ'_{r} are the scattered and recoil proton scattering angles.

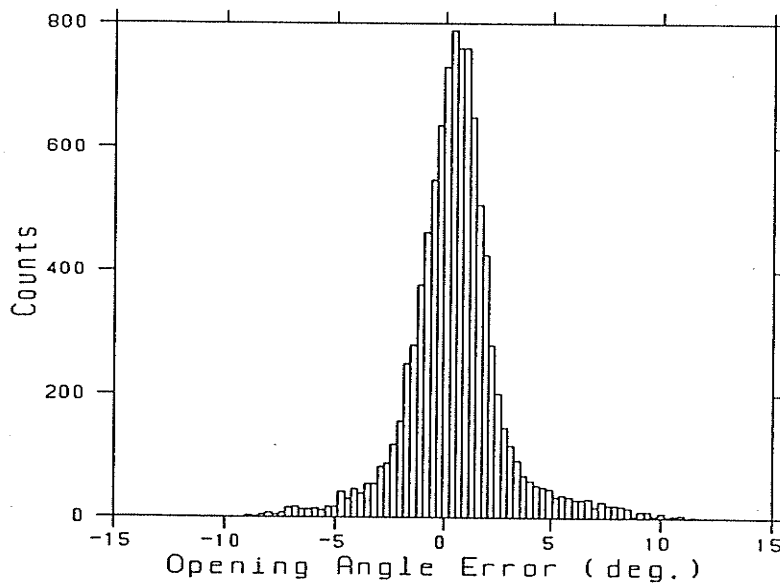
The experimental opening angle was calculated from the following expression

$$\theta_{\text{open,exp}} = \cos^{-1} \left[\frac{\vec{p}'_{\text{s}} \cdot \vec{p}'_{\text{r}}}{|\vec{p}'_{\text{s}}| |\vec{p}'_{\text{r}}|} \right] \quad (64)$$

where \vec{p}'_{s} and \vec{p}'_{r} are the magnetic field corrected scattering and recoil proton momentum vectors.



(a) Energy sum error.



(b) Opening angle error.

[Fig. 42]

Energy sum and opening angle error plots used to identify elastic scattering events during run 271. In both of the above figures, the error is taken to be the difference between the experimental and theoretical values. Both figures are for left events

The opening angle error was calculated from

$$\Delta\theta_{\text{open}} = \theta_{\text{open.exp}} - \theta_{\text{open.theo}} \quad (65)$$

Note that the theoretical opening angle, $\theta_{\text{open,theo}}$, was determined from an equation similar to [Eq. 63], whose only difference was in the replacement of θ_r' with the theoretical recoil proton scattering angle, $\theta_{r,\text{theo}}$. The theoretical angle $\theta_{r,\text{theo}}$ was determined from the following relativistic expression

$$\tan \theta_{r,\text{theo}}' = \frac{E_o [2\eta + \eta^2]^{\frac{1}{2}} \sin\theta_s'}{[2E_o E_{\text{in}} + E_{\text{in}}^2]^{\frac{1}{2}} - E_o [2\eta + \eta^2]^{\frac{1}{2}} \cos\theta_s'} \quad (66a)$$

where

$$\eta = \frac{2E_{\text{in}} \cos^2\theta_s'}{2E_o + E_{\text{in}} \sin^2\theta_s'} \quad (66b)$$

The scattering angles, θ , used in [Eq. 66a] were corrected for the magnetic field deflections. [Fig. 42b] illustrates a typical opening angle error spectrum. The width of the spectrum, which was 1.23° (one σ), was due to the scattered and recoil proton multiple scattering. This can be illustrated by adding in quadrature the individual approximated multiple scattering effects of the scattered and recoil protons, that is

$$[(0.6)^2 + (1.1)^2]^{\frac{1}{2}} = 1.25^\circ. \quad (67)$$

The opening angle centroid shift from zero [Fig. 42b] was found to be equal to the following difference

$$\theta_{\text{open,uncorrected}} - \theta_{\text{open.physical}} \quad (67a)$$

where the first (second) term corresponded to the opening angle as calculated from the scattered and recoil proton scattering angles with no magnetic field corrections (angles at which the scattered and recoil proton detectors were placed on the floor).

IV.4.c Coplanarity Angle

Because in elastic scattering, the three proton (incident, scattered and recoil) momentum vectors are coplanar, the sum of the scattered and recoil proton azimuthal angles minus 180° , their non-coplanarity, should be equal to zero.

The non-coplanarity angle, ϕ_{copl} , was calculated from the following relation

$$\phi_{\text{copl}} = \sin^{-1} \left[\frac{|(\vec{p}'_s \times \vec{p}'_{in}) \times (\vec{p}'_{in} \times \vec{p}'_r)|}{|\vec{p}'_s \times \vec{p}'_{in}| |\vec{p}'_{in} \times \vec{p}'_r|} \right] \quad (68)$$

where \vec{p}'_s , \vec{p}'_r and \vec{p}'_{in} are the scattered, recoil and incident proton momentum vectors, corrected for magnetic field deflection. The sign of ϕ_{copl} was defined positive when the z-component of the triple product was along the positive direction of the experimental coordinate system's z-axis. [Fig. 43a] illustrates a typical non-coplanarity spectrum, whose width was 1.6° (one σ). Because of the manner in which ϕ_{copl} was calculated, the width in the spectrum was attributed to the scattered and recoil proton TOF resolution and to the widths of the various incident, scattered and recoil proton momentum vector component [Eq. 61] distributions.

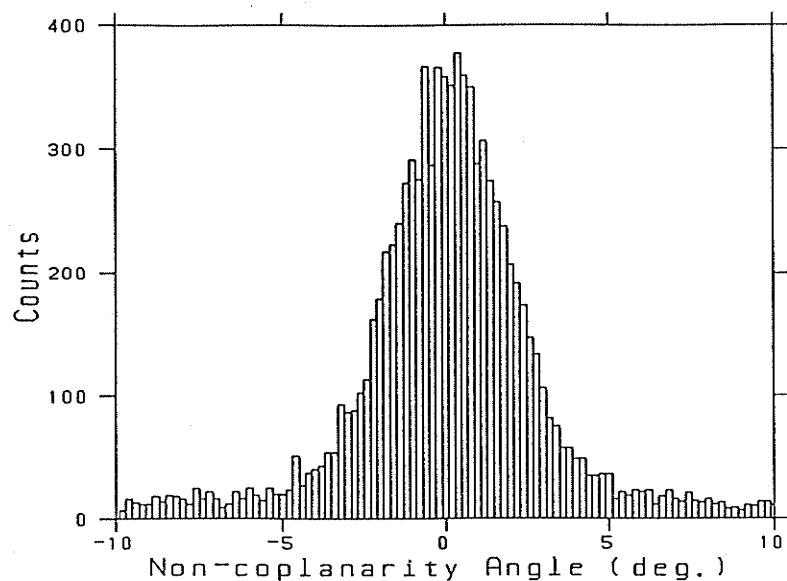
IV.4.d Transverse Momentum Sum

Because momentum is conserved for a given p-p elastic scattering event, the x-component of the transverse momentum (that is, momentum transverse to the incident proton direction) sum must be equal to zero.

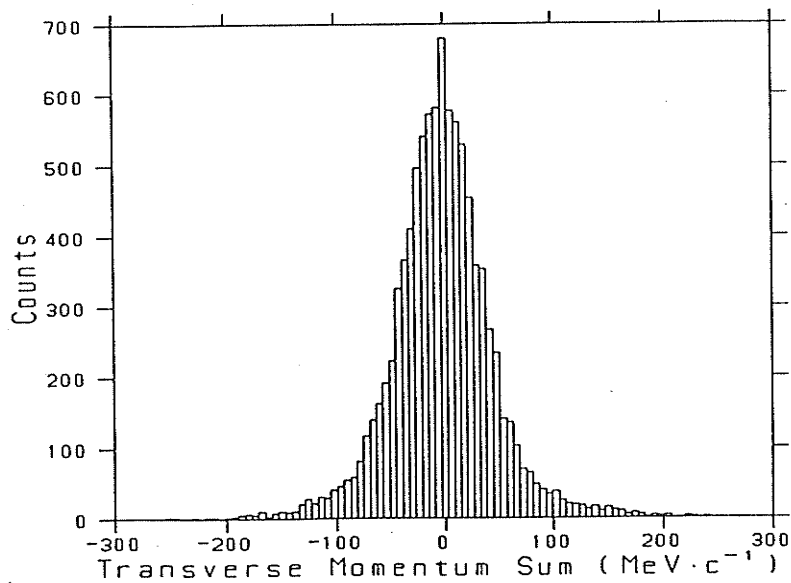
The x-component of the transverse momentum sum (p_x) as calculated from the expression

$$p_x = p_s \sin \theta'_s \cos \phi'_s + p_r \sin \theta'_r \cos \phi'_r + p_{in} \sin \theta'_{in} \cos \phi'_{in} \quad (69)$$

where θ' and ϕ' are the magnetic field corrected scattering and



(a) Non-coplanarity.



(b) x-component of the transverse momentum sum.

[Fig. 43]

Non-coplanarity and transverse momentum sum plots used to identify elastic scattering events, during run 271. Both figures are for left events.

azimuthal angles; the subscripts s, r and in correspond to the scattered, recoil and incident protons. The angles θ'_{in} and ϕ'_{in} were calculated from the net horizontal and vertical deflections the incident proton underwent while traversing the various magnetic fields.

[Fig. 43b] illustrates a typical spectrum for the x-component transverse momentum sum. The width of the spectrum, which was typically 34 MeV/c (one σ), was due to the scattered and recoil protons TOF resolution and to the widths in their $\sin\theta\cos\phi$ distributions. The centroid deviation from zero is due to the scattered and recoil proton centroid deviations in their energy error spectra.

IV.5 Data Representation

The p-p elastic scattering events were selected from the events that had "passed" all of the software cuts, by imposing cuts on the chi-square (χ^2) sum, which was defined as

$$\chi_{\text{sum}}^2 = \sum_{i=1}^4 \chi_i^2 \quad (70)$$

where χ_i^2 is the individual χ^2 of the i'th variable, of the four kinematic constraints to identify the elastic events. The individual χ^2 for the i'th kinematic constraint and j'th event, was determined from

$$\chi_{ij}^2 = \frac{(x_j - \langle x_i \rangle)^2}{\sigma_i^2} \quad (71)$$

where x_j is the measured value for the j'th event, $\langle x_i \rangle$ is the expected value for the i'th constraints distribution and σ_i is the standard deviation in the i'th distribution.

To ensure the consistency of χ_i^2 , and thus χ_{sum}^2 , over the full angular range of the experimental data, σ_i was made independent of scattering angle. This was performed in the following way. The full angular range of the scattered proton detector system, which spanned from 19° to 29° (lab), was binned into 5, 2° bins. The i 'th kinematic distribution was then determined for each bin and the standard deviations for each of the 5 bins were plotted against their corresponding bin centroid angle. The data was then fitted by using a cubic polynomial. By replacing the constant σ_i in [Eq. 71] by the fitted equation of σ_i , which is a function of scattering angle, this removed most if not all of the angular dependence in the variable χ_i^2 , and thus χ_{sum}^2 . The angular correction to σ_i was performed for all the analyzed data for each of the four kinematic constraints. To illustrate the effectiveness of this correction, the centroid in the opening angle χ_i^2 distribution is plotted against the proton scattering angle (for both constant and fitted standard deviations) in [Fig. 44]. The data point in [Fig. 44] at the 20° scattering angle location was not consistent with the other points, due to lack of statistics in the first 2° angular bin.

It should be noted though that with this angular correction, the centroid in the opening angle χ_i^2 distribution is relatively constant in the proton scattering angle region between 21° to 27° (lab), which corresponded to the scattered proton detectors overlap region (to be discussed in section IV.6.a.1).

IV.5.a Detector Counts

The number of elastic events that passed the above software cuts in the left (right) event scattered proton detector system for a given run

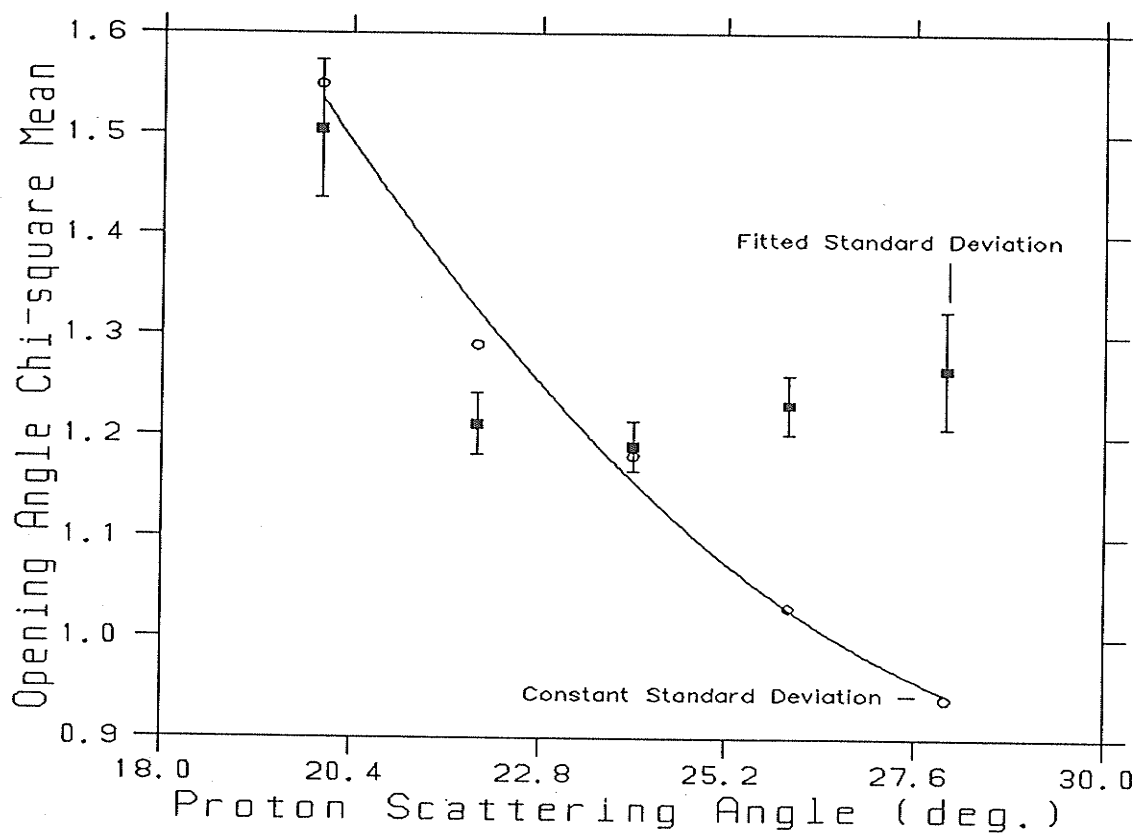


[Fig. 44]

Opening angle χ_1^2 distribution centroids
as a function of proton scattering angle.

is symbolized as L(R). A superscript is attached to illustrate the FST polarization state. That is, for a positive (negative) FST polarization the left event counts would be symbolized as $L^+(L^-)$, a similar notation is used for right events. In the analysis, the detector counts were determined for χ_{sum}^2 cuts of ≤ 10 , ≤ 15 and ≤ 20 .

The detector counts [Ref. 26] were

$$\begin{aligned} L^+ &= nN\Omega_L^+\epsilon_L^+\sigma_0(\theta)[1 + PA_y(\theta)] \\ L^- &= n'N\Omega_L^-\epsilon_L^-\sigma_0(\theta)[1 - PA_y(\theta)] \\ R^+ &= nN\Omega_R^+\epsilon_R^+\sigma_0(\theta)[1 - PA_y(\theta)] \end{aligned} \quad (72)$$

and

$$R^- = n'N\Omega_R^-\epsilon_R^-\sigma_0(\theta)[1 + PA_y(\theta)]$$

where n is the number of incident particles, N is the target thickness (in protons cm^{-2}) and Ω_L , Ω_R , ϵ_L , ϵ_R are the solid angles and total detector efficiencies for the left and right events, $\sigma_0(\theta)$ is the unpolarized cross section, P is the FST polarization and $A_y(\theta)$ is the p-p analyzing power. In [Eq. 72], it is assumed that the incident proton polarization is along the x-axis (and hence contributes nothing to the left-right scattering asymmetry) and the FST polarization along the y-axis.

In the analysis, it was assumed that on the average the target thickness did not vary with runs (time). This was a reasonable assumption since the target, throughout both calibration experiments, was never refilled with beads. The detector counts were corrected for background and total detector efficiency.

IV.5.a.1 Background Corrections

Because there were no separate runs performed to determine the background, it was estimated from the experimental data as follows:

- (a) for a given χ_{sum}^2 cut, eg. $\chi_{\text{sum}}^2 \leq 15$, the opening angle distribution was plotted under the condition $\chi_{\text{sum}}^2 \leq 15$. The number of events within this distribution corresponded to the total number of elastic and background events "observed" for that detector system; and
- (b) the opening angle distribution was once again plotted, but with the conditions $\chi_{\text{sum}}^2 \leq 15$ and $|\phi_{\text{copl}}| > 6^\circ$; determining the number of events within this distribution, gave an estimate on the number of the "observed" events that were due to background. The detector counts were then corrected for background by subtracting the number of background events from the total "observed" events.

The 6° cut in ϕ_{copl} was determined using [Eq. 71], by setting $\chi_{\text{i}}^2 = 15$ and $\sigma_{\text{i}} = 1.6^\circ$ (width of non-coplanarity distribution) then solving for the net deviation from the mean, that is $|x_{\text{j}} - \langle x_{\text{i}} \rangle|$. The systematic error contribution to the FST polarization measurement due to the uncertainty in determining the background fraction, was found for both calibration experiments to be 0.5% (see Appendix C). Typical background fractions during the LH2 (C) calibration experiment were in the order of 2% (5%). The above technique used to obtain the background fraction had originally been verified during the "Test of Change Symmetry Breaking" experiment [Ref. 35].

IV.5.a.2 Total Detector Efficiency Corrections

The background corrected detector counts (N) were corrected for the total detector efficiency (ϵ_T) by performing the following

$$N_{\text{corrected}} = \frac{N_{\text{background corrected}}}{\epsilon_T} \quad (73)$$

In the analysis, ϵ_T was determined when using [Eq. 50].

IV.5.a.3 Effective Runs

Because runs with the same "Bonnie" DAC settings have the incident protons impinging on the same region of the FST sample, the corrected counts of these runs were summed together to improve experimental statistics. These runs were known as effective runs. [Table 27] and [Table 28] indicate the various runs that were combined to create the effective runs. In both of these tables, \bar{P}_{NMR} is the straight average of the various run P_{NMR} values tabulated in [Table 19] and [Table 20]. For the one or two runs with slightly different DAC settings, these runs were combined in the effective tape group that gave the closest agreement to their FST illuminated region.

IV.6 FST Polarization Measurement

IV.6.a Using p-p Elastic Scattering Experiment

IV.6.a.1 Scattering Asymmetry

Using the detector counts [Eq. 72], one can form the following ratio

[Table 27]

Effective Runs Used in LH2 Calibration Experiment

Effective run identification	"Bonnie" DAC setting	P_{NMR}	Combined runs
1	0.02	0.798	223
2	0.07	0.796	222/225/226
3	0.15	0.707	224
4	0.02	-0.800	215/227
5	0.07	-0.777	214
6	0.15	-0.818	213/228/229/230/231

[Table 28]

Effective Runs Used in C Calibration Experiment

Effective run identification	"Bonnie" DAC setting	P_{NMR}	Combined runs
1	0.00	0.818	272/273
2	0.05	0.820	271
3	0.10	0.814	274/275/279
4	0.10 ³⁶	0.813	276/277/278
5	0.00	-0.811	282/287/288/289/290/292
6	0.05	-0.819	281
7	0.10	-0.817	280/286
8	0.10 ³⁶	-0.814	283/284/285/291

³⁶The polarity of "Bonnie" was interchanged.

$$\frac{L^+R^-}{L^-R^+} = \frac{\Omega_L^+ \epsilon_L^+ \Omega_R^- \epsilon_R^- [1 + PA_y(\theta)]^2}{\Omega_L^- \epsilon_L^- \Omega_R^+ \epsilon_R^+ [1 - PA_y(\theta)]^2} \quad (74a)$$

$$\frac{L^-R^+}{L^+R^-} = \frac{\Omega_L^- \epsilon_L^- \Omega_R^+ \epsilon_R^+ [1 - PA_y(\theta)]^2}{\Omega_L^+ \epsilon_L^+ \Omega_R^- \epsilon_R^- [1 + PA_y(\theta)]^2}$$

By expressing the left event detector solid angles and efficiencies as

$$\begin{aligned} \Omega_L^+ &= \Omega_0 (1 + \omega_L^+) \\ \epsilon_L^+ &= \epsilon_0 (1 + S_L^+) \end{aligned} \quad (74b)$$

$$\Omega_L^- = \Omega_0 (1 + \omega_L^-)$$

$$\epsilon_L^- = \epsilon_0 (1 + S_L^-)$$

and using a similar set of equations for the right event detector, one can express [Eq. 74a] as

$$\frac{L^+R^-}{L^-R^+} = \frac{[1 + PA_y(\theta)]^2}{[1 - PA_y(\theta)]^2} \quad (75)$$

when only the zero order terms in [Eq. 74b] are considered.

Solving for P in the above equation, allows one to determine the FST polarization from the left and right event detector counts and p-p analyzing power. From this we find

$$P = \frac{\epsilon}{A_y(\theta)} \quad (76)$$

where

$$\epsilon = \frac{r - 1}{r + 1} \quad (77)$$

with

$$r = \left(\frac{L^+R^-}{L^-R^+} \right)^{\frac{1}{2}} \quad (78)$$

The term ϵ is known as the scattering asymmetry and the method used to deduce it from the detector counts is known as the ratio method. The advantage in using the ratio method to determine ϵ , and in turn P, is that it allows first order cancellation of systematic errors arising from differences in detector efficiencies, solid angle, target thickness, scattering angles and incident beam intensity.

The uncertainty in ϵ due to the statistical fluctuations in the "observed" counts (after background correction), was determined from

$$\Delta\epsilon = \frac{r}{(1+r)^2} \left[\frac{L^+ L^+}{r B} + \frac{R^+ R^+}{r B} + \frac{L^- L^-}{r B} + \frac{R^- R^-}{r B} \right]^{\frac{1}{2}} \quad (79)$$

In the above equation the notation L^+ , L_r^+ and L_B^+ corresponded to the detector background corrected counts, uncorrected "raw" counts and background counts respectively. The variable r in [Eq. 79] was calculated from the background corrected counts.

As a consistency check, the scattering asymmetry was calculated using the normalization method as well. In this method, ϵ was determined from

$$\epsilon = \frac{\epsilon_L + \epsilon_R}{2} \quad (80)$$

where the left event scattering asymmetry (ϵ_L) was defined as

$$\epsilon_L = \frac{L^+ - aL^-}{L^+ + aL^-} \quad (81)$$

with

$$a = \frac{L^+ + R^+}{L^- + R^-} \quad (82)$$

The right event scattering asymmetry (ϵ_R) was defined similarly to ϵ_L , except the left event count rates were interchanged for the right

event counts. Because the normalization method was not as effective as the ratio method in systematic error cancellation, a consistency in the two methods of calculating ϵ , and in turn P , would indicate that most of the errors arising from the detector differences have been correctly accounted for in the analysis.

In this work, only the ratio method data has been presented, although consistency between both methods has been illustrated (see following chapter). When using the ratio method to determine ϵ , only events that fell within the detector overlap region were considered. The overlap region was determined by histogramming the left and right event magnetic field corrected proton scattering angle distributions and then locating the region that was common to both distributions. The overlap region was found to be between 21° and 27° as opposed to the 19° to 29° detector full angular acceptance (this difference in angular range was attributed to the scattered proton magnetic field deflections). Software cuts were imposed on the magnetic field corrected proton scattering angles to ensure that only events within the overlap region were selected to be analysed.

IV.6.a.2 p-p Analyzing Power

The average p-p analyzing power, $\bar{A}_y(\theta)$, was determined from the overlap regions proton scattering angle distribution by calculating the following expression

$$\bar{A}_y(\theta) = \frac{\sum_i A_y(\theta)_i W(\theta)_i}{\sum_i W(\theta)_i} \quad (83)$$

The magnetic field corrected proton scattering angle distribution was binned into $\sim 0.1^\circ$ bins [Fig. 45]. Where i is the bin index, $A_y(\theta)_i$ was the p-p analyzing power for the i 'th bin deduced from the phase shift data and $W(\theta)_i$ is the weighting term, which corresponds to the number of elastic scattering events that fell within the i 'th bin.

The term $A_y(\theta)_i$ was calculated in the following fashion:

- (a) using the phase shift data [Ref. 3], in particular the SP88 energy dependent solutions, a plot of $A_y(\theta)$ versus proton scattering angle was made and the data was fitted using a quadratic polynomial. The analyzing power was determined for the incident proton beam energy of 469 (501) MeV when analyzing the LH2 (C) calibration data; and
- (b) the value of $A_y(\theta)_i$ was then determined from the fit by using the i 'th bins scattering angle centroid.

The uncertainty in the average p-p analyzing power, due to statistical fluctuations in the weighting term, $W(\theta)_i$, was calculated from

$$\overline{\Delta A_y(\theta)} = \frac{1}{\left[\sum_i W(\theta)_i\right]^{\frac{1}{2}}} \left[\frac{\sum_i A_y^2(\theta)_i W(\theta)_i}{\sum_i W(\theta)_i} - (\overline{A_y(\theta)})^2 \right]^{\frac{1}{2}} \quad (84)$$

[Eq. 83] and [Eq. 84] gave the average analyzing power and its statistical error for a given scattered proton detector system. To obtain the average analyzing power and its statistical error over both detectors one uses the expressions:

$$\overline{A_y(\theta)} = \frac{\overline{A_y(\theta)}_L + \overline{A_y(\theta)}_R}{2} \quad (85)$$

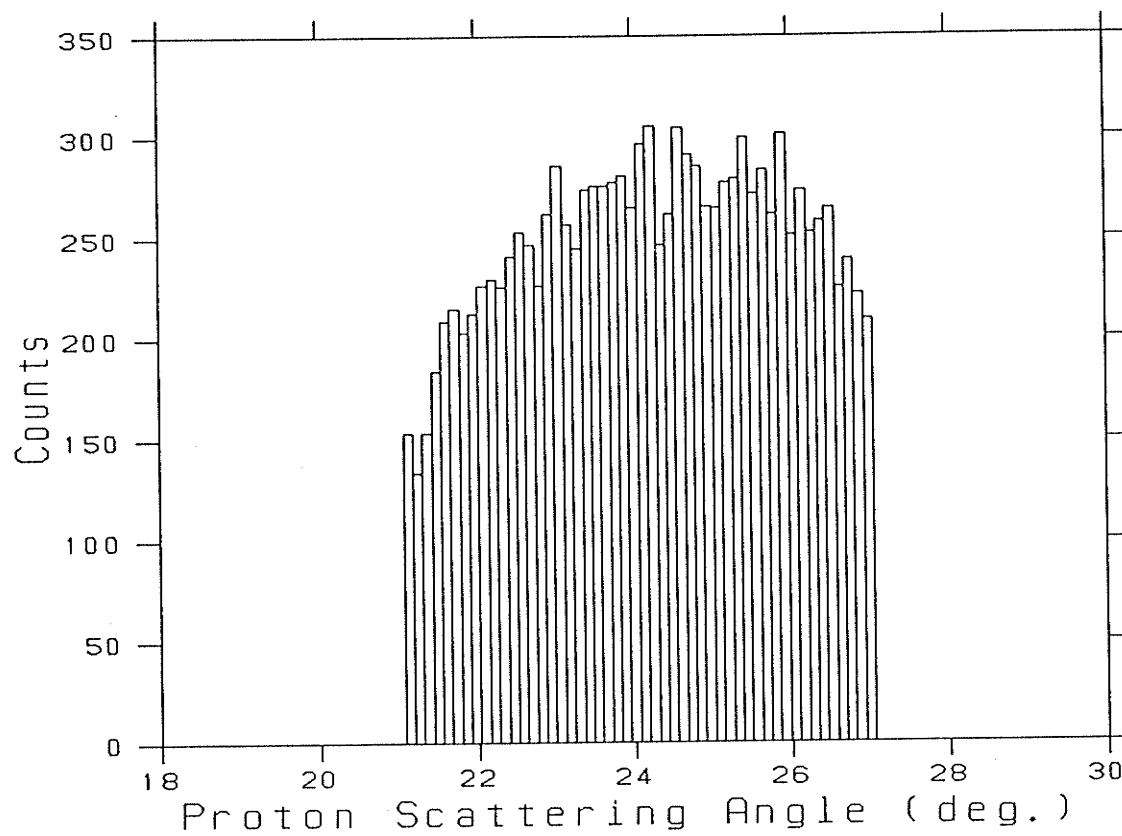


[Fig. 45]

Proton scattering angle distribution
binned to aid in $\bar{A}_y(\theta)$ calculation.

and

$$\Delta A_y(\theta) = \frac{\Delta A_y(\theta)_L + \Delta A_y(\theta)_R}{2} \quad (86)$$

During the LH2 calibration data analysis, the scattering angle distributions used were those of the unpolarized runs. These runs were initially combined into effective runs to improve $\bar{A}_y(\theta)$ statistics. Because the second calibration experiment did not have any unpolarized runs, the effective "unpolarized" distributions were created by combining two runs of opposite FST polarization. Particular care was made to ensure that both of these runs had the same number of events passing the software cuts. Effective runs were also made. The systematic error contribution to the FST polarization measurement due to the uncertainty in the analyzing power deduced from the phase shift data, $A_y(\theta)_i$ [Eq. 83], was calculated to be 1.47 (1.40)% (see Appendix C) for the LH2 (C) calibration results.

IV.6.a.3 FST Polarization

The experimental measurement of the FST polarization was made from [Eq. 76]

$$P = \frac{\epsilon}{\bar{A}_y(\theta)}$$

where ϵ is the calculated scattering asymmetry and $\bar{A}_y(\theta)$ the average analyzing power over both scattered proton detectors. The statistical uncertainty in P was determined from

$$\Delta P = P \left[\left(\frac{\Delta \epsilon}{\epsilon} \right)^2 + \left(\frac{\Delta \bar{A}_y(\theta)}{\bar{A}_y(\theta)} \right)^2 \right]^{1/2} \quad (87)$$

The target polarization as calculated above corresponds to the average target polarization for a given run. Because in reality the target polarization during a run was exponentially decaying in time [Eq. 6a], the target polarization for a given run as determined from the NMR system was corrected for this decay [see following section].

The systematic error contribution to the FST polarization measurement due to the presence of various extraneous beam and FST polarization components was calculated to be 0.56 (0.28)% for the LH2 (C) results (see Appendix C). The systematic error contribution due to differences in effective run polarizations was negligible (see Appendix C). The absolute error in P was determined by adding the statistical and total systematic [Table 33] errors in quadrature.

IV.6.b Using the NMR System

The FST polarization was measured at the start (P_s) and end (P_e) of a given data collection period. The time (t') between polarization measurements was also known. The FST polarization at some time (t) from the P_s measurement was determined using [Eq. 6a] which was

$$P_{\text{NMR}}(t) = P_s e^{-\frac{t}{\tau}}$$

The time decay constant, τ , of the FST polarization in the above equation was calculated from

$$\tau = \frac{t'}{\ln(R)} \quad (88)$$

where

$$R = \frac{P_s}{P_e} \quad (89)$$

Between the polarization measurements P_s and P_e , the data may have been collected (stored) on several magnetic tapes (runs). The average FST polarization for a given run was then determined from

$$\bar{P}_{\text{NMR}} = \frac{P(t_2) - P(t_1)}{\ln(R')} \quad (90)$$

where

$$R' = \frac{P(t_2)}{P(t_1)} \quad (91)$$

The run had started at a time t_1 from the P_s measurement and ended at time t_2 . The \bar{P}_{NMR} values tabulated in [Table 19] and [Table 20] were calculated using [Eq. 90] and [Eq. 91].

The error in the individual NMR polarization measurement was estimated to be $\pm 2\%$. This is based upon the distribution of six thermal equilibrium calibrations which showed a standard deviation of 2%. The error in the enhancement factor [see section II.5.a] was 10 times smaller and can be neglected.

IV.7 FST Polarization Distribution

The FST sample was segmented into three horizontal strips [Fig. 46] of equal height. Software cuts were imposed on the FST y-coordinate image to isolate the elastic p-p scattering events that had taken place within a given bin. The experimental data was calculated for χ_{sum}^2 cuts of ≤ 10 , ≤ 15 and ≤ 20 , as well as for various FST bins and effective runs, which were characterized by their common "Bonnie" DAC settings. The FST polarizations [see Appendix D] were calculated from

$$P(i, j, k) = \frac{\epsilon(i, j, k)}{A_y(i, j, k)} \quad (92)$$

when using [Eq. 76], whose statistical uncertainty can be calculated when using [Eq. 87]. The index definitions [see Appendix D] were

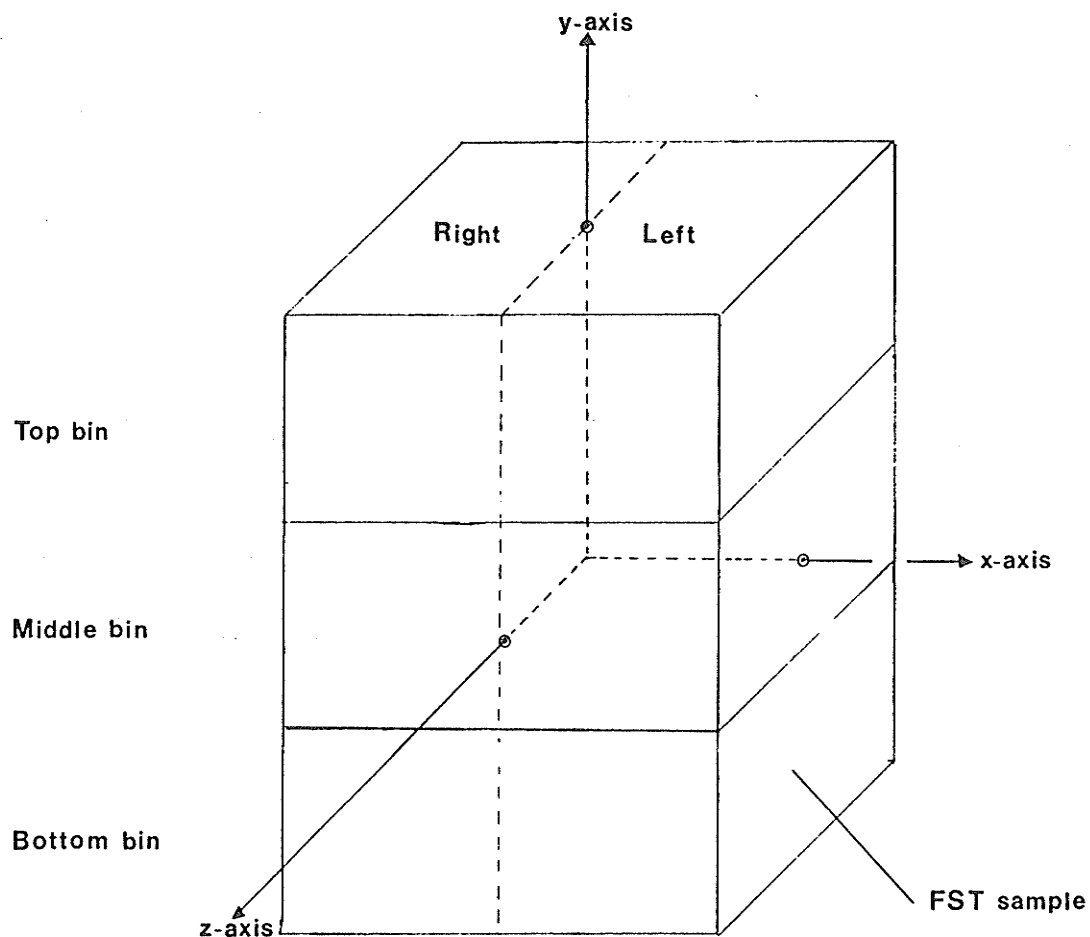


[Fig. 46]

FST sample segmentation. The dimensions of the target sample were 3.5 cm long (along z-axis), 2 cm wide and 5 cm high. The incident beam direction was along the positive z-axis. The diagram is not to scale.

$$\begin{aligned}
 i &= \text{FST bin (1, 2, 3)} \\
 j &= \text{"Bonnie" DAC setting (1, 2, 3 or 4)} \\
 k &= \chi^2_{\text{sum}} \leq \text{cut (1, 2, 3)}.
 \end{aligned}
 \tag{93}$$

The FST polarization as a function of bin was then calculated from the $P(i,j,k)$ measurements from the relation

$$P(i,k) = \frac{\sum_{j=1}^{3 \text{ or } 4} \frac{P(i,j,k)}{[\Delta P(i,j,k)]^2}}{\sum_{j=1}^{3 \text{ or } 4} \frac{1}{[\Delta P(i,j,k)]^2}}
 \tag{94}$$

and the statistical uncertainty in $P(i,k)$ was calculated from

$$\Delta P(i,k) = \left[\frac{1}{\sum_{j=1}^{3 \text{ or } 4} 1/[\Delta P(i,j,k)]^2} \right]^{\frac{1}{2}}
 \tag{95}$$

The sum of j goes from 1 to 3(4) when the LH2 (C) effective runs were analyzed. The FST polarization distribution was also determined when using 6 bins. The 6 bin setup was achieved by vertically bisecting the existing three horizontal segments as illustrated in [Fig. 46]. Because the polarization for the left and right segments of a given horizontal bin was found to be within the uncertainty in the polarization measurement of the horizontal bin (before bisection), only the 3 bin arrangement was used to determine the FST polarization measurement.

[Table 29] summarizes the FST polarization distribution when using a 3 and 6 bin arrangement. The data in [Table 29] were deduced from the zero "Bonnie" effective run data, that had been collected during the second calibration experiment.

[Table 29]

FST Polarization Distribution
Using Three and Six Bin Arrangements

bin	3 bin arrangement		6 bin arrangement	
	FST polarization ³⁷		bin ³⁸	FST polarization ³⁷
Top	0.782 \pm 0.024		Top left	0.799 \pm 0.039
			Top right	0.769 \pm 0.032
Middle	0.728 \pm 0.015		Middle left	0.739 \pm 0.023
			Middle right	0.721 \pm 0.020
Bottom	0.749 \pm 0.024		Bottom left	0.730 \pm 0.037
			Bottom right	0.769 \pm 0.032

³⁷The quoted uncertainties are purely statistical.

³⁸The left-right bin orientation is with respect to an observer looking downstream from the FST.

The dimensions of the bins that were ultimately used were 16.7 mm high by 20 mm wide by 35 mm thick. The smallest bins that could have been used (calculated by projecting the fourth DLC x- and y-coordinate resolutions (typically ± 1 mm) from the TOF stop scintillator position to the FST center and rotating the projected values into the FST reference frame) had the dimensions of 15.6 mm high by 14.2 mm wide by 35 mm thick.

IV.8 Average FST Polarization

The average FST polarization was calculated from the FST polarization distribution using the expression

$$P(k) = \frac{\sum_{i=1}^3 P(i,k)}{3} \quad (96)$$

and the associated statistical uncertainty was calculated from

$$\Delta P(k) = \frac{1}{3} \left[\sum_{i=1}^3 \Delta P(i,k)^2 \right]^{1/2} \quad (97)$$

IV.9 NMR Polarization Calibration

The calibration constant (μ) relates the measurements of target polarization made by the p-p elastic scattering and NMR methods; and was defined as:

$$\mu = \frac{P_{\text{scatter}}}{P_{\text{NMR}}} \quad (98)$$

To determine μ from the experimental $P(i,j,k)$ data (see Appendix D), the following relation was used

$$\mu(i,j,k) = \frac{P(i,j,k)}{\bar{P}_{\text{NMR}}(j)} \quad (99)$$

where

$$\bar{P}_{\text{NMR}}(j) = \frac{|\bar{P}_{\text{NMR}}^+(j)| + |\bar{P}_{\text{NMR}}^-(j)|}{2} \quad (100)$$

The variables $\bar{P}_{\text{NMR}}^+(j)$ and $\bar{P}_{\text{NMR}}^-(j)$ are the NMR polarization measurements, as tabulated in [Table 27] or [Table 28], for the two effective runs that were used to calculate $\epsilon(i,j,k)$ for the j'th "Bonnie" DAC setting. The statistical uncertainty in μ was calculated from

$$\Delta\mu(i,j,k) = \mu(i,j,k) \left[\left(\frac{\Delta\epsilon(i,j,k)}{\epsilon(i,j,k)} \right)^2 + \left(\frac{\Delta A_y(i,j,k)}{A_y(i,j,k)} \right)^2 + \left(\frac{\Delta \bar{P}_{\text{NMR}}(j)}{\bar{P}_{\text{NMR}}(j)} \right)^2 \right]^{\frac{1}{2}} \quad (101)$$

as opposed to [Eq. 87] for the FST polarization measurement. The experimental $\mu(i,j,k)$ data have also been tabulated (see Appendix D). The average calibration constant was calculated from the calibration constants distribution in the same manner as indicated in [Eq. 96] and [Eq. 97].

CHAPTER V

RESULTS AND DISCUSSION

Before the average NMR calibration constant was determined from its distribution throughout the FST sample, it was necessary to determine the FST polarization distribution. The FST polarization distribution was obtained by segmenting (via software) the FST sample into several bins of equal size and then determining the FST polarization for the sample region within each bin. The FST polarization distribution was deduced from 3 horizontal strips of equal height [Fig. 46], identified as the top, middle and bottom bin. When a 6 bin arrangement (vertically bisecting the existing 3 horizontal bins) was used to deduce the FST polarization distribution, the left-right difference in the FST polarization for the top, middle and bottom bins was typically 0.03, 0.02 and 0.04, respectively. Because the left-right difference in the FST polarization for a given horizontal bin was smaller than the error bar in the FST polarization measurement for the entire horizontal bin [Table 29], this effect was not significant enough to be accounted for.

The FST polarization and NMR calibration constant distributions over the three FST bins, as deduced from the p-p elastic scattering asymmetries, are summarized in [Table 30] and [Table 31]. It is seen from [Table 30] that the FST polarization decreases from top to bottom of the target during both calibration experiments. A possible explanation is the following: if we assume the FST sample polarization to be of uniform distribution when it was initially polarized, then the observed FST polarization distribution can be predicted when the

[Table 30]

FST Polarization Distribution

FST bin	FST polarization ³⁹	
	LH2 runs	C runs
for $\chi^2_{\text{sum}} \leq 10$ data		
Top	0.808 \pm 0.015	0.792 \pm 0.008
Middle	0.768 \pm 0.010	0.762 \pm 0.006
Bottom	0.734 \pm 0.015	0.763 \pm 0.008
for $\chi^2_{\text{sum}} \leq 15$ data		
Top	0.818 \pm 0.014	0.796 \pm 0.008
Middle	0.766 \pm 0.009	0.768 \pm 0.006
Bottom	0.728 \pm 0.014	0.766 \pm 0.008
for $\chi^2_{\text{sum}} \leq 20$ data		
Top	0.805 \pm 0.014	0.789 \pm 0.008
Middle	0.762 \pm 0.009	0.768 \pm 0.006
Bottom	0.728 \pm 0.014	0.761 \pm 0.008

³⁹The quoted uncertainties are purely statistical.

[Table 31]

NMR Calibration Constant Distribution

FST bin	NMR Calibration Constant ⁴⁰	
	LH2 runs	C runs
for $\chi^2_{\text{sum}} \leq 10$ data		
Top	1.009 \pm 0.019	0.971 \pm 0.010
Middle	0.961 \pm 0.012	0.935 \pm 0.007
Bottom	0.922 \pm 0.019	0.937 \pm 0.010
for $\chi^2_{\text{sum}} \leq 15$ data		
Top	1.023 \pm 0.018	0.976 \pm 0.010
Middle	0.959 \pm 0.012	0.942 \pm 0.007
Bottom	0.915 \pm 0.018	0.940 \pm 0.009
for $\chi^2_{\text{sum}} \leq 20$ data		
Top	1.006 \pm 0.018	0.967 \pm 0.010
Middle	0.955 \pm 0.011	0.942 \pm 0.007
Bottom	0.914 \pm 0.018	0.934 \pm 0.009

⁴⁰The quoted uncertainties are purely statistical.

polarization decay constant for each of the 3 bins was different and decreased from top to bottom. The only FST parameters that could cause the polarization decay constant [Eq. 6b] to vary within each bin would be changes in the sample temperature and in the holding field. Consider the sample temperature possibility first. Because the polarization decay constant decreases from top to bottom [Table 31], then from [Eq. 6b] it would indicate that the sample must be cooler at the top than at the bottom. The $\chi_{\text{sum}}^2 \leq 20$ data in [Table 30], indicate a FST polarization difference of 0.077 and 0.028 from the top to the bottom bin, for the LH2 and C runs respectively. This corresponded to a temperature difference between the top and bottom bins of 19 mK and 10 mK, respectively. The temperature difference (ΔT) was calculated from the observed FST polarization difference (ΔP), using

$$\Delta T = \frac{\tau T}{6tP} \Delta P \quad (102)$$

and [Table 32], where τ is the average polarization decay constant deduced from the NMR measurements, t is the total data collection period, T is the sample temperature and P the average FST polarization deduced from [Table 30]. [Eq. 102] was derived from [Eq. 6a] and [Eq. 6b]. Because there was only one mixing chamber thermometer [Fig. 7] located at the bottom of the FST sample, it was not possible to verify this conjecture for the observed FST polarization distribution. Consider now the holding field possibility. Since the polarization decay constant decreases from top to bottom, then from [Eq. 6b], it would indicate that the holding field is larger at the top than at the bottom. If once again we employ the $\chi_{\text{sum}}^2 \leq 20$ data in [Table 30], the up-down FST polarization difference of 0.077 (0.028) would correspond to

[Table 32]

FST Experimental Parameters

Item	LH2 runs	C runs
Average FST polarization	0.766	0.755
Top-bottom polarization difference ($\chi_{\text{sum}}^2 \leq 20$ data)	0.077	0.028
Average polarization decay constant	479.3 Hrs.	833.6 Hrs.
Total data collection period	18.7 Hrs.	23.3 Hrs.
Sample temperature	45 mK	45 mK
FST holding field	0.257 T	0.257 T

a holding field difference between the top and bottom bins of 0.16 (0.08) T. The holding field difference (ΔB) was calculated from ΔP , using

$$\Delta B = \frac{\tau B}{4tP} \Delta P \quad (103)$$

and [Table 32], where B is the FST holding field. [Eq. 103] in turn was derived from [Eq. 6a] and [Eq. 6b]. Prior to the "Test of Charge Symmetry Breaking" experiment, various holding field maps were made above and below the central plane of the target cell. From these field maps the holding field change with vertical distance (at the target center) was found to be $0.006 \text{ T} \cdot \text{cm}^{-1}$. The above calculated 0.16 T and 0.08 T holding field differences over the full 5 cm height of the target, corresponded to change of $0.032 \text{ T} \cdot \text{cm}^{-1}$ and $0.016 \text{ T} \cdot \text{cm}^{-1}$ for the LH2 and C runs respectively. Because the observed holding field variation with vertical distance (as calculated from field maps) is much smaller than that predicted, it would be reasonable to assume that the observed polarization difference from the top of the target to the bottom is not due to a holding field variation between the top and bottom bin.

Another explanation for the observed polarization distribution would be to have the sample temperature constant throughout the FST sample, and thus the polarization decay constant, and have the FST polarization distribution to be such that the bin polarization decreased from top to bottom when the sample was initially polarized. This effect is somewhat justified from the fact that the microwave photons that are used to initially polarize the FST sample via the dynamic nuclear polarization method enter the FST sample from the top [Fig. 7]. Thus,

the top bin may have been polarized more than the bottom bin due to photon attenuation within the FST sample. It is not possible to distinguish whether the resulting FST polarization distribution is due to the temperature variation throughout the FST sample or the initial microwave photon attenuation within the sample, or a combination of both effects.

The NMR calibration constant (μ) was defined as

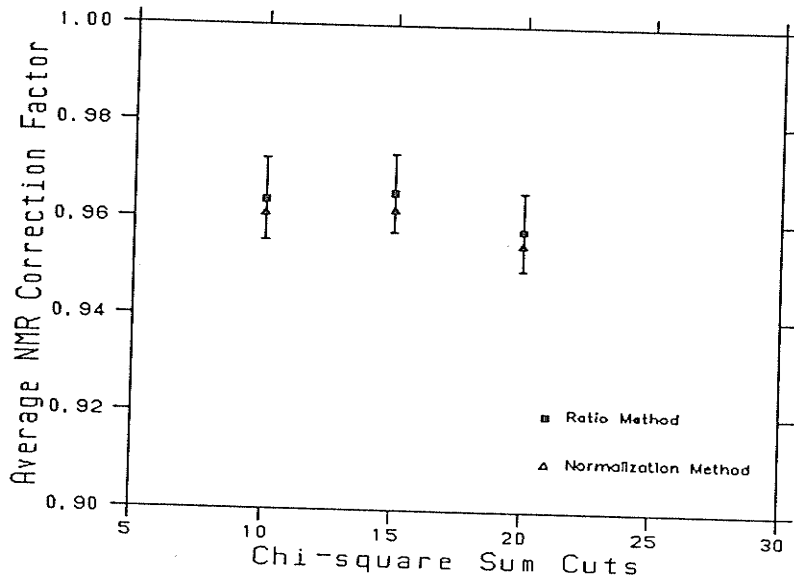
$$\mu = \frac{P_{\text{scatter}}}{P_{\text{NMR}}} \quad (104)$$

where P_{scatter} and P_{NMR} are the FST polarizations deduced from p-p elastic scattering and the NMR system. It should be noted that μ was observed [Table 31] to be near unity at the top of the sample, not in the middle where the NMR coil is physically situated.

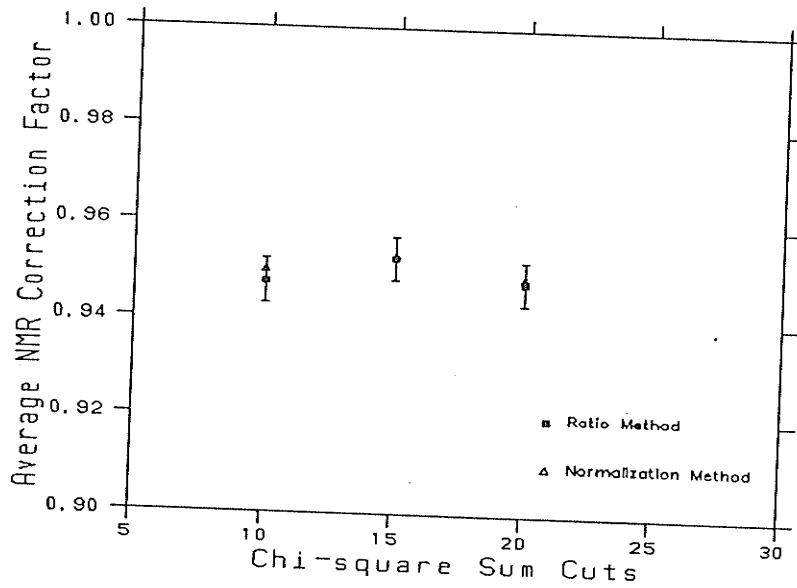
The average NMR calibration constant over the entire FST sample was calculated in a manner as indicated in [section IV. 9]. [Fig. 47] illustrates the experimental results with their associated statistical error bars. Agreement between the average NMR calibration constants calculated from the asymmetries using the ratio and normalization methods indicates that systematic errors arising from differences in detector solid angles, efficiencies, target thickness, scattering angle and incident beam current have been correctly accounted for. [Fig. 48] illustrates the various contributing effects the background and detector efficiency corrections to the detector count rates had on the final results.

The systematic error in the average NMR calibration constant ($\bar{\mu}$) was evaluated from

$$\Delta\bar{\mu} = f_A \bar{\mu} \quad (105)$$



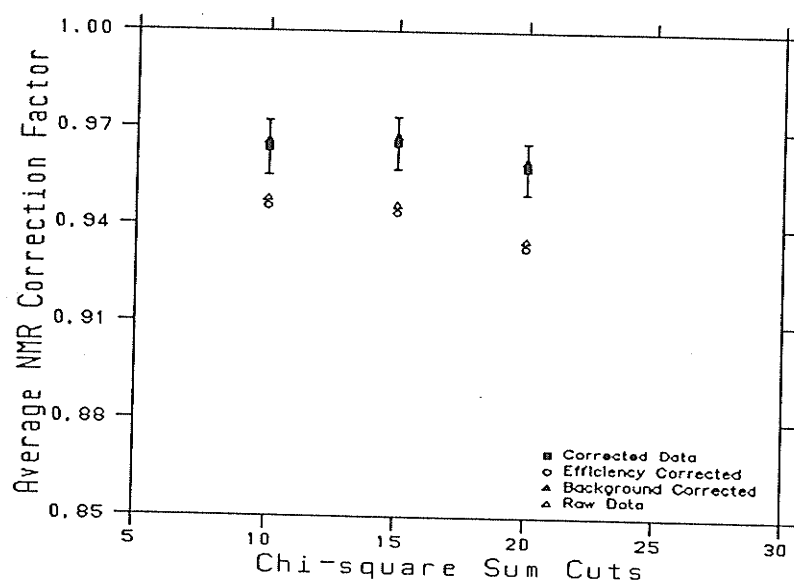
(a) For LH2 runs.



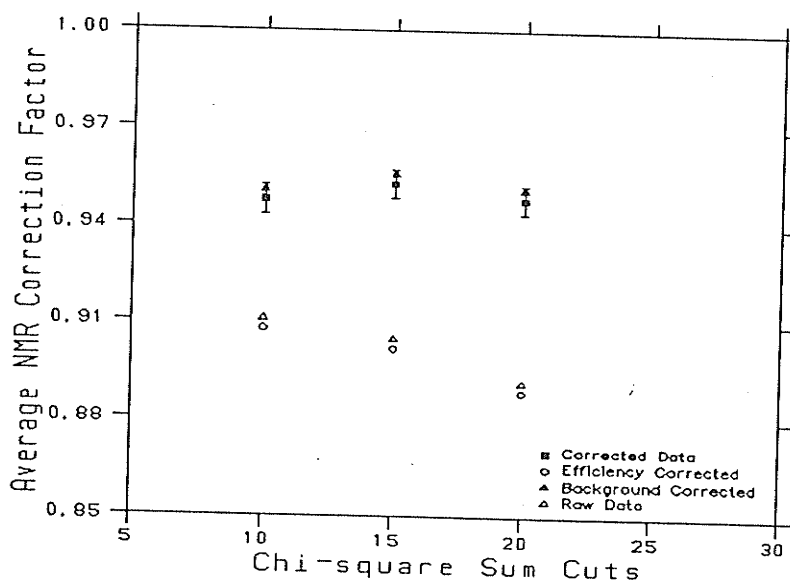
(b) For C runs.

[Fig. 47]

Average NMR calibration constant results using the ratio and normalization methods of determining the scattering asymmetry.



(a) For LH2 runs.



(b) For C runs.

[Fig. 48]

Average NMR calibration constant results when corrected for background and detector efficiency.

where the scaler f_A is assigned the value 0.0216 (0.0209) when analyzing the LH2 (C) data. The scaler f_A was determined by adding the individual systematic error contributions [see Appendix C] in quadrature [Table 33] excluding the p-p analyzing power systematic error contribution. The latter was determined from the phase shift analysis results [Ref. 3] to the existing p-p data base, and was kept separate from the other 8 due to the method used to estimate it [see Appendix C]. The systematic error in the average NMR calibration constant due to this effect alone was calculated using [Eq. 105] but f_A was now assigned the value 0.0147(0.0140) [Table 33] when analyzing the LH2 (C) data. [Table 34] summarizes the average NMR calibration constant results which have assigned to them three uncertainties. The first of these is due to statistical fluctuations in the data, the second is due to the first 8 systematic error contributions as tabulated in [Table 33] and the third is due to the systematic error of the p-p analyzing power deduced from the phase shift analysis.

After the data analysis, the primary proton beam energy loss from cyclotron exit to FST center [see section IV.2.a.2] was re-calculated and it was found, that the LH2 run beam energy at the center of the FST should have been 467.6 MeV and not 469.0 MeV [Table 35] as previously calculated. To compensate for this change in beam energy, the LH2 results in [Table 34] were re-calculated. This involved the scaling of the observed analyzing power data, that is

$$A_{y_{\text{new}}}(\theta) = A_{y_{\text{obs}}}(\theta) \cdot f_B \quad (106)$$

where

[Table 33]

Systematic Error Considerations

Contributing effects	(ΔP/P)	
	LH2 runs	C runs
Error in P due to error in incident proton beam energy	0.0021	0.0011
Error in P due to error in determining the detector physical angle	0.0022	0.0022
Error in P due to wrong corrections for deflections in holding field	0.0002	0.0002
Error in P due to different effective run FST polarizations	negligible	negligible
Error in P _{NMR} due to reproducibility of the NMR system	0.0200	0.0200
Error in P due to error in determining the background fraction	0.0049	0.0047
Error in P due to incorrect spin precession of superconducting solenoid	negligible	negligible
Error in P due to the presence of various beam and FST polarization components	0.0056	0.0028
Adding the above in quadrature	0.0216	0.0209
Error in P due to the error in the analyzing power	0.0147	0.0140

[Table 34]

Average NMR Calibration Constant Results

$\chi^2_{\text{sum}} \leq \text{cut}$	LH2 runs	C runs
10	$0.9639 \pm 0.0084 (+0.0208) (\pm 0.0142)$	$0.9477 \pm 0.0046 (+0.0198) (\pm 0.0133)$
15	$0.9654 \pm 0.0081 (+0.0208) (\pm 0.0142)$	$0.9527 \pm 0.0045 (+0.0199) (\pm 0.0133)$
20	$0.9579 \pm 0.0080 (+0.0207) (\pm 0.0141)$	$0.9480 \pm 0.0044 (+0.0198) (\pm 0.0133)$
Straight		
average of	$0.9624 \pm 0.0082 (+0.0208) (\pm 0.0142)$	$0.9495 \pm 0.0045 (+0.0198) (\pm 0.0133)$
above results		
Weighted mean of above		
results using the statistical		$0.952 \pm 0.004 (+0.020) (\pm 0.014)$
errors as weighting		

[Table 35]

LH2 Run Primary Proton Beam Energy Losses

	Previous Values (MeV)	Recalculated Values (MeV)
At cyclotron exit	497.0	497.0
At BEM kapton foil exit	497.0	497.0
At center of secondary beam production target	493.0	493.0
After 9° (lab) scattering at center of secondary beam production target	477.9	477.9
At secondary beam production target exit	476.8	473.8
After passing through 317.13 cm of air	475.8	472.8
At TOF start scintillator exit	475.6	472.6
After passing through 166.28 cm of air	475.1	472.0
At horizontal drift chamber exit	475.1	471.7
After passing through 124.22 cm of air	474.7	471.6
At horizontal drift chamber exit	474.6	471.5
After passing through 9.75 cm of air	474.6	471.4
At TOF stop scintillator exit	474.4	471.3
After passing through 21.55 cm of air	474.3	471.2
At FST center	469.0	467.6

$$\begin{aligned}
 f_B &= \frac{A_y(24^\circ)}{467.6} \\
 &= \frac{A_y(24^\circ)}{469} \\
 &= 0.9988
 \end{aligned}
 \tag{107}$$

and recalculating the NMR calibration constant data from the observed scattering asymmetries. The scaler f_B was determined from Arndt's phase shift analysis [Ref. 3] SP88 energy dependent solutions. The new LH2 run average NMR calibration constant result, after the above correction, was found to be $0.9636 \pm 0.0082(\pm .0208)(\pm .0142)$. The new weighted mean of the average NMR calibration constants of both experiments was $0.953 \pm 0.004(\pm 0.020)(\pm 0.014)$, which had an absolute error of

$$\frac{100 \times [(.004)^2 + (.020)^2 + (.014)^2]^{1/2}}{0.953} = 2.6\% \tag{108}$$

As a finishing note, during the "Test of Charge Symmetry Breaking" experiment an average NMR calibration constant value of 0.961 ± 0.024 (± 0.027) [Ref. 1] was obtained. The first and second uncertainties were due to the statistical and systematic errors, respectively. The NMR calibration constant (R) was calculated from

$$R = \frac{P_{\text{scatter}}}{P_{\text{NMR}}} \tag{109}$$

where P_{NMR} is the NMR target polarization measurement and P_{scatter} is the FST polarization measurement determined from an experiment that used a secondary beam of neutrons to impinge upon the FST's protons.

P_{scatter} was determined from the neutron beam polarization (P_n), using

$$P_{\text{scatter}} = P_n \cdot \left(\frac{d\epsilon_p/d\theta}{d\epsilon_n/d\theta} \right) \tag{110}$$

In the above equation, ϵ_n (ϵ_p) is the observed scattering asymmetry when the neutron beam is polarized (unpolarized) and FST is unpolarized (polarized); θ was the proton scattering angle, that was observed over the angular range of 27° to 37° (lab.).

When a comparison is made between the average NMR calibration constant found here 0.953 ± 0.025 (absolute), and that of the charge symmetry experiment 0.961 ± 0.036 (absolute) it is seen that they agree within their associated error bars. The present result, is taken to be a better representation of the true average NMR calibration constant, due to its smaller error bar and the fact that it was determined from the NMR calibration constant distribution throughout the FST sample.

V.1 Conclusion

The average NMR calibration constant was determined from its distribution throughout the FST sample and has been measured with an accuracy of $\pm 2.6\%$, using p-p elastic scattering. Prior to this measurement the NMR calibration constant was known to $\pm 3.6\%$ [Ref. 1]. The NMR calibration constant distribution for a 3 horizontal bin arrangement, indicated that the top bin of the sample obtained the highest value, and the middle and bottom bins were consecutively lower.

The incorporation of the results of this work into the $A_{yy}(\theta)$ experiment's analysis, allowed the measurement of $A_{yy}(\theta)$ and $A_y(\theta)$ [see chapter I] to be determined to an absolute accuracy of ± 0.03 . The resulting new data had a great impact on the phase shift parametrization of the $I = 0$ scattering amplitudes [Ref. 2].

REFERENCES

- [1] R. Abegg et al., Nucl. Instr. and Meth., **A254**, 469(1987).
- [2] D. Bandyopadhyay, Spin Correlation Parameter and Analyzing Power in n-p Elastic Scattering at Intermediate Energies, Ph.D. thesis, University of Manitoba, 1988.
- [3] R.A. Ardnt, Scattering Analysis Interaction Dial-in Program, SAID, Spring 1988 solutions.
- [4] T.J. Schmutge and C.D. Jeffries, Phys. Rev., **A138**, 1785(1965).
- [5] W. Gorn and P. Robish, Proc. 2nd Int. Conf. on Polarized Targets, Berkeley, 271 (1971).
- [6] D. Hill et al., Phys. Letters, **23**, 63(1966).
- [7] H. London, G.R. Clarke and E. Mendoza, Phys. Rev., **128**, 1992(1962).
- [8] W. de Boer and T.O. Niinikoski, Nucl. Instr. and Meth., **114**, 495(1974).
- [9] A. Abragam and M. Goldman, Rep. Prog. Phys., **41**, 395(1978).
- [10] P.P.J. Delheij, D.C. Healey and G. Wait, Proc. Sixth Int. Symp. on Polar. Pheno., Osaka 1985.
- [11] P.B. Pipes, Experiments with He-3/He-4 Dilution Refrigeration and their Application to Nuclear Magnetic Susceptibility Measurements in Solid He-3, Ph.D. thesis, Stanford University, 1969.
- [12] M.G. Richards and J.M. Homer, Proc. of the 11th Int. Conf. on Low Temp. Phys., 340(1968).
- [13] W.R. Abel, A.C. Anderson, W.C. Black and J.C. Wheatley, Phys., **1**, 337(1965).
- [14] H.D. Cohen and W.M. Fairbank, Proc. of the 10th Int. Conf. on Low Temp. Phys., 350(1967).
- [15] D.O. Edwards, D.F. Brewer, P. Seligman, M. Skertic and M. Yaqub, Phys. Rev. Letters, **15**, 773(1955).
- [16] C. Kittel, Elementary Statistical Physics, 94(1961).
- [17] E.M. Ifft, D.O. Edwards, R.E. Sarwinski and M.M. Skertic, Phys. Rev. Letters, **19**, 831(1967).

- [18] S.R. de Groot, H.A. Tolhoek and W.T. Huiskamp, Alpha-Beta- and Gamma Ray Spectroscopy, 1233 (1965).
- [19] P.P.J. Delheij, D.C. Healey and G.D. Wait, Nucl. Inst. and Meth., **A264**, 186 (1988).
- [20] M. Krumpolc and J. Rocek, J. Am. Chem. Soc., **101**, 3206 (1979).
- [21] P.P.J. Dehlheij, D.C. Healey and G.D. Wait, TRIUMF Technical Note, Target Polarizations for the Test of Charge Symmetry, 1985.
- [22] J. Ball et al., Proc. 4th Int. Workshop on Pol. Target Materials and Techniques, 112 (1984).
- [23] G.E. Pake, Am. J. Phys., **18**, 438 (1950).
- [24] R. Abegg et al., Nucl. Inst. and Meth., **A234**, 11 (1985).
- [25] L.G. Greeniaus and J. Soukup, Polarimeter-Beam Energy Monitor, Internal TRIUMF Report TRI-DNA-1 (1981).
- [26] G.G. Ohlsen, Rep. Prog. Phys., **35**, 717 (1972).
- [27] TRIUMF kinematic handbook. Section VII-1, (1989).
- [28] P. Hillman, G.H. Stafford and C. Whitehead, Nuovo Cimento, **4**, 67 (1956).
- [29] J.S.C. McKee, 7.0 Tesla Superconducting Solenoid and 2 Inch Room Temp. Bore - Horizontal Cryostat System, University of Manitoba, (1980).
- [30] K. Chantziantoniou, Operation Manual for Superconducting Solenoid, TRIUMF Group Report, (1987).
- [31] R.C. Fernow, Introduction to Experimental Particle Physics, (1986).
- [32] D. Bandyopadhyay, MRS Front End Wire Chambers, TRIUMF Group Report, (1986).
- [33] R. Abegg et al., Nucl. Inst. and Meth., **A234**, 20 (1985).
- [34] P. Poffenberger, A Pedestrian's Guide to the CSB Delay Line Chambers, Internal TRIUMF Report TRI-DN-84-30 (1984).
- [35] R.C. Tkachuk, Search For Charge Symmetry Breaking in Neutron-Proton Elastic Scattering at 477 MeV, Ph.D. Thesis, University of Alberta, 1987.

APPENDIX A

FROZEN SPIN TARGET POLARIZATION UNCERTAINTY REQUIREMENT

The n-p spin correlation parameter $A_{yy}(\theta)$ can be shown to be of the form:

$$A_{yy}(\theta) = \frac{1}{P_T P_B} \left(\frac{\beta-1}{\beta+1} \right) \quad (A1)$$

with

$$\beta = \left[\frac{L_{++} + L_{--}}{L_{+-} + L_{-+}} \cdot \frac{R_{++} + R_{--}}{R_{+-} + R_{-+}} \right]^{1/2} \quad (A2)$$

where L_{++} and R_{++} are the counts in the left and right detectors, the subscripts indicate the beam (first) and target (second) polarization directions; P_T and P_B are the target and beam polarizations.

[Eq. A1] can be simplified to

$$A_{yy}(\theta) = \frac{\epsilon}{P_T P_B} \quad (A3)$$

when ϵ is defined as

$$\epsilon = \frac{\beta - 1}{\beta + 1} \quad (A4)$$

The n-p spin correlation parameter uncertainty can be determined from [Eq. A3] and is written as

$$\frac{\sigma_{A_{yy}}}{A_{yy}} = \left[\frac{\sigma_{\epsilon}^2}{\epsilon^2} + \frac{\sigma_{P_B}^2}{P_B^2} + \frac{\sigma_{P_T}^2}{P_T^2} \right]^{1/2} \quad (A5)$$

where σ_{P_T} , $\sigma_{A_{yy}}$, σ_{P_B} and σ_{ϵ} are the uncertainties in the variables P_T , $A_{yy}(\theta)$, P_B and ϵ , respectively. It should be noted that [Eq. A5] assumes that P_B and P_T or σ_{P_B} and σ_{P_T} are not correlated.

The beam polarization can be determined to less than $\pm 2\%$, assuming that the spin transfer coefficient r_t is known, so

$$\frac{\sigma_{P_B}}{P_B} < 0.02 \quad (\text{A6})$$

and assuming the systematic errors in the observed scattering asymmetry (ϵ) are under control then

$$\frac{\sigma_{\epsilon}}{\epsilon} < 0.01 \quad (\text{A7})$$

If the target polarization can be determined to at most $\pm 2\%$, that is

$$\frac{\sigma_{P_T}}{P_T} < 0.02 \quad (\text{A8})$$

then by substituting [Eq. A6], [Eq. A7] and [Eq. A8] into [Eq. A5] it can be shown that

$$\frac{\sigma_{A_{yy}}}{A_{yy}} < 0.03 \quad (\text{A9})$$

Since $|A_{yy}| \leq 0.5$ then from [Eq. A9]

$$\sigma_{A_{yy}} < 0.03 \quad (\text{A10})$$

It is seen then from the above derivation that a target polarization with absolute accuracy of less than $\pm 2\%$ is necessary to achieve an absolute accuracy of ± 0.03 in the n-p spin correlation parameter.

APPENDIX B

PROTON ENSEMBLE POLARIZATION AT THERMAL EQUILIBRIUM

Consider an ensemble of independent particles each having the same spin S . The Hamiltonian for the interaction between each particle and the static external magnetic field $\vec{B} = B\hat{k}$, is given as

$$H = -M_z B \quad (B1)$$

where M_z is the z-component of the ensemble magnetic moment. Since

$$M_z = \gamma S_z \quad (B2)$$

where S_z is the z-component of the spin operator S and γ is the gyromagnetic ratio of the particles, then from [Eq. B1]

$$H = -\gamma B S_z \quad (B3)$$

The nuclear spin polarization for the ensemble of particles is defined as

$$P = \frac{\overline{\langle S_z \rangle}}{S_z} \quad (B4)$$

where $\overline{\langle S_z \rangle}$ is the ensemble average of the spin operator S_z , and can be determined by

$$\overline{\langle S_z \rangle} = \text{Tr}(\rho S_z) \quad (B5)$$

with ρ being the density matrix. If we assume that the ensemble is at thermal equilibrium then

$$\rho = \frac{e^{-H/kT}}{Z} \quad (B6)$$

Using the above equations, [Eq. B6] can be expressed as

$$\overline{\langle \mathbf{S}_z \rangle} = \frac{\text{Tr}(e^{\frac{\gamma B \mathbf{S}_z}{kT}} \mathbf{S}_z)}{Z} \quad (B7)$$

Recalling that

$$\mathbf{S}_z |S m\rangle = m\hbar |S m\rangle \quad (B8)$$

where $|S m\rangle$ is the eigenvector of the operator \mathbf{S}_z with eigenvalues $m\hbar$ (m taking on $2I+1$ values between $-I$ and I) and summing over all the states m , puts [Eq. B7] into the form

$$\overline{\langle \mathbf{S}_z \rangle} = \frac{\hbar}{Z} \sum_{m=-I}^I m e^{\frac{\gamma B m \hbar}{kT}} \quad (B9)$$

From the normalization condition of the density matrix, the partition function Z can be shown to be

$$Z = \sum_{m=-I}^I e^{\frac{\gamma B m \hbar}{kT}} \quad (B10)$$

By substituting [Eq. B10] into [Eq. B9], and assuming that the individual particles are of spin $1/2$ such as protons (that is, $m = 1/2$ or $-1/2$), we get from [Eq. B9] and [Eq. B10]

$$\overline{\langle \mathbf{S}_z \rangle} = \frac{\hbar}{2} \cdot \left[\frac{e^{\gamma B \hbar / 2kT} - e^{-\gamma B \hbar / 2kT}}{e^{\gamma B \hbar / 2kT} + e^{-\gamma B \hbar / 2kT}} \right] \quad (B11)$$

From the definition of the tanh function we can rewrite [Eq. B11]

as

$$\overline{\langle \mathbf{S}_z \rangle} = \frac{\hbar}{2} \cdot \tanh \left[\frac{\gamma B \hbar}{2kT} \right] \quad (B12)$$

Now substituting [Eq. B12] into [Eq. B4], we obtain the nuclear spin polarization for an ensemble of protons as

$$P = \tanh \left[\frac{\gamma B \hbar}{2kT} \right] . \quad (\text{B13})$$

APPENDIX C

SYSTEMATIC ERROR CALCULATIONS

To estimate the various systematic error contributions to the FST polarization measurement the following numerical values were used:

Item	LH2 runs	C runs
Incident proton beam energy (E)	469 MeV	501 MeV
Nominal scattering angle (θ)	24° (lab)	24° (lab)
Average p-p analyzing power (A_y)	0.4092	0.4204
Average FST polarization (P)	0.80	0.81
$r_o = \frac{1 + PA_y}{1 - PA_y}$	1.9734	2.0327

The average p-p analyzing power was calculated for the above θ and E values using Arndt's phase shift analysis [Ref. 3], in particular, the SP88 energy dependent solutions.

Before the various systematic error calculations are presented the following common expression is derived here to eliminate repetition.

By defining the ratio

$$r_o^2 = \frac{L^+ R^-}{L^- R^+} \quad (C1)$$

and using the following detector count rates [Eq. 72]

$$\begin{aligned} L^+ &= \sigma_o (1 + PA_y) \\ R^+ &= \sigma_o (1 - PA_y) \\ L^- &= \sigma_o (1 - PA_y) \\ R^- &= \sigma_o (1 + PA_y) \end{aligned} \quad (C2)$$

it can be shown that

$$P = \frac{1}{A_y} \left[\frac{r_o - 1}{r_o + 1} \right] \quad (C3)$$

It should be noted that the above count rates and thus r_0 are defined to be in the absence of any systematic errors. Taking the derivative of P with respect to r_0 then gives us

$$\Delta P = \frac{2}{A_y(1+r_0)^2} \Delta r \quad (C4)$$

where

$$\Delta r = r - r_0 \quad (C5)$$

The ratio r is defined similarly to the ratio r_0 [Eq. C1] but now the count rates have some systematic error contributions. Writing r in terms of r_0 via the scaler δ

$$r^2 = \delta r_0^2 \quad (C6)$$

allows [Eq. C4] to be expressed as

$$\frac{\Delta P}{P} = \frac{2r_0}{(r_0-1)(r_0+1)} \cdot (\delta^{1/2} - 1) \quad (C7)$$

We then have

$$\begin{aligned} \frac{\Delta P}{P} &= 1.3636 (\delta^{1/2} - 1) && \text{for LH2 runs} \\ &= 2.0327 (\delta^{1/2} - 1) && \text{for C runs} \end{aligned}$$

C.1 Incident Proton Beam Energy

Because the p-p analyzing power is a function of the incident proton beam energy there would be a systematic error contribution to the FST polarization measurement as a result of the beam energy uncertainty.

This contribution can be calculated from

$$\frac{\Delta P}{P} = \frac{-\Delta E}{A_y} \left[\frac{\partial A_y}{\partial E} \right]_{\theta, E} \quad (C8)$$

Using a ± 2 MeV and ± 1 MeV estimate of the incident proton beam energy uncertainty for the LH2 and C runs respectively, and

$$\left. \frac{\partial A_y}{\partial E} \right|_{\theta, E} = 4.2 \times 10^{-4} \quad (4.6 \times 10^{-4}) \quad (C9)$$

via the Arndt phase shift analysis (SP88 solution), the fractional error in the FST polarization measurement was estimated to be

$$\frac{\Delta P}{P} = 0.0021 \quad (0.0011) \quad (C10)$$

Because throughout this appendix data is presented for both calibration experiments, the terms in the brackets will correspond to the C run data.

C.2 Scattered Proton Detector Positioning

Because the p-p analyzing power was determined from the detector scattering angle distributions, there will be a systematic error contribution to the FST polarization measurement as a result of the uncertainty in determining the detector physical angular positions. Estimates of this contribution were calculated from

$$\frac{\Delta P}{P} = -\Delta\theta \left[\left. \frac{\partial A_y}{\partial \theta} \right|_{E, \theta} \right] \quad (C11)$$

Using an angular positioning uncertainty of $\Delta\theta = \pm 0.05^\circ$ (lab) and

$$\left. \frac{\Delta A_y}{\partial \theta} \right|_{E, \theta} = -0.0183 \quad (-0.0183) \quad (C12)$$

via the SP88 solution of Arndt's phase shift analysis we find

$$\frac{\Delta P}{P} = 0.0022 \quad (0.0022) \quad (C13)$$

C.3 Holding Field Deflection Angles

There could have been systematic error contributions to the FST polarization measurement arising from wrong corrections for deflection in

the holding field. As a result of this, there would have been a mismatch in the left and right event scattering angles. To estimate this contribution the following definitions were applied. The subscripts were used for left (L) and right (R) event identification.

By defining the following scattering angles

$$\theta_L = \theta' - \rho \quad \text{and} \quad \theta_R = \theta' + \rho \quad (\text{C14})$$

where

$$\theta' = \frac{\theta_L + \theta_R}{2} \quad \text{and} \quad \rho = \frac{\theta_L - \theta_R}{2} \quad (\text{C15})$$

the analyzing powers could be expressed as

$$\begin{aligned} A_L &= A_y(\theta' - \rho) \\ &= A'_y - \rho \frac{dA_y}{d\theta} + \frac{\rho^2}{2} \frac{d^2 A_y}{d\theta^2} \end{aligned} \quad (\text{C16})$$

and

$$\begin{aligned} A_R &= A_y(\theta' + \rho) \\ &= A'_y + \rho \frac{dA_y}{d\theta} + \frac{\rho^2}{2} \frac{d^2 A_y}{d\theta^2} \end{aligned} \quad (\text{C17})$$

The difference between the left and right event analyzing powers is due to the scattering angle mismatch, ρ . Substituting [Eq. C16] and [Eq. C17] into [Eq. C2] we get

$$\begin{aligned} L^+ &= \sigma_0 [1 + P(A'_y - \delta A + \delta'A)] \\ R^+ &= \sigma_0 [1 - P(A'_y + \delta A + \delta'A)] \\ L^- &= \sigma_0 [1 - P(A'_y - \delta A + \delta'A)] \\ R^- &= \sigma_0 [1 + P(A'_y + \delta A + \delta'A)] \end{aligned} \quad (\text{C18})$$

where

$$\delta A = \rho \frac{dA_y}{d\theta} \quad \text{and} \quad \delta'A = \frac{\rho^2}{2} \frac{d^2 A_y}{d\theta^2} \quad (\text{C19})$$

Using [Eq. C18] and performing the ratio in [Eq. C1] one finds the relation $r^2 = \delta r_0^2$ to be satisfied when

$$\delta = \frac{1 + 2P^2 A'_y \delta'A + 2P\delta'A - P^2 (\delta A)^2 + P^2 (\delta'A)^2}{(1 + PA'_y)^2} \cdot \frac{1 + 2P^2 A'_y \delta'A - 2P\delta'A - P^2 (\delta A)^2 + P^2 (\delta'A)^2}{(1 - PA'_y)^2} \quad (C20)$$

Since $\rho = -0.32^\circ$ (-0.37°), $\theta' = 24.20^\circ$ (23.84°), $A'_y = 0.4058$ (0.4234),

$$\left. \frac{dA'_y}{d\theta} \right|_{\theta'} = -0.0184 \quad (-0.0181)$$

and

$$\left. \frac{d^2 A'_y}{d\theta^2} \right|_{\theta'} = -0.0001 \quad (-0.0001)$$

then

$$\delta = 0.99968 \quad (0.99968) \quad (C21)$$

substituting [Eq. C21] into [Eq. C7] we obtain

$$\frac{\Delta P}{P} = 0.0002 \quad (0.0002) \quad (C22)$$

C.4 p-p Analyzing Power

Because the FST polarization is calculated from the measured scattering asymmetry and analyzing power, there would be a systematic error contribution to the polarization measurement arising from the analyzing power uncertainty. This contribution was determined from the relation

$$\frac{\Delta P}{P} = -\frac{\Delta A_y}{A_y} \quad (C23)$$

The analyzing power uncertainty ΔA_y was determined from the Arndt phase shift analysis by estimating the largest differences between energy dependent (SP88) and single energy solutions. The following differences were formed for the LH2 data

$$\Delta A_y = A_{y\text{SP88 sol'n}} - A_{y\text{C450 sol'n}} = 0.0060 \quad (\text{C24})$$

$$\Delta A_y = A_{y\text{SP88 sol'n}} - A_{y\text{S500 sol'n}} = 0.0015$$

and C data

$$\Delta A_y = A_{y\text{SP88 sol'n}} - A_{y\text{C500 sol'n}} = -0.0039 \quad (\text{C25})$$

$$\Delta A_y = A_{y\text{SP88 sol'n}} - A_{y\text{S500 sol'n}} = -0.0059$$

respectively. Using $\Delta A_y = 0.0060$ (-0.0059) in [Eq. C23] we obtained

$$\frac{\Delta P}{P} = 0.0147 \quad (0.0140) \quad (\text{C26})$$

C.5 Different FST polarizations

When the FST polarization measurement was calculated from the scattering asymmetry and analyzing power, two effective runs were used of opposite FST polarization directions. The measured polarization was then taken to be the average of the two effective run polarizations. Systematic error contributions to the FST polarization measurement would exist arising from differences between the effective run polarizations. Taking this effect into account, [Eq. C2] becomes

$$\begin{aligned} L^+ &= \sigma_0 (1 + P^+ A_y) \\ R^+ &= \sigma_0 (1 - P^+ A_y) \\ L^- &= \sigma_0 (1 - P^- A_y) \\ R^- &= \sigma_0 (1 + P^- A_y) \end{aligned} \quad (\text{C27})$$

Defining

$$P = \frac{|P^+| + |P^-|}{2} \text{ and } \delta P = \frac{|P^+| - |P^-|}{2}, \quad (\text{C28})$$

and substituting [Eq. C27] into the ratio in [Eq. C1], we find δ in the relation $r^2 = \delta r_0^2$ to be

$$\delta = 1 - \frac{A_y^2 (\delta P)^2}{(1 + PA_y)^2} \frac{1 - A_y^2 (\delta P)^2}{(1 - PA_y)^2} \quad (\text{C29})$$

using $\delta P = -0.0059$ (0.0014) from the NMR polarization values we find

$$\delta = 1.000010 \text{ (1.0000006)} \quad (\text{C30})$$

Substituting [Eq. C30] into [Eq. C7]

$$\frac{\Delta P}{P} = 7 \times 10^{-6} \text{ (} 4 \times 10^{-7} \text{)} \quad (\text{C31})$$

It is illustrated above that this contribution is negligible.

C.6 Background Fraction Estimation

Another systematic error contribution to the FST polarization measurement could have arisen from the method used to estimate the background fraction [see section IV.5.a.1]. Rearranging [Eq. C2] to take into account the various background contributions

$$\begin{aligned} L^+ &= \sigma_L^+ + \Delta f_L^+ \sigma_B \\ R^+ &= \sigma_R^+ + \Delta f_R^+ \sigma_B \\ L^- &= \sigma_L^- + \Delta f_L^- \sigma_B \\ R^- &= \sigma_R^- + \Delta f_R^- \sigma_B \end{aligned} \quad (\text{C32})$$

it can be shown then, that

$$\delta = 1 + \frac{\Delta f_L^+ \sigma_B}{\sigma_L^+} + \frac{\Delta f_R^- \sigma_B}{\sigma_R^-} - \frac{\Delta f_R^+ \sigma_B}{\sigma_R^+} - \frac{\Delta f_L^- \sigma_B}{\sigma_L^-} \quad (C33)$$

for the relation $r^2 = \delta r_0^2$ to be true. The various terms in [Eq. C33], which will be referred to as Δf_L^+ , Δf_R^- , Δf_R^+ and Δf_L^- , correspond to the calculated background fractions. Calculating these terms from the general equation

$$\Delta f = \Delta \phi \cdot \left. \frac{df}{d\phi} \right|_{\phi = 6^\circ} \quad (C34)$$

where the derivative is the rate of change of the calculated background fraction with non-coplanarity angle ϕ , evaluated for $\phi = 6^\circ$, and $\Delta \phi$ the root-mean-square of the multiple scattering angle. It can be shown, from the following $\chi_{\text{sum}}^2 \leq 15$ data

$$\left. \frac{df_L^+}{d\phi} \right|_{\phi = 6^\circ} = -0.0208 \quad (-0.0208) \quad \left. \frac{df_R^+}{d\phi} \right|_{\phi = 6^\circ} = -0.0133 \quad (-0.0133) \quad (C35)$$

$$\left. \frac{df_L^-}{d\phi} \right|_{\phi = 6^\circ} = -0.0148 \quad (-0.0148) \quad \left. \frac{df_R^-}{d\phi} \right|_{\phi = 6^\circ} = -0.0199 \quad (-0.0199)$$

and

$$\Delta \phi = 0.62^\circ \quad (0.58^\circ) \quad (C36)$$

that

$$\frac{\Delta P}{P} = 0.0049 \quad (0.0047) \quad (C37)$$

C.7 Superconducting Solenoid Spin Precession

Systematic error contribution to the FST polarization measurement could have arisen by not having the incident beam polarization in the horizontal, x - z plane. There were two independent effects.

C.7.a Incorrect Solenoid Current Setting

After the experiment, the spin precession angle, θ_p , of the solenoid was measured (see section III.3.c) and it was found to be $89.8^\circ \pm 1.8^\circ$ (2%). If we consider the worst case, $\theta_p = 88^\circ$, then the incident beam polarization along the y - axis, P_B^y , would be

$$P_B^y = P^y \cdot \sin(90^\circ - \theta_p) \quad (C38)$$

where P^y is the secondary proton beam polarization along the y - axis, as a result of 9° (lab) scattering of the unpolarized primary proton beam, within the secondary beam production target. Rearranging [Eq. C2].

for the presence of P_B^y we get

$$\begin{aligned} L^+ &= \sigma_0 [(1 + A_y P_T^y) + A_y P_B^y + P_T^y P_B^y A_{yy}] \\ R^+ &= \sigma_0 [(1 - A_y P_T^y) - A_y P_B^y + P_T^y P_B^y A_{yy}] \\ L^- &= \sigma_0 [(1 - A_y P_T^y) + A_y P_B^y - P_T^y P_B^y A_{yy}] \\ R^- &= \sigma_0 [(1 + A_y P_T^y) - A_y P_B^y - P_T^y P_B^y A_{yy}] \end{aligned} \quad (C39)$$

where P_T^y is the FST polarization assumed to be parallel to the y - axis and A_{yy} is one of the p-p spin correlation parameters at $\theta = 24^\circ$ (lab) and incident proton beam energy E. Substituting [Eq. C39] into [Eq. C1] we find the relation $r^2 = \delta r_0^2$ to be satisfied when

$$\delta = \frac{1 - \frac{(A_y P_B^y + P_T^y P_B^y A_{yy})^2}{(1 + A_y P_T^y)^2}}{1 - \frac{(A_y P_B^y - P_T^y P_B^y A_{yy})^2}{(1 - A_y P_T^y)^2}} \quad (C40)$$

Using the values

$$P^y = 0.4099 \text{ (0.2389)} \quad (C41)$$

$$A_{yy} = 0.6368 \text{ (0.6086)}$$

which were derived from the SP88 solution of Arndt's phase shift analysis, it can be shown

$$\frac{\Delta P}{P} = 7 \times 10^{-5} \text{ (} 2 \times 10^{-5} \text{)} \quad (C42)$$

The systematic error contribution to the FST polarization as a result of the above effect has been illustrated to be negligible.

C.7.b Solenoid Misalignment

The $\int B \cdot dl$ of the superconducting solenoid due to a misalignment angle, θ_s , will be

$$\sin\theta_s (\int B \cdot dl)_{\text{solenoid}} \quad (C43)$$

thus the change in $\int B \cdot dl$ will be

$$[1 - \sin\theta_s] \cdot (\int B \cdot dl)_{\text{solenoid}} \quad (C44)$$

But since the spin precession angle of a solenoid is directly proportional to the $(\int B \cdot dl)_{\text{solenoid}}$, then the spin precession angle, θ_p , will change to

$$\theta_p(1 - \sin\theta_s) \quad (C45)$$

due to the presence of θ_s . Thus if $\theta_p = 90^\circ$ and $\theta_s = 0.1^\circ$ then the new precession angle, θ'_p , would be 89.8° . Substituting this value for θ_p in [Eq. C38] and once again solving [Eq. C40], it can be shown that

$\frac{\Delta P}{P}$ will be just as negligible.

C.8 Extraneous Beam and FST Polarization Components

Because the scattering asymmetry was calculated by using [Eq. C2], a systematic error contribution to the FST polarization measurement could have arisen from possible extraneous beam and FST polarization components. Rearranging [Eq. C2] for the various polarization components we have

$$\begin{aligned}
 L^+ &= \sigma_0[(1 + P_T^y A_y) + a] \\
 R^+ &= \sigma_0[(1 - P_T^y A_y) + b] \\
 L^- &= \sigma_0[(1 - P_T^y A_y) + c] \\
 R^- &= \sigma_0[(1 + P_T^y A_y) + d]
 \end{aligned} \tag{C46}$$

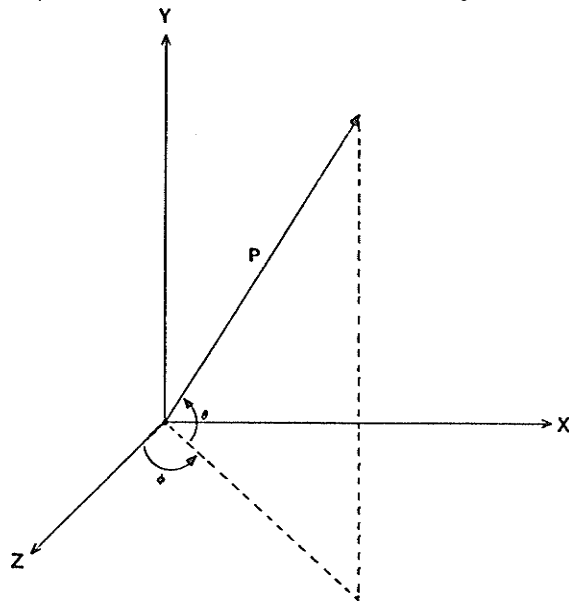
where

$$\begin{aligned}
 a &= A_y P_B^y + P_T^y P_B^y A_{yy} + P_T^x P_B^x A_{xx} + P_T^z P_B^z A_{zz} + (P_T^x P_B^z + P_T^z P_B^x) A_{zx} \\
 b &= -A_y P_B^y + P_T^y P_B^y A_{yy} + P_T^x P_B^x A_{xx} + P_T^z P_B^z A_{zz} - (P_T^x P_B^z + P_T^z P_B^x) A_{zx} \\
 c &= A_y P_B^y - P_T^y P_B^y A_{yy} - P_T^x P_B^x A_{xx} - P_T^z P_B^z A_{zz} - (P_T^x P_B^z + P_T^z P_B^x) A_{zx} \\
 d &= -A_y P_B^y - P_T^y P_B^y A_{yy} - P_T^x P_B^x A_{xx} - P_T^z P_B^z A_{zz} + (P_T^x P_B^z + P_T^z P_B^x) A_{zx}
 \end{aligned} \tag{C47}$$

In the above equation P_B and P_T are the beam and FST polarizations, with their various x, y, and z - components identified as superscripts; A_{xx} , A_{yy} , A_{zz} , and A_{zx} are the proton spin correlation parameters obtained from Arndt's phase shift analysis (SP88 solution) and were determined for $\theta = 24^\circ$ (lab) and incident proton energy E, as indicated at start of the appendix. Substituting [Eq. C46] and [Eq. C47] into [Eq. C1], one finds the relation $r^2 = \delta r_0^2$ to hold when

$$\delta = \frac{1 + (a + d)(1 + A_y P_T^y) + ad}{(1 + A_y P_T^y)^2} \cdot \frac{1 + (c + b)(1 + A_y P_T^y) + cb}{(1 - A_y P_T^y)^2} \quad (C48)$$

If we define the beam and FST polarization components as



$$p^x = P \cos \theta \sin \phi$$

$$p^y = P \sin \theta$$

$$p^z = P \cos \theta \cos \phi$$

and using the following data

$$A_{xx} = -0.5178 \quad (-0.5001)$$

$$A_{yy} = 0.6369 \quad (0.6086)$$

$$A_{zz} = 0.5025 \quad (0.4574)$$

$$A_{zx} = 0.1627 \quad (0.1399)$$

$$P_T = 0.80 \quad (0.81)$$

for FST polarization

$$P_B = 0.4099 \quad (0.2389)$$

for beam polarization

$$\theta = 2^\circ \quad \phi = 88^\circ$$

for beam polarization

$$\theta = 88^\circ \quad \phi = 2^\circ$$

for FST polarization

then after some substitution we find

$$\frac{\Delta P}{P} = 0.0056 \quad (0.0028) \quad (C49)$$

APPENDIX D

EXPERIMENTAL DATA

The following data that will be presented below are for the ratio method calculated scattering asymmetries using effective run count rates corrected for background, incident proton beam current and detector efficiencies. The various effective run data that was used is tabulated in [Table D1]. The $\bar{P}_{\text{NMR}}(j)$ values as tabulated, were calculated using [Eq. 100] which is the straight average of the spin up (+) and spin down (-) effective run \bar{P}_{NMR} values, listed in [Table 27] and [Table 28].

The index used throughout this appendix and their assignments are defined below:

(1) i index:

index number	FST bin
1	bottom
2	middle
3	top

(2) j index:

index number	"Bonnie" DAC setting	
	LH2 runs	C runs
1	0.02	0.00
2	0.07	0.05
3	0.15	0.10
4		0.10*

[*polarity interchanged]

(3) k index:

index number	$\chi_{\text{sum}}^2 \leq \text{cut}$
1	10
2	15
3	20

All of the uncertainties that will be stated below are due to statistical fluctuations only.

[Table D1]

Effective Run Data

j index	"Bonnie" DAC setting	Effective run identification		- P _{NMR} (j)
		Spin up (+)	Spin down (-)	
For LH2 run:				
1	0.02	1	4	0.7991
2	0.07	2	5	0.7867
3	0.15	3	6	0.8076
For C runs:				
1	0.00	1	5	0.8149
2	0.05	2	6	0.8193
3	0.10	3	7	0.8156
4	0.10*	4	8	0.8135

* The polarity of "Bonnie" was interchanged.

[Table D2]

LH2 Run Data

index i j k	$A_y(i, j, k)$	$\epsilon(i, j, k)$	$P(i, j, k)$	$\mu(i, j, k)$
1 1 1	.41257 ± .00062	.2969 ± .0085	.7197 ± .0206	.9007 ± .0258
2	.41265 ± .00061	.2959 ± .0082	.7171 ± .0200	.8974 ± .0250
3	.41261 ± .00060	.2958 ± .0081	.7170 ± .0198	.8973 ± .0247
1 2 1	.41221 ± .00043	.3093 ± .0107	.7503 ± .0260	.9538 ± .0330
2	.41243 ± .00042	.3056 ± .0104	.7410 ± .0253	.9419 ± .0322
3	.41260 ± .00042	.3037 ± .0103	.7360 ± .0251	.9355 ± .0319
1 3 1	.41083 ± .00132	.3071 ± .0155	.7475 ± .0379	.9257 ± .0469
2	.41127 ± .00128	.3045 ± .0151	.7403 ± .0368	.9167 ± .0455
3	.41135 ± .00125	.3069 ± .0150	.7461 ± .0365	.9239 ± .0452
2 1 1	.41129 ± .00048	.3083 ± .0073	.7495 ± .0179	.9380 ± .0224
2	.41142 ± .00047	.3040 ± .0071	.7384 ± .0174	.9247 ± .0218
3	.41141 ± .00046	.3047 ± .0071	.7407 ± .0172	.9269 ± .0215
2 2 1	.41236 ± .00027	.3288 ± .0069	.7974 ± .0166	1.0135 ± .0211
2	.41246 ± .00027	.3274 ± .0067	.7937 ± .0162	1.0089 ± .0206
3	.41246 ± .00026	.3251 ± .0066	.7881 ± .0161	1.0018 ± .0204
2 3 1	.41180 ± .00056	.3115 ± .0062	.7564 ± .0151	.9366 ± .0186
2	.41188 ± .00055	.3141 ± .0060	.7625 ± .0146	.9442 ± .0181
3	.41188 ± .00054	.3119 ± .0060	.7572 ± .0145	.9377 ± .0180
3 1 1	.41152 ± .00091	.3438 ± .0179	.8354 ± .0435	1.0455 ± .0544
2	.41178 ± .00088	.3456 ± .0173	.8393 ± .0419	1.0504 ± .0525
3	.41194 ± .00086	.3451 ± .0171	.8378 ± .0416	1.0485 ± .0520
3 2 1	.41227 ± .00043	.3352 ± .0112	.8130 ± .0273	1.0334 ± .0346
2	.41245 ± .00041	.3328 ± .0109	.8068 ± .0265	1.0256 ± .0337
3	.41244 ± .00041	.3313 ± .0108	.8033 ± .0263	1.0211 ± .0334
3 3 1	.41080 ± .00064	.3283 ± .0081	.7991 ± .0198	.9896 ± .0245
2	.41103 ± .00062	.3371 ± .0078	.8202 ± .0190	1.0156 ± .0236
3	.41115 ± .00062	.3284 ± .0078	.7988 ± .0189	.9891 ± .0234

[Table D3]

C Run Data

index i j k	$A_y(i, j, k)$	$\epsilon(i, j, k)$	$P(i, j, k)$	$\mu(i, j, k)$
1 1 1	.42918 ± .00047	.3324 ± .0066	.7745 ± .0155	.9505 ± .0190
2	.42948 ± .00045	.3351 ± .0064	.7803 ± .0150	.9576 ± .0184
3	.42966 ± .00045	.3337 ± .0064	.7767 ± .0149	.9532 ± .0183
1 2 1	.42913 ± .00042	.3243 ± .0134	.7556 ± .0312	.9218 ± .0380
2	.42938 ± .00041	.3193 ± .0131	.7437 ± .0304	.9073 ± .0371
3	.42955 ± .00040	.3171 ± .0130	.7385 ± .0303	.9009 ± .0370
1 3 1	.42749 ± .00065	.3297 ± .0116	.7713 ± .0272	.9456 ± .0333
2	.42785 ± .00063	.3337 ± .0113	.7801 ± .0265	.9564 ± .0325
3	.42801 ± .00063	.3267 ± .0113	.7633 ± .0265	.9359 ± .0324
1 4 1	.42869 ± .00026	.3250 ± .0043	.7581 ± .0100	.9320 ± .0123
2	.42898 ± .00025	.3260 ± .0042	.7600 ± .0097	.9343 ± .0119
3	.42919 ± .00025	.3247 ± .0041	.7565 ± .0096	.9300 ± .0118
2 1 1	.42865 ± .00030	.3271 ± .0043	.7631 ± .0100	.9364 ± .0122
2	.42902 ± .00030	.3292 ± .0041	.7674 ± .0097	.9418 ± .0119
3	.42911 ± .00030	.3294 ± .0041	.7677 ± .0096	.9421 ± .0118
2 2 1	.42912 ± .00027	.3261 ± .0072	.7600 ± .0168	.9271 ± .0205
2	.42941 ± .00026	.3300 ± .0070	.7684 ± .0163	.9374 ± .0199
3	.42951 ± .00026	.3314 ± .0070	.7716 ± .0162	.9412 ± .0198
2 3 1	.42937 ± .00029	.3219 ± .0052	.7497 ± .0121	.9191 ± .0148
2	.42963 ± .00028	.3245 ± .0051	.7553 ± .0118	.9260 ± .0145
3	.42977 ± .00028	.3250 ± .0050	.7562 ± .0118	.9272 ± .0144
2 4 1	.42893 ± .00027	.3307 ± .0043	.7711 ± .0101	.9479 ± .0124
2	.42931 ± .00026	.3334 ± .0042	.7766 ± .0098	.9546 ± .0121
3	.42947 ± .00026	.3329 ± .0042	.7751 ± .0097	.9528 ± .0120
3 1 1	.42878 ± .00050	.3395 ± .0066	.7918 ± .0154	.9717 ± .0189
2	.42894 ± .00049	.3412 ± .0064	.7955 ± .0149	.9762 ± .0183
3	.42910 ± .00048	.3366 ± .0063	.7845 ± .0148	.9628 ± .0182
3 2 1	.42932 ± .00040	.3509 ± .0093	.8173 ± .0217	.9970 ± .0265
2	.42949 ± .00039	.3544 ± .0091	.8250 ± .0211	1.0065 ± .0258
3	.42963 ± .00039	.3499 ± .0090	.8144 ± .0210	.9935 ± .0257

Continued

3 3 1	.42921 ± .00032	.3344 ± .0056	.7790 ± .0131	.9551 ± .0161
2	.42967 ± .00031	.3369 ± .0055	.7841 ± .0128	.9613 ± .0156
3	.42992 ± .00031	.3355 ± .0054	.7804 ± .0127	.9567 ± .0155
3 4 1	.42863 ± .00067	.3461 ± .0110	.8075 ± .0257	.9927 ± .0317
2	.42889 ± .00065	.3452 ± .0107	.8050 ± .0250	.9896 ± .0307
3	.42915 ± .00065	.3437 ± .0107	.8008 ± .0249	.9845 ± .0306
